ALMA MATER STUDIORUM – UNIVERSITÀ DI BOLOGNA

SCUOLA DI INGEGNERIA E ARCHITETTURA

DIPARTIMENTO DI INGEGNERIA INDUSTRIALE

CORSO DI LAUREA MAGISTRALE IN INGEGNERIA ENERGETICA

TESI DI LAUREA

in

FISICA TECNICA INDUSTRIALE

MICROCHANNEL HEAT EXCHANGERS: AN ATTRACTIVE OPTION FOR THE REGENERATOR OF A MOBILE ORC WASTE HEAT RECOVERY SYSTEM

CANDIDATO
Alessandro Mantovanelli

RELATORE
Chiar.mo Prof. Gian Luca Morini

CORRELATORE
Chiar.mo Prof. Piero Colonna

Anno Accademico 2013/14

Sessione III

Contents

Acknowledgments

My gratitude goes to Prof. Gian Luca Morini and Prof. Piero Colonna for making this project possible: working under their guidance and expertise was an extraordinary learning opportunity.

Special thanks to all the guys of the Power & Propulsion Department of the TU Delft, for their help and for the time spent together. I'm grateful to Sebastian in particular, for his supervision and for the time he spent on my work.

My parents deserve tanks of thanks, for their patience and support in every imaginable way.

Finally, thanks to all the wonderful people I met during this beautiful era that is about to end, and to those who have always been there.

Abstract

The technical advancements of the last decades have made organic Rankine cycles (ORC) an attractive option for automotive applications: several examples of waste heat recovery systems suitable for internal combustion engines of heavy duty vehicles are available in literature.

Mobile power systems must be compact and light: generally heat exchangers constitute the largest part of the whole installation, hence the priority in reducing their dimensions and weight. Microchannels heat exchangers (MCHE) are distinguished by a very high ratio of surface area to volume, low thermal resistances, small volumes, low total mass and low inventory of working fluids, and are therefore the ideal candidate.

Typically, applications such as waste heat recovery usually involve heat loads and mass flow rates significantly higher than any device found in the open literature: automotive MCHE exist as proprietary or in-house packages only and have not penetrated the market yet. Further research is therefore needed to assess performance and limits of microchannel technology coupled with mobile ORC systems. The task is complicated by the sensibility of microflows to phenomena usually negligible in channels of conventional size.

The present work, carried out at the Propulsion&Power Department of Delft University of Technology, aims to design a microchannel regenerator optimized for a specific ORC waste heat recovery system, which is the target of a recent feasibility study funded by TU Delft in cooperation with two European automotive manufacturers. The system requires the regenerator to transfer around 35 kW_{th} from the gas-side to the-liquid-side. In the open literature, no microchannel devices are proposed above 5 kW_{th} nor is a suitable optimization procedure available, making the project original and innovative.

The optimization process developed in this document is implemented in the MATLAB environment. Appropriate values for each design parameter describing the geometry of the MCHE core are selected in order to obtain a light and compact device. Each

parameter is allowed to vary between a maximum and a minimum value, determined from information on the manufacturing method, on the distribution elements and on the other components of the ORC system in which the MCHE is to be integrated. Some of the considerations made to establish the constraints have general validity and may come handy for diverse microchannel applications.

An important feature of the procedure is the accurate estimation of conjugate heat transfer, which is shown to have strong impact on the thermal behavior of the microchannel device. Two different alloys with substantially different thermal conductivity are considered for the solid walls, leading to remarkably different optimal design parameters.

For each material, specifically a copper-based and an aluminium based alloy suitable for the required manufacturing method, the optimization process calculates the best counterflow and crossflow configuration which satisfy the thermohydraulic requirements fed to the MATLAB script. Four optimized heat exchangers, from the lightness and compactness point of view, are provided in only a few minutes of computational time.

In order to validate the simplification introduced in the selection process, the optimal designs are rated in detail and the magnitude of the scaling effects is estimated following the guidelines available in literature. Computational fluid-dynamics (CFD) analysis of the crossflow arrangement are impracticable, but the symmetry planes of the crossflow MCHE may be exploited to single out a sufficiently contained computational domain. CFD simulations in ANSYS Fluent are in good agreement with the implemented model, with relative errors of in the order of only 0.5 % for what concern both the heat exchanger effectiveness and the total pressure drop in the core.

The optimized microchannel devices offer striking improvement in compactness and lightness compared to the exchanger originally meant for the specified ORC system. The distribution elements are found to have major impact on dimension and weight. A preliminary design is given however improvement might be needed. Experimental information on the manufacturing process and the materials are also required.

Nomenclature

Appropriate SI base and derived units eventually with metric prefixes are used throughout the present document; IEEE Standards Style is adopted for numbering and citing references, equations, figures and tables.

Acronyms

ASME	American Society of Mechanical Engineers
CFD	computational fluid-dynamics
DN	Nominal Diameter, designator used in the SI system to describe pipe size
EU	European Union
EU-28	the 28 member states comprised by EU since July 2013
GHG	greenhouse gas: CO_2 ; CH_4 ; N_2O ; HFCs ; PFCs ; SF_6
HDV	heavy-duty vehicle: motor vehicle with gross weight greater than 7500 kg
IEEE	Institute of Electrical and Electronics Engineers
LIGA	Lithographie, Galvanoformung und Abformung
MCHE	microchannel heat exchanger
NADCA	North American Die Casting Association
NIST	National Institute of Standards and Technology
ORC	organic Rankine cycle
PFHE	plate-fin heat exchanger
PHE	plate heat exchanger
SI	international system of units

Roman Symbols

A	heat transfer surface area, better specified by the subscript [m^2]
a	aspect ratio of the channels on the hot-side [#]
b	aspect ratio of the channels on the cold-side [#]
Br	Brinkmann number [#]
C	heat capacity rate [W/K]
c	long dimension of the cold-side channels [m]
c_P	specific heat of fluid at constant pressure [J/(kg K)]
d	short dimension of the cold-side channels [m]
D	diameter of the supply or return pipe, better specified by the subscript [m]
D_C	smallest characteristic length for heat exchanger passages [m]
D_H	hydraulic diameter of flow passages [m]
f	Fanning friction factor [#]
G	fluid mass flux, mass flow rate per unit surface area [kg/(m^2 s)]
h	heat transfer coefficient [W/(m^2 K)]
H	header parameter [#]
k	thermal conductivity [W/(m K)]
K_∞	Hagenbach's factor [#]
Kn	Knudsen number [#]
L	fluid flow length on one side of the heat exchanger [m]
l	long dimension of the hot-side channels [m]
L_{HD}	hydrodynamic entrance length [m]
L_{TH}	thermal entrance length [m]
L_w	width of the counterflow modules [m]
m	fin parameter [#]
$\dot{m}$	fluid mass flow rate [kg/s]
M	molar mass of a gas [kg/mol]
N_c	number of channels on the cold-side [#]
N_h	number of channels on the hot-side [#]
N_m	number of modules [#]

N_p	number of plates [#]
NTU	number of transfer units [#]
Nu	Nusselt number [#]
p	fluid static pressure [Pa]
P	perimeter [m]
Pe	Peclét number [m]
Po	Poiseuille number [#]
Pr	Prandtl number [#]
q	heat flux, heat transfer rate per unit surface area [W/m^2]
$\dot{Q}$	heat transfer rate: thermal power exchanged or heat duty [W]
R	universal gas constant [$J/(mol\ K)$]
r	heat capacity rate ratio [#]
R	thermal resistance [K/W]
Re	Reynolds number [#]
S	free flow area, better specified by the subscript [m^2]
s	short dimension of the hot-side channels [m]
S_w	area of the dividing wall [m^2]
T	fluid temperature, better specified by the subscript: static [°C] or absolute [K]
t_w	wall shear stress [Pa]
u	fluid mean axial velocity inside the microchannel [m/s]
UA	overall thermal conductance [W/K]
V	volume, better specified by the subscript [m^3]
v	fluid mean axial velocity inside the headers [m/s]
x	coordinate along the flow direction of the hot fluid [m]
X	non-dimensional coordinate along the flow direction of the hot fluid [m]
x_h	coordinate in the flow direction of the header [m]
y	coordinate along the flow direction of the cold fluid [m]
Y	non-dimensional coordinate along the flow direction of the cold fluid [m]
y_c	coordinate perpendicular to the core for the cold-side outlet header [m]
y_h	coordinate perpendicular to the core for the cold-side outlet header [m]
z	coordinate along the no-flow or stack height direction [m]
z_c	coordinate perpendicular to the core for the cold-side inlet header [m]
z_h	coordinate perpendicular to the core for the hot-side inlet header [m]

Greek Symbols

α	ratio of the total transfer area to the total exchanger mass [m^2/kg]
β	heat transfer surface area density [m^2/m^3]
δ	thickness of the dividing wall [m]
ϵ	average surface roughness height [m]
ε	heat exchanger effectiveness [#]
η_f	fin efficiency [#]
η_o	extended surface efficiency [#]
θ	non-dimensional hot-side temperature [#]
Θ	non-dimensional wall temperature [#]
ϑ	non-dimensional cold-side temperature [#]
κ_{HD}	dimensionless hydrodynamic entrance length [#]
κ_{TH}	dimensionless thermal entrance length [#]
λ	mean free path [m]
Λ	longitudinal heat conduction parameter [#]
μ	fluid dynamic viscosity [Pa s]
ρ	mass density [kg/m^3]
ϱ	ratio of the cold fluid heat capacity rate to the hot fluid heat capacity rate [#]
σ	ratio of the free flow area to the frontal area [#]
τ	frame thickness [m]
φ	fin thickness [m]
ψ	generic physical property in the appropriate units of measurement
ω	weight [kg]

Subscripts

abrupt	abrupt entrance and exit in the headers
acc	acceleration
app	apparent
av	average
b	bulk
c	cold-fluid side (liquid)
f	fin
fr	friction
h	hot-fluid side (gas)
head	header
in	inlet
max	maximum
min	minimum
out	outlet
p	primary
pipe	supply and return piping
r	reference
w	wall separating the fluids

1 Introduction

The European Union (EU) climate and energy policy targets towards 2020 include international commitments pursuant to the Kyoto Protocol and a more ambitious EU unilateral commitment, the so-called 20/20/20 triple objective [1]. Endorsed by the European Council in 2007 and implemented through the 2009 Climate and Energy Package and the 2012 Energy Efficiency Directive, this program aims to achieve the following improvements with respect to the base year 1990:

- 20 % reduction of greenhouse gas emissions
- 20 % share of renewable energy in energy consumption
- 20 % increase in energy efficiency

The EU-28 Countries are essentially on track towards their respective targets: for what concerns greenhouse gas (GHG) emissions, in 2012 approximately 4544 Tg CO_2 equivalents of GHE were released to the atmosphere, corresponding to 19.2 % less than base year levels. An estimated decrease of 1.3 % occurred between 2011 and 2012 [2].

In the same year, the share of GHG emissions ascribable to road transport was 19.7 %, of which 98.8 % were CO_2 [2]. If no additional measures are adopted, the future scenarios outlined in Figure 1 forecast a rise in emissions from this sector, in contrast to a generally decreasing trend. It is therefore evident that more efforts should be made to

limit GHG emissions especially from vehicles. The most significant existing measures include the implementation of the 2009/443/EC and 2011/510/EU Regulations and following Amendments, which set limits for CO_2 emissions from new cars and light commercial vehicles. On the other hand, heavier vehicles such as trucks and buses are currently unrestricted.

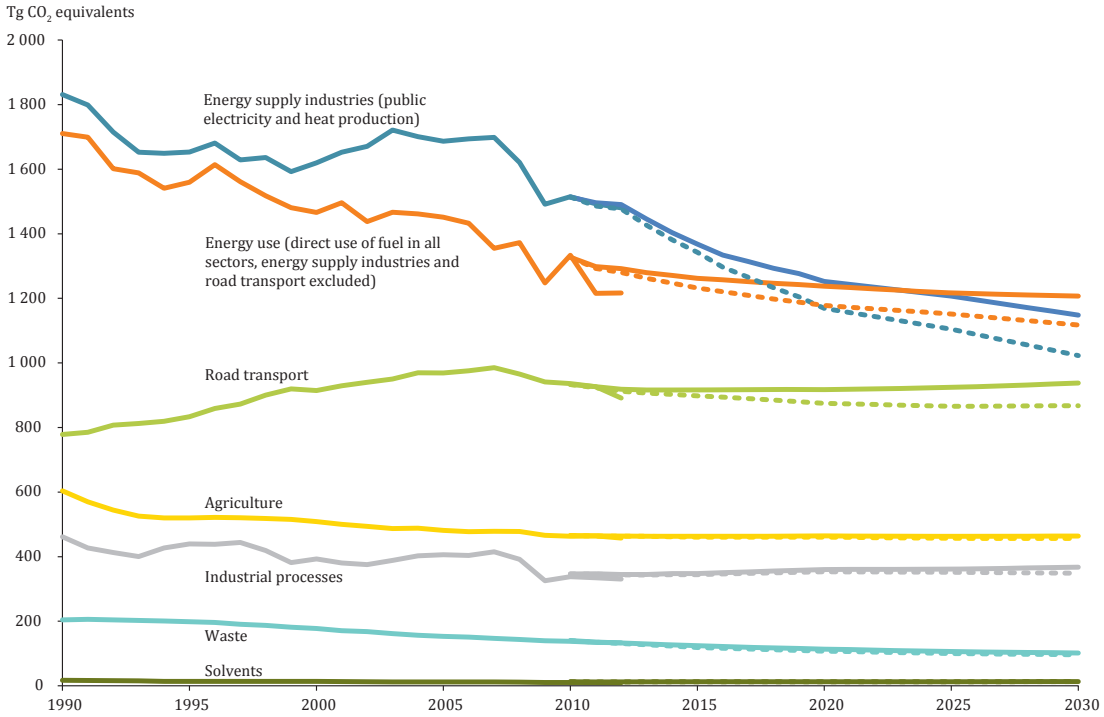

Note: Solid lines represent historic GHG emissions up to 2012 and with existing measures projections from 2010 onwards. Dashed lines represent with additional measures projections.
The projected trends were calibrated to the 2010 year of the latest inventory data, which is the base year for the projections for most Member States.

Source: EEA, 2013a; EEA, 2013d; EEA, 2013f.

Figure 1: sectoral trends and projections of EU GHG emissions in EU-28 **[1]**

In 2011, heavy-duty vehicles (HDV) accounted for approximately 26 % of EU-28 road transport related CO_2 [3]. Despite a CO_2 emission normative specific to HDV has not entered yet into legal force, a strategy for reducing CO_2 from HDV was defined with the 2014/285/COM Communication. Climate Action Commissioner Connie Hedegaard stated short after the approval:

« *Today we are taking the next steps to curb emissions from road transport. We first regulated cars and vans, and we can now see the results: emissions have been reduced,*

air pollution in cities is in decline, and more innovative, fuel-efficient vehicles are now available to consumers. That is why we turn now to trucks and buses. This strategy outlines new measures which over time will cut CO_2 emissions of these vehicles, save operators money and make the EU less dependent on imported oil. » [*]

This policy was also welcomed by the European commercial vehicle industry. Erik Jonnaert, Secretary General of the European Automobile Manufacturers' Association, commented on the certification system introduced in the approved Communication:

« *Fuel efficiency is a top priority for the transport companies who buy and use trucks and buses, because fuel accounts for over one-third of their total operating costs. Fuel efficiency is therefore the number one competitive factor in developing and selling heavy-duty vehicles. This system will empower customers to compare and choose the most fuel-efficient vehicle combination adapted to their needs.* » [**]

In order to reduce fuel consumption and therefore emissions, the documentation [3] attached to 2014/285/COM recommends several waste heat recovery technologies suitable for HDV engines, among which bottoming systems based on organic Rankine cycle (ORC) are possibly the most promising choice [4]. The literature reviewed in [5] clearly reports that fuel economy improvements around 10 % are a practicable outcome, granting a payback period of only 2-5 years.

In HDV reciprocating engines, exhaust gas energy has the highest and most technically feasible recovery potential [6] and represents a significant amount of the fuel energy, as shown in Figure 2. The exhaust gas is available at temperatures ranging from 200 to 400 °C, and in the exhaust gas recirculation (EGR) system at even higher temperatures, from 280 to 580 °C. [6].

ORC systems have already been widely exploited for heat recovery from stationary

[*] "Climate action: Commission sets out strategy to curb CO_2 emissions from trucks, buses and coaches", European Commission press release, Brussels, 21/5/2014

[**] "European auto industry welcomes transparency for customers on CO_2 from heavy-duty vehicles", European Automobile Manufacturers' Association press release, Brussels, 21/5/2014

energy sources at comparable temperature [7]. However, the implementation on board of vehicles is challenging, and it is still in research phase. Although the first ORC studies date from the oil crisis of the 1970s, no commercial application exists [6]. Recent published papers sponsored by Honda, Toyota, BMW, Wartsila and Volvo show a renewed interest in this technology, impelled by the surge in fuel prices and upcoming regulations [5]. Naturally, the ideal condition for such systems is stable engine load and speed over a large portion of operation hours [8]. This is why research concentrates on HDV designed for freight transport on long hauling routes. However, in principle this concept may be applied also to passengers car [9], which would require even more compact equipment due to reduced size.

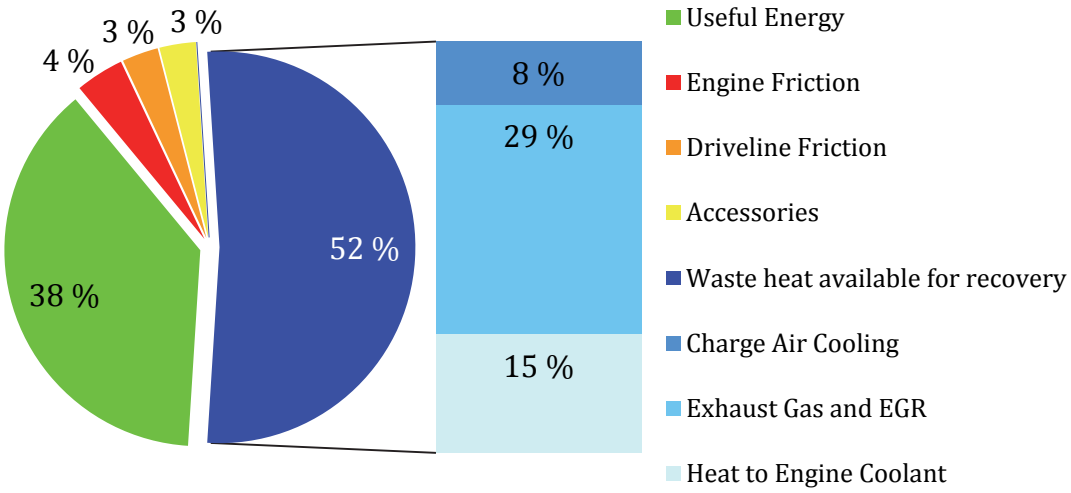

Figure 2: typical fuel energy dissipation in a HDV **[10]**

Compactness and lightweight are of course crucial for mobile applications [6]. The technical advancements of the last decades in the critical components (evaporator, condenser, regenerator, expander, etc.) of ORC systems are now making them a concrete option to increase the thermal efficiency of automotive internal combustion engines [9]. However, the heat exchangers (PHE) usually employed in such systems are still considered more voluminous than desirable [6]. Generally, heat exchangers constitute the largest part of the space occupied by the whole bottoming installation, hence the priority in reducing their dimensions and weight [8]. Microchannels heat exchangers (MCHE) are ideal candidates due to several features: high ratio of surface area to

volume, low thermal resistances, small volumes, low total mass and low inventory of working fluids [11]. While a comprehensive literature on MCHE for electronic cooling is available, there is limited research that focuses on larger applications such as waste heat recovery. Automotive MCHE exist as proprietary or in-house packages only and have not penetrated the market yet [12]. In order to provide a better alternative to the state-of-the-art technology, it is therefore important to assess the performance of such heat exchangers in mobile ORC systems.

1.1 Organic Rankine Cycle

The organic Rankine cycle (ORC) is a Rankine cycle that does not use steam as its working fluid, but an *organic fluid*, i.e. a compost, not necessarily present in living organisms, containing a significant quantity of carbon [13].

1.1.1 Field of Application

Figure 3 approximately represents the field of employment, in terms of temperature and power, for heat engines using steam or organic fluids. Steam has practically no rivals in applications requiring largepower levels (higher than 500-1000 kW_e) and at medium-high temperatures (above 200-250 °C). For lower power levels, the steam turbine is usually too expensive due to several factors that increase the cost: high maximum pressure (150-300 bar) and temperature (500-700 °C) of the cycle, complexity of the plant layout (numerous regenerators) and of the turbine expander (several stages) [13].

Only few organic fluids can be operated at temperatures above 300°C, due to thermal stability issues. Temperatures below 70-100 °C make the costs of the ORC engine prohibitive, so that it is often recommended not to use them unless the power levels are particularly high, as in the case of ocean thermal energy conversion (OTEC) systems. Very low power levels (below a few tens of kW_e, typical in micro-cogeneration systems) mean high costs for the organic fluid engine and, consequently, it becomes at present often uneconomic [13].

Nevertheless, interest in the ORC technology is growing rapidly and the range of potential applications, at low and medium-high temperatures, is vast. Development potential is high in the sectors of primary generation and cogeneration (including the domestic field, within the range of a few kW_e); in biomass fired systems; when there are difficult fuels involved (syngas, flare gas, etc.); in the concentrated solar power sector; in the various forms of heat recovery (from industrial processes, from gas turbines, from reciprocating internal combustion engines, in plants for re-gasification of natural gas, etc.); in the exploitation of geothermal sources and in OTEC systems [13].

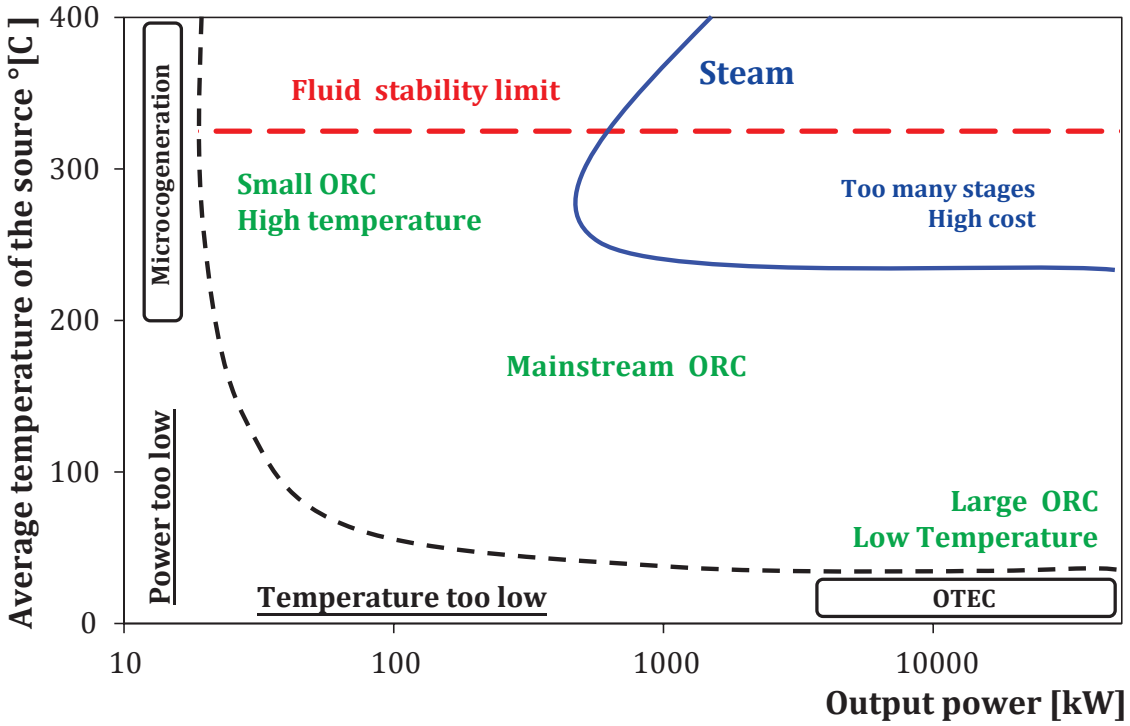

Figure 3: fields of employment for the Rankine cycle **[14]**

1.1.2 Features of the Candidate Working Fluid

The versatility of ORC is principally owed to the working fluid, which may also be a mixture of two or more components [15]. The fluid constituents and concentrations can be tailored to maximize the efficiency of power plants with different applications and configurations.

The selection of organic fluids, instead of steam, leads to desirable thermodynamic and

turbine design features [13]:

- fluids with different critical parameters allows for thermodynamic cycle configurations otherwise inaccessible in the state diagram of water, e.g. supercritical cycles at low maximum temperatures and pressures
- even in the presence of significant differences between the temperatures of the heat source and the cold well, efficient thermodynamic cycles can be achieved through a relatively simple plant set-up, without vapor extraction and perhaps with one expansion stage, thanks to the regeneration that occurs with a de-superheating of the vapor at the turbine outlet
- the turbine generally requires modest peripheral speed and condensation is avoided during the expansion without superheating. The turbine, though, often has supersonic flows with high expansion ratios
- the choice of the fluid influences the volumetric flows, consenting turbine optimization for any power level
- pressure levels and expansion ratios may be chosen with a certain freedom, independently of the temperature levels of the heat source and the cold well, e.g. low temperatures may be associated with high pressures and high temperatures with low pressures

Inevitably, the selection of working fluids brings performance trade-offs, due to the influence of the fluid properties in most components (e.g. different condensation pressures for given saturation temperature cause wide variations in volume flows at the condenser inlet, which directly affect design and dimensions of the expander and the regenerator). Therefore, the assessment of the benefits of a particular solution must be based on the system as a whole [7]. Moreover, the choice of the working fluid is unavoidably influenced by safety and financial concerns. Consequently, it is generally the result of a compromise between the required and the desirable features of the working fluid in Rankine power systems: above all, adequate thermo-physical and thermodynamic properties, compatibility with the materials used in building the plant and the limits of thermal stability of the fluid, the health and safety issues, the fluid's

availability and its cost [16].

1.1.3 Components and Thermodynamic Aspects

The classic configuration of the critical components of an ORC engine and the thermodynamic representation of the cycle in a *T-s* diagram are shown in Figure 4. The working fluid, which may be saturated as in the picture, superheated or even in supercritical conditions [17], is expanded (A → B) generally in a turbine, which in small power units may be substituted with a less expensive scroll expander [18]. In B, the temperature of the fluid might be high enough to include a recuperative heat exchanger, frequently called *regenerator*, in order to cool the vapor (B → C) and preheat the liquid (C → D). In the regenerator, the heat recovered is exploited to preheat (E → F) the liquid originating from the pump (D → E) and heading to the evaporator (F → A), which feeds the working fluid again to the expander.

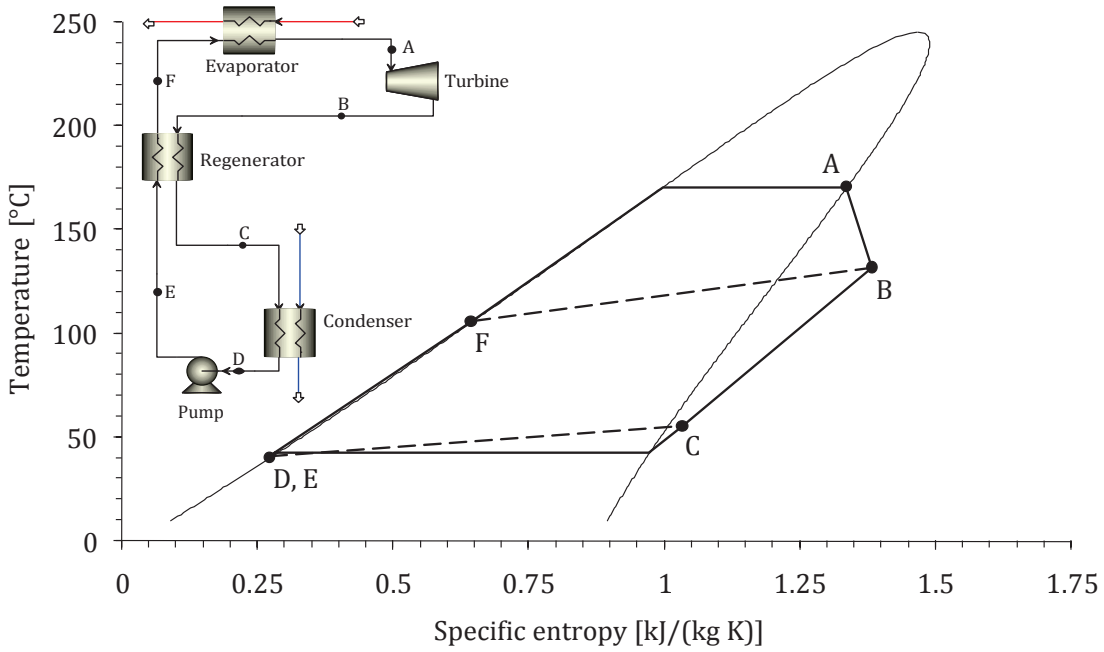

Figure 4: *T-s* diagram and component layout for a hexamethyldisiloxane ORC cycle **[19]**

The molecular structure of the working fluid is strongly related to the shape of the saturation curve in the *T-s* diagram: the slope of the saturated vapor line tend to be negative for fluids with low molecular complexity like water, characterized by the well-

known bell-shaped curve, while is positive for fluids with high molecular complexity [20], as for the siloxane of Figure 4. Often organic fluids have a complex molecular structure, which usually makes the employment of a regenerator necessary to achieve an acceptable thermal efficiency. In fact, the working fluid expands from A to B in the superheated vapor region, moving away from the saturation line. Therefore, a large amount of thermal energy can be recovered from the vapor flow before it enters the condenser, raising cycle performance. This operation improves the cycle efficiency, depending on the performance of the regenerator itself [13]. It should be also noted that a positive slopes makes it possible to avoid superheating the working fluid after the evaporation without concerns of condensation inside the expander.

Phase change in ORC systems cannot always be considered isothermal. *Zeotropic mixtures*, i.e. multicomponent fluids whose composition can be altered through simple distillation, are characterized by a temperature difference between the dew and the bubble temperatures. This *temperature glide* depends on the fluids and their mass fraction in the mixture. In practice, a better thermal match between the heat source and the working fluid results in less irreversibility within the evaporator, limiting the available work lost by the system as a whole [21]. Therefore, the presence of a temperature glide could be useful from the thermodynamic point of view in those cases where the heat source is not intrinsically isothermal, as in the heat recovery of exhausts [13]. Moreover, if a refrigerant with a modest heat capacity is used for condensation, the non-isothermal phase change may still be useful in reducing the mass flow rate necessary [15]. The differences between zeotropic and azeotropic mixtures are qualitatively shown in Figure 5, where diagrams for two ORC optimized for the same heat source are reported.

An improved thermal match with heat source at variable temperature may also be obtained with supercritical heating processes, which are strongly non-isothermal. By changing the composition of the mixture, the critical point varies continually, even in a non-linear fashion [13]. Tis characteristic may prove useful in creating thermodynamic cycles with low critical temperatures and pressures [15].

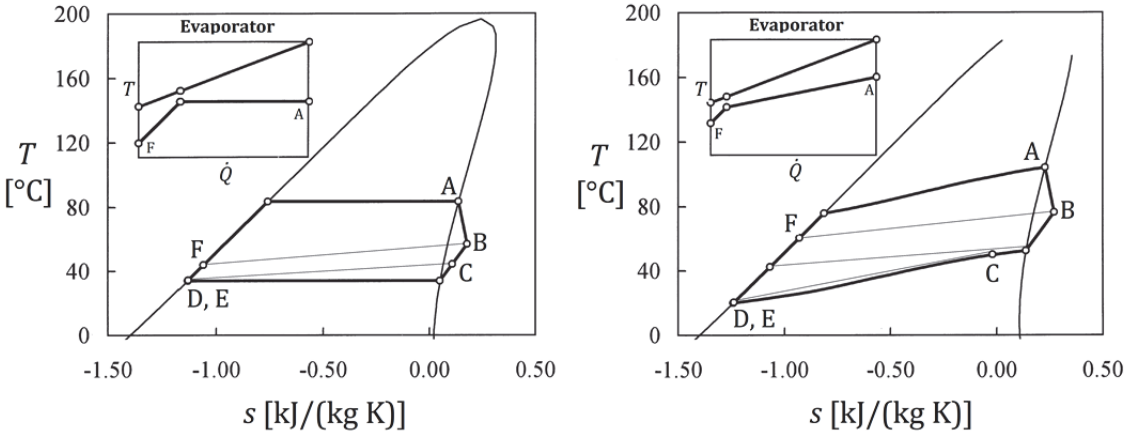

Figure 5: phase change in azeotropic (a) and zeotropic (b) mixtures **[15]**

1.2 Microchannel Heat Exchangers

The literature on heat transfer and fluid-dynamics in small passages is filled with terms to describe channel size (*nano-*, *micro-*, *meso-*, *mini-*, etc.), reflecting the lack of a universally accepted criterion separating microchannels from the conventional scale [22]. However, any flow passage with cross-sectional characteristic dimension less than 1 mm is generally classified as *microchannel* [12]. This definition for microchannel heat exchangers (MCHE) is then adopted throughout the present document and, within this context, the smallest characteristic dimension is considered, e.g. the short side length of a rectangular cross-section.

1.2.1 Thermohydraulic Performance

In heat exchangers, thermal energy (enthalpy) is generally transferred by forced convection between a fluid and a solid surface [23]. Convective heat transfer process for internal flows is described by the following well-known equation written for the differential element of a heat exchanger:

$$\mathrm{d}\dot{Q} = h\,\mathrm{d}A\,(T_w - T_b) = \dot{m}\,c_P\,\mathrm{d}T_b \qquad \textbf{(1.1)}$$

where $\dot{Q}$ is the heat transfer rate, and represents the thermal power exchanged between a fluid at the bulk temperature T_b and the enclosing walls at temperature T_w ; h is the

convective heat transfer coefficient; A is the convective heat transfer surface area, which corresponds to the wall-fluid interface area; c_P is the specific heat at constant pressure of the fluid; $\dot{m}$ is the fluid mass flow rate, which can be expressed as $\dot{m} = \rho\, u\, S$, where u is the fluid mean axial velocity, ρ is the fluid mass density and S is the flow area.

Efforts are made to enhance h and A with constraints on the overall volume and weight, in order to develop compact devices capable of dealing with the desired heat duty in a reduced space. The small passages that constitute MCHE consent to improve both quantities simultaneously [24].

These and other important aspects associated to microchannels can best be outlined with a simple analysis [25]. Consider two channels I and II of different hydraulic diameter D_H and length L, in which flows the same fluid with constant physical properties. Both streams are characterized by the mass flux $G = \rho\, u = \dot{m}_\mathrm{I}/S_\mathrm{I} = \dot{m}_\mathrm{II}/S_\mathrm{II}$ and are submitted to an equal temperature difference ΔT_b between the outlet and the inlet, caused by the heat flux at the channel wall $q = \mathrm{d}\dot{Q}/\mathrm{d}A = \dot{Q}_\mathrm{I}/A_\mathrm{I} = \dot{Q}_\mathrm{II}/A_\mathrm{II}$ constant along the flow direction. With reference to a single channel of type I, the number N_II of channels of type II required to obtain the same total heat transfer rate, surface area, mass flow rate and flow area is:

$$N_\mathrm{II} = \frac{A_\mathrm{I}}{A_\mathrm{II}} = \frac{q\, A_\mathrm{I}}{q\, A_\mathrm{II}} = \frac{\dot{Q}_\mathrm{I}}{\dot{Q}_\mathrm{II}} = \frac{\dot{m}_\mathrm{I}\, c_P\, \Delta T_b}{\dot{m}_\mathrm{II}\, c_P\, \Delta T_b} = \frac{\dot{m}_\mathrm{I}}{\dot{m}_\mathrm{II}} = \frac{G\, S_\mathrm{I}}{G\, S_\mathrm{II}} = \frac{S_\mathrm{I}}{S_\mathrm{II}} \tag{1.2}$$

Then, the ratio of the ratio of the hydraulic diameters holds:

$$\frac{D_{H,\mathrm{I}}}{D_{H,\mathrm{II}}} = \frac{4\, S_\mathrm{I}\; L_\mathrm{I}/A_\mathrm{I}}{4\, S_\mathrm{II}\; L_\mathrm{II}/A_\mathrm{II}} = \frac{N_\mathrm{II}\, L_\mathrm{I}}{N_\mathrm{II}\, L_\mathrm{II}} = \frac{L_\mathrm{I}}{L_\mathrm{II}} \tag{1.3}$$

which means that the flow length is directly proportional to the hydraulic diameter:

$$L \propto D_H \tag{1.4}$$

If the walls have zero thickness, the volume V occupied by the channel is equal to the volume occupied by the fluid, the following expression may be obtained:

$$\frac{A_\mathrm{I}/V_\mathrm{I}}{A_\mathrm{II}/V_\mathrm{II}} = \frac{S_\mathrm{II}\, L_\mathrm{II}\, A_\mathrm{I}}{S_\mathrm{I}\, L_\mathrm{II}\, A_\mathrm{II}} = \frac{L_\mathrm{I}}{L_\mathrm{II}} = \frac{D_{H,\mathrm{I}}}{D_{H,\mathrm{II}}} \tag{1.5}$$

and therefore:

$$\beta = \frac{A}{V} \propto \frac{1}{D_H} \tag{1.6}$$

The ratio of the total transfer area to the total exchanger volume is called the heat transfer surface area density β, which is the most widely used heat exchanger specification related to compactness and surface area enhancement: low D_H implies high β, indicating that more heat transfer area can be made available in a reduced space.

Considering now the Reynolds number *Re*:

$$Re = \frac{\rho\, u\, D_H}{\mu} = \frac{G\, D_H}{\mu} \propto D_H \tag{1.7}$$

where μ is the fluid dynamic viscosity. Hence, *Re* decreases with the hydraulic diameter, so that at smaller scale the flow tends towards the laminar region [21]. The critical Reynolds number for a laminar condition to prevail depends on the surface geometry itself: for straight smooth channels it is generally safe to assume that the laminar condition will apply for $\mathrm{Re} < 2200$, while some surfaces designed to avoid boundary layer formation and enhance heat transfer may have transitional or turbulent flow at Reynolds numbers as low as about 300 [21].

For laminar flows, under several assumptions that will be listed in Section 1.2.2, the continuity, the momentum and the energy equations can be analytically solved, and constant asymptotic values are obtained for the Nusselt number *Nu* and the Poiseuille number *Po*, which are defined as:

$$Nu = \frac{h\, D_H}{k} = constant \tag{1.8}$$

$$Po = f\, Re = constant \tag{1.9}$$

where *k* is the thermal conductivity of the fluid; *f* is the Fanning friction factor.

Rearranging the definition of *Nu*, the improvement in the heat transfer coefficient employing microchannels becomes clear:

$$h = \frac{Nu\ k}{D_H} \propto \frac{1}{D_H} \tag{1.10}$$

Then the temperature difference between the wall and the fluid does not vary along the flow direction and is reduced for smaller hydraulic diameters, as a result of the heat transfer coefficient enhancement:

$$(T_w - T_b) = \frac{q}{h} = \frac{q\ D_H}{Nu\ k} \propto D_H \tag{1.11}$$

Also the axial temperature gradient is constant along the flow direction, in fact, since the wall flux is independent of the axial coordinate x as the flow area:

$$\frac{\mathrm{d}T_b}{\mathrm{d}x} = \frac{q}{\dot{m}\ c_P}\ \frac{\mathrm{d}A}{\mathrm{d}x} = \frac{q}{\dot{m}\ c_P}\ \frac{\mathrm{d}\left(\frac{4\ S\ x}{D_H}\right)}{\mathrm{d}x} = \frac{4\ S\ q}{D_H\ \dot{m}\ c_P} = \frac{q\ A}{\dot{m}\ c_P\ L} = \frac{\Delta T_b}{L} \propto \frac{1}{D_H} \tag{1.12}$$

Therefore, if the fluid temperature does not vary significantly on the small cross-section, a considerable temperature difference may occur between the inlet and the outlet, in the case of in microchannels with considerable flow length [25].

The length of the channels is important also in relation to the frictional pressure drop, in fact:

$$\Delta p_{fr} = \int_0^L \frac{1}{2}\ \rho\ u^2\ \frac{4\ f}{D_H}\mathrm{d}x = \int_0^L \frac{2\ G^2}{\rho\ D_H}\ \frac{Po}{Re}\mathrm{d}x = \frac{2\ \mu\ G\ Po}{\rho\ D_H^2}\int_0^L \mathrm{d}x = \frac{2\ \mu\ G\ Po\ L}{\rho\ D_H^2} \tag{1.13}$$

Considering again I and II it holds:

$$\Delta p_{fr} \propto \frac{1}{D_H} \tag{1.14}$$

which shows that the improvement in thermal performance achieved reducing the channel size is accompanied by deterioration in hydraulic performance [24]. As a consequence, the designer must find a compromise between these two aspects. The degrees of freedom are numerous: for example, considering a third channel III related to I through the same assumption for II with the exception of imposed Δp_{fr} instead of G, it leads to:

$$N_{\mathrm{III}} = \frac{A_{\mathrm{I}}}{A_{\mathrm{III}}} = \frac{\dot{Q}_{\mathrm{I}}}{\dot{Q}_{\mathrm{III}}} = \frac{\dot{m}_{\mathrm{I}}}{\dot{m}_{\mathrm{III}}} = \frac{G_{\mathrm{I}}\, S_{\mathrm{I}}}{G_{\mathrm{III}}\, S_{\mathrm{III}}} = \frac{S_{\mathrm{I}}}{S_{\mathrm{III}}} \sqrt{\frac{D_{H,\mathrm{I}}}{D_{H,\mathrm{II}}}} \tag{1.15}$$

where the following relationship is used:

$$G = \frac{\rho\, D_H^2\, \Delta p_{fr}}{2\, \mu\, Po\, L} = \frac{2\, \rho\, S\, D_H\, \Delta p_{fr}}{\mu\, A\, Po} \propto \frac{S\, D_H}{A} \implies \frac{G_{\mathrm{I}}}{G_{\mathrm{III}}} = \frac{S_{\mathrm{I}}\, D_{H,\mathrm{I}}}{N_{\mathrm{III}}\, S_{\mathrm{III}}\, D_{H,\mathrm{III}}} \tag{1.16}$$

Then it holds

$$L \propto D_H^{1.5} \tag{1.17}$$

From (1.4) and (1.17), if $D_{H,\mathrm{III}} = D_{H,\mathrm{II}}$, which also implies $S_{\mathrm{III}} = S_{\mathrm{II}}$ if the cross-sectional shape is maintained:

$$\frac{L_{\mathrm{III}}}{L_{\mathrm{II}}} = \frac{L_{\mathrm{I}} \left(\frac{D_{H,\mathrm{II}}}{D_{H,\mathrm{I}}}\right)^{1.5}}{L_{\mathrm{I}} \frac{D_{H,\mathrm{II}}}{D_{H,\mathrm{I}}}} = \sqrt{\frac{D_{H,\mathrm{II}}}{D_{H,\mathrm{I}}}} < 1 \tag{1.18}$$

$$\frac{N_{\mathrm{III}}}{N_{\mathrm{II}}} = \frac{A_{\mathrm{II}}}{A_{\mathrm{III}}} = \frac{\frac{4\, S_{\mathrm{II}}\, L_{\mathrm{II}}}{D_{H,\mathrm{II}}}}{\frac{4\, S_{\mathrm{II}}\, L_{\mathrm{III}}}{D_{H,\mathrm{II}}}} = \sqrt{\frac{D_{H,\mathrm{I}}}{D_{H,\mathrm{II}}}} > 1 \tag{1.19}$$

and with (1.15) and (1.16):

$$\frac{Re_{\mathrm{III}}}{Re_{\mathrm{II}}} = \frac{u_{\mathrm{III}}}{u_{\mathrm{II}}} = \frac{G_{\mathrm{III}}}{G_{\mathrm{II}}} = \frac{G_{\mathrm{III}}}{G_{\mathrm{I}}} = \sqrt{\frac{D_{H,\mathrm{II}}}{D_{H,\mathrm{I}}}} < 1 \tag{1.20}$$

Therefore the pressure drop can be contained using a larger number of shorter channels, which provides augmented total flow area $N_{\mathrm{III}}\, S_{\mathrm{III}}$ and reduced fluid velocity. Since L and the flow area vary significantly, it is clear that the shape of the heat exchanger as a whole changes as the hydraulic diameter is reduced.

This is how I would have done this few sentences:

With the assumptions for channel III, it can be easily shown that (1.6) holds true. However, while calculating the heat transfer surface area density, the wall thickness is

not considered. The thickness of the walls contributes to the exchanger volume, which is the denominator of (1.6). Generally, due to manufacturing and/or operational constraints, in small passages the wall thickness is comparable to the hydraulic diameter, and sometimes even larger. Hence, if the wall thickness has reached its lower limit, a hydraulic diameter below which β starts to decrease must exist. This concept will be further developed for rectangular channels in Section 2.2.2.

1.2.2 Scaling Effects

Many recent works on forced convection through microchannels report discrepancies between experimental data and the well-established theory, claiming that laws governing transport phenomena within passages of macroscopic dimensions are not suitable to evaluate pressure drop and convective heat transfer coefficients in microchannels. New phenomena specific to the small scale are sometimes invoked to explain the inconsistency between the empirical results and the conventional correlations [26].

In the last few years, this conclusion seems to be controverted by additional, more accurate experimental data. The open literature nowadays seems to indicate that a large part of the results obtained for microchannels can be completely explained applying in a right way the existing theory and correlations, considering that certain known effects can be of different importance in macro- or microsystems [27] [28].

For instance, in single-phase forced convection Equations (1.8) and (1.9) hold true under the following assumptions [29]:

- the fluid can be treated as a continuum medium
- steady fully developed laminar flow
- simplified boundary conditions
- simple geometries with smooth surfaces
- the physical properties are independent of temperature and pressure
- the heating due to viscous dissipation can be neglected

- the heat conduction in the fluid in the flow direction can be neglected
- no electromagnetic effects take place

In microchannels, depending on whether the flow is liquid or gaseous, some of the above assumptions may no longer be acceptable. The so-called *Scaling effects* are defined as those effects that may be neglected at the reference geometrical scale, but which become important when the scale changes. The reformulation of the conservation equations and/or their associated boundary conditions may be required as the characteristic scale of the system is reduced. The magnitude of these phenomena should be determined in order to assess the validity of the constant Nu and Po hypothesis [30] [31] [32].

A brief description of the main effects that may arise in single-phase flows inside microchannels is reported below. Notice that the scale of the system is of primary importance as the conditions required to ignore these effects involve the characteristic dimension of the cross-section and/or the channel length and/or the Reynolds number.

Rarefaction Effects

Shrinking down the dimensions of microfluidic systems dealing with internal gas flows, the free path of the fluid molecules may become comparable to the characteristic dimension of the passages, even at standard pressure and temperatures. The fluid then can no longer be treated as a continuum and the behavior of the single molecules comes to be predominant. It should be noted that rarefaction effects are usually irrelevant for liquids [29].

The ratio of the mean free path λ to the smallest characteristic dimension Dc is called the Knudsen number Kn. Many collision models are available to evaluate λ [22], among which the hard sphere model is a cautious choice, since particle interactions are considered to occur only at null relative distance, overestimating as a consequence the mean free path. The Knudsen number may then be written as:

$$Kn = \frac{\lambda}{D_C} = \frac{1.277}{\sqrt{\frac{R}{M}\,T}}\,\frac{\mu(T)}{\rho\,D_C} = 1.277\,\frac{\mu(T)}{D_C}\,\sqrt{\frac{R}{M}\,\frac{T}{p^2}} \qquad \textbf{(1.21)}$$

where R is the universal gas constant; M is the molar mass of the gas; T is the absolute temperature. It should be noted that the last equality holds true only for an ideal gas. Nevertheless it shows the dependence of the rarefaction effect from temperature and pressure.

Based on the magnitude of the Knudsen number, four different flow regimes are identified [22]:

- for $\mathrm{Kn} < 10^{-3}$ the flow is a *continuum flow* and it is accurately modeled by the classical theory with no-slip boundary conditions
- for $10^{-3} < \mathrm{Kn} < 10^{-1}$ the flow is a *slip flow* and the classical equations remain applicable, provided a velocity slip and a temperature jump are taken into account at the walls. These new boundary conditions point out that rarefaction effects become sensitive at the wall first. Since the velocity and temperature fields are modified with respect to the continuum flow, pressure drop and heat transfer inevitably influenced: correction factors for *Po* are available in [33], while several correlations for *Nu* are provided in [34]
- for $10^{-1} < \mathrm{Kn} < 10$ the flow is a *transition flow* and the continuum approach is no longer valid. However, the intermolecular collisions are not yet negligible and should be taken into account. The Monte Carlo method or the Lattice-Boltzmann model may be employed in this range: the molecules are treated in large groups, still considerably smaller than the smallest length scale of the simulation in question [29]
- for $\mathrm{Kn} > 10$ the flow is a *free molecular flow* and the occurrence of intermolecular collisions is negligible compared with the one of collisions between the gas molecules and the walls. Molecular dynamics models are available, however, the computational demands of resolving individual molecules are so heavy that only very small volumes can be addressed [29]

Entrance Effects

At the entrance of a heated or cooled channel, the flow is not hydrodynamically nor thermally developed, and the Poiseuille and Nusselt numbers are typically greater that the corresponding asymptotic values. Therefore these contributions can be ignored only if the velocity and the temperature profile stabilize within a short distance from inlet when compared to the entire channel length. This means that the channel length must be large when compared to the hydrodynamic entrance length L_{HD} and to the thermal entrance length L_{TH}. These two quantities can be expressed as:

$$L_{HD} = \kappa_{HD}\, D_H\, Re \tag{1.22}$$

$$L_{TH} = \kappa_{TH}\, D_H\, Re\, Pr \tag{1.23}$$

where κ_{HD} and κ_{TH} are constants that depend only on the cross-sectional shape: κ_{HD} may be found in tables, while κ_{TH} may be calculated from the definition and information on the local Nusselt number [23]; Pr is the Prandtl number, defined as:

$$Pr = \frac{\mu\, c_P}{k} \tag{1.24}$$

To neglect the entrance effect on pressure drop, the following condition should be verified [35]:

$$\frac{L}{D_H} > 60 \iff \frac{L_{HD}}{L} < \frac{\kappa_{HD}\, Re}{60} \tag{1.25}$$

while heat transfer is not influenced if [27]:

$$Re\, Pr \frac{D_H}{L} < 10 \iff \frac{L_{TH}}{L} < 10\, \kappa_{TH} \tag{1.26}$$

Several correlations are available for Po and Nu in hydrodinamically, thermally or simultaneously developing flows [36] [37] [38] but, due to their complexity, tables and charts [21] [22] [23] may sometime be a quicker instrument.

Conjugate Heat Transfer

In microflows, the thermal energy transferred by conduction in the solid and in the axial

direction of the flow may be of the same order of magnitude as the energy exchanged by convection with the fluid. Temperature profiles and heat transfer may be strongly influenced, affecting the boundary conditions [39].

Conjugate effects may be neglected if the heat transfer rate by conduction in the solid walls is negligible with respect to the thermal power exchanged by convection [39], that is to say if:

$$\Lambda = \frac{k_w\, A_w}{\dot{m}\, c_P\, L} = \frac{k_w\, A_w \frac{\Delta T}{L}}{\dot{m}\, c_P \Delta T} < 0.01 \qquad \textbf{(1.27)}$$

where Λ is the longitudinal heat conduction parameter; k_w is the wall thermal conductivity; A_w is the heat transfer surface area available to longitudinal conduction and coincides with the total wall cross-sectional area, perpendicular to the flow direction.

Conjugate heat transfer becomes significant in compact heat exchangers, characterized by reduced L and often elevated values of A_w, due to the manufacturing constraints on the wall thickness. Crossflow configurations are particularly exposed to the phenomenon, which assume a two-dimensional connotation [23]. Finally, it can be easily shown that Λ is amplified at low Reynolds numbers [27], typical of microchannels; in fact:

$$\Lambda = \frac{k_w\, A_w}{\dot{m}\, c_P\, L}\ \frac{\frac{\mu\, c_P}{k}}{Pr}\ \frac{\frac{4\,\dot{m}\, L}{\mu\, A}}{Re} = \frac{4}{Re\, Pr}\ \frac{k_w}{k}\ \frac{A_w}{A} \qquad \textbf{(1.28)}$$

It will be shown that conjugate effects should be considered, as they have strong influence on the case study. A few models are available [23] [39]; the one presented in [40] is chosen for being accurate, versatile and fairly simple at the same time.

Surface Roughness

In the microscale it is practically impossible to produce what would be generally considered as a smooth surface, because the average height ϵ of the surface irregularities

may not be negligible compared to the smallest duct characteristic dimension. Usually *Nu* and *Po* for fully developed laminar flow are not influenced as long as the following condition is respected:

$$\frac{\epsilon}{D_C} < 0.01 \tag{1.29}$$

Otherwise, the surface roughness changes the effective flow cross-sectional geometry, which in turn affects heat transfer and pressure drop [23]. Moreover, earlier transition to turbulent flow may be induced, which could explain some results showing dependence on Reynolds number for both *Nu* and *Po* even at $\mathrm{Re} < 2200$ [41].

Both Nusselt and Poiseuille numbers grow with surface roughness, correlation and plots can be found for example in [42] [43]. However, the drawbacks from the increased friction factor usually overcome the enhancement in the heat transfer coefficient. This conclusion, though, is reversed when microchannels are deliberately fabricated with protrusions for heat transfer improvement purposes [42].

Variable Properties

The assumption of constant ρ, μ, k and c_P allows to solve independently the momentum equation for the pressure field and the energy equation for the temperature field inside the channel. On the contrary, the two equations are coupled if the physical properties are strong functions of temperature and pressure [44].

The variation with T or p for the generic property ψ can be neglected if the following conditions [25] are respected:

$$\left|\left(\frac{T}{\psi}\frac{\partial\psi}{\partial T}\right)_{T_r}\right| \ll 1 \tag{1.30}$$

$$\left|\left(\frac{p}{\psi}\frac{\partial\psi}{\partial p}\right)_{p_r}\right| \ll 1 \tag{1.31}$$

where the terms between the absolute value designators are sensitivity coefficients calculated at an appropriate reference temperature T_r and pressure p_r. In the opposite

situation, heat transfer and frictional losses can be heavily influenced by property variation [45] [46].

For what concerns temperature dependent properties, the variation along the flow direction may play an relevant role in the small scale. In fact, according to Equation (1.12), the axial temperature gradients become large when the channel size is reduced [25]. Consequently, the constant properties assumption may not be a good approximation even in relatively short channels: in this case, the heat exchanger should be ideally subdivided into zones with limited axial temperature difference, in which properties do not vary significantly [23].

On the contrary, in microchannels the temperature difference the direction perpendicular to the flow can generally be neglected [25]. Considering Equation (1.11) it is clear that at the small scale the temperature becomes more uniform over the cross-section. Nevertheless, corrections may be applied to *Nu* and *Po* employing the property ratio method available in [23].

Equation (1.13) shows that, for small passages, the pressure difference between the inlet and the outlet could be considerable. However, as discussed in Section 1.2.1, pressure drop can be contained increasing the total flow area and reducing the fluid velocity, and the variation of physical property dependence on pressure may often be ignored, coherently to what is reported in [25] [47].

Viscous Dissipation

The dissipation function is usually neglected in the energy equation. However, when the hydraulic diameter is very small, the internal heat generation due to the viscous forces may produce a significant temperature rise that can remarkably influence the heat transfer. The Brinkmann number *Br*, which can be seen as the ratio of the viscous heating rate to the average heat transfer rate by convection, is usually employed to evaluate if the viscous heating effects can be influential. The following inequality should be satisfied in order to neglect viscous heating:

$$Br = \mu\, u^2 \frac{L}{\dot{Q}} < 0.05 \frac{D_H^2}{2\, S\, Po} \tag{1.32}$$

This condition is obtained imposing a small temperature rise caused by viscous dissipation inside the fluid when compared to the temperature difference due to convection. If it does not hold true, the Nusselt number should be corrected as a function of *Br* as described in [48].

The effects of the Brinkman number on Nusselt number depend on the characteristics of the boundary conditions: for flows with constant wall temperature, *Nu* increases, because of viscous heating effects, to a value that is not dependent on *Br*; for flows with constant wall heat flux, *Nu* decreases as *Br* number increases [29].

Fluid Axial Conduction

In the energy equation, the term related to heat transfer by conduction in the fluid and in the axial direction can generally be neglected with respect to the convective term. This is mathematically expressed through the Peclét number *Pe* as:

$$Pe = Re\, Pr = \frac{\rho\, c_P\, u\, D_H}{k} > 100 \tag{1.33}$$

In fact, for small *Pe*, conduction becomes the dominant mechanism for heat transfer: in this situation, the thermal entrance length is heavily reduced and the Nusselt number inside the channel becomes sensible to upstream and downstream conditions [49]

Electroviscous Effect

Solid non-conductive materials may acquire a relative electric charge when in contact with polar liquids. If the liquid contains ions, e.g. due to impurities, the surface charges will attract the opposite ions. Stream-induced currents and potentials differences are generated along the flow direction following the radial redistribution of charges, in zones characterized by different fluid velocity. The overall result is an additional drag force which increases the pressure drop and also affects heat transfer [50].

This effect may become non-negligible in the small scale, as shown by the models

available in literature [51] [52]. However, if the channel walls are not charged relatively to the liquid and/or if the bulk ionic concentration is close to zero, this complex phenomenon can be ignored, regardless of the characteristic dimension [53].

1.2.3 Fabrication Techniques

Ultra-compact structured surfaces such as microchannels or microfins can be fabricated through several different processes and from a broad variety of materials including glasses, polymers, metals, ceramics, and semiconductors [11]. When selecting the manufacturing technology for compact heat exchangers, the important factors to consider are [54]:

- desired channel cross-sectional shape, aspect ratio and other geometric constraints
- compatibility of channel interior surface materials with the working fluid
- interior wall roughness
- complexity and cost of fabrication
- maximum pressure and temperature ratings of various materials used, including those applied for bonding

A few manufacturing techniques suitable to obtain metal-based microstructures will be now briefly outlined. Each method grants typical minimum feature dimension of a few nanometers with tolerances below 1 μm. High aspect ratios of 10 or more are feasible and the maximum size of the workpiece on which the compact structures are obtained can be of several hundreds of square centimeters [54].

Micro-machining is a category of processes available for micro heat exchangers fabrication which covers any technique where tools are used to cut, bond, form, deform or remove material to create channels or heat exchanger assemblies. The only limitation is on materials, which need to be soft and ductile enough to be machined [55].

Dry etching involves the vaporization of the solid surface, physically by ion

bombardment, chemically by the contact with a reactive species, or by the combined use of both mechanisms. A mask is used to transfer the desired pattern on the surface with high precision. [54].

LIGA process, from the German acronym for lithography, molding and electroplating, employs X-rays emitted onto a suitable photo-resist material that has been bonded to a conductive substrate material. A mask positioned between the X-ray source and the workpiece enables the X-ray projection to take the shape of the final design. The conductive substrate and photo-resist material are then immersed in a nickel ion solution bath. The nickel in solution is electroplated onto the photo-resist material with the pattern arranged by the mask. The nickel structure can then be directly used or employed as a mold for other materials. This process can be repeated several times and the final products may be bonded together to create more complex builds [54].

Recently, high temperature compression molding was used to produce cost-effective layers of aluminium and copper based high-aspect-ratio microscale structures [56] characterized by a surface roughness height in the order of 10 μm. The layers were then stacked up and joined together by eutectic bonding [57] to form arrays of rectangular microchannels 150 μm wide and 400 μm high, spaced by 750 μm thick walls. Molding replication seems then an interesting option for microchannel heat exchangers fabrication [58], and each manufacturing method described above may be employed to create the mold.

1.3 Motivation and Scope

As already mentioned, microchannels heat exchangers are ideal candidates for mobile applications due to several features: high ratio of surface area to volume, low thermal resistances, small volumes, low total mass and low inventory of working fluids [11]. However, the open literature provide extremely limited information on MCHE for applications in the range of several kW_{th} , typical of waste heat recovery systems for heavy-duty vehicles.

Only one relevant document [59] could be found, in which a 5 kW_{th} microchannel regenerator for an ORC system is described. The device, characterized by a mass flow rate around 0.04 kg/s, was tested and rated with promising results: as expected, the employ of microchannels led to enhanced heat transfer but also increased pressure drop when compared to a plate heat exchanger (PHE). Nevertheless, as noted by the authors and as shown in Section 1.2.1, it is certainly possible to optimize the MCHE and improve its performance.

In order to assess the potential of microchannel technology in mobile ORC systems, it is therefore important to develop a suitable optimization method. The scope of the present thesis is to obtain an optimized microchannel regenerator; the device must be smaller and lighter with respect to the state-of-the-art solutions.

A plate heat exchanger is a common choice [6] [59] in similar situations, even though it is doubtfully the best option for gas-to-liquid exchanger [23]. Often, a PHE, even if optimized for the application, is still more voluminous than desirable [6]. The compactness of the device is generally limited by the pressure drop on the gas-side, which is often several orders of magnitude higher than on the liquid-side. In fact, in PHE the two sides are similar, and often identical, in term of heat transfer surface area and flow area; high gas velocity is then needed to ensure turbulent flow with high heat transfer coefficient [60], comparable to that of the liquid. If the total flow area is increased, as suggested in Section 1.2.1, in order to reduce the flow velocity and therefore the pressure drop, the heat transfer coefficient will diminish, making it necessary to enhance the surface area, which evidently penalizes the compactness.

A microchannel heat exchanger manufactured as described in Section 1.2.3 can be classified as a laminar flows plate-fin heat exchanger (PFHE). Such a device is a better alternative to PHE, since surface areas and pressure drop may be redistributed on the two sides adjusting the size and/or the aspect ratio of the channels formed between the fins. In this way, it possible to increase the compactness complying with the hydraulic constraints imposed by the other components of the heat recovery system, compensating for the lower gas-side heat transfer coefficient with greater surface area than on the liquid side.

2 Method

As already mentioned, the studied microchannel heat exchanger (MCHE) can be classified as a plate-fin heat exchanger (PFHE). Such a device can be directly sized for given maximum pressure drop allowed on the gas-side (usually the most critical), provided that the extended surface features are known for both sides [23]. This would require to pre-determine the dimensions and the number of the rectangular channels, optimized according to some desired objective function.

Unfortunately, guidelines to accomplish the task are particularly scarce in the open literature: often the choice of the microchannel dimension is not justified [61], sometimes simply concluding that «there is sizable design space to optimize the dimensions» [59]. In other papers, only few parameters are considered in the selection process [62] [63] [64]. However, the general approach is to iteratively assign values to the design parameters and rate the resulting exchangers [65] [66], which must satisfy constraints imposed by the manufacturing method [67] [68] [69].

It is always possible to reduce the sizing problem to an iterative rating problem by tentatively specifying the dimensions and other design parameters to calculate the performance [23]. This method is particularly suitable to test different surfaces and select the best one, but it can be computationally demanding even for simple geometries, due the numerous design parameters. Therefore, particular attention is given

to reducing the number of operations at each iteration and to selecting appropriately small intervals for each parameter, which constitute the design space where the optimal values are searched.

The design space is defined by constraints imposed by the manufacturing method and by other components of the ORC system. Genetic algorithms may prove useful in similar situations [70], but two different formulations of the problem were attempted with no satisfying results in acceptable computational time and the tool was abandoned. The design space is then discretized to obtain, for each design parameter, a finite number of values, among which the optimal ones are searched. All the combinations of the candidate values are tested in order to obtain first attempt solutions. Some of these rough designs are then selected for refinement.

As described in Section 1.2.2, the thermohydraulic behavior of microflows is increasingly complicated by scaling effects as the passage dimension is reduced. However, as reported in Table 1, the case study involves a heat load and a mass flow rate with no precedents in the open literature, almost one order of magnitude higher than the quantities reported in [59] and in Section 1.3. It is then easy to imagine that a suitable microchannel heat exchanger will not feature extremely small passages: the scaling effects are therefore expected to have weak influence on the thermohydraulic behavior of the MCHE. As a consequence, the assumptions listed at the beginning of Section 1.2.2 are supposed true for a fast, simple optimization process implemented in MATLAB. The resulting design will then be then rated in the next chapter in order to assess the validity of the hypotheses.

An exception must be made for conjugate effects: in fact, as shown in Section 1.2.2, wall longitudinal heat conduction has a particularly strong impact on compact crossflow heat exchangers, characterized by reduced flow length, elevated total wall cross-sectional area and low Reynolds numbers. Since the microchannel heat exchanger to optimize falls into this case, the mathematical model implemented in the selection process must include conjugate heat transfer.

The optimization process developed in the following sections considers both the

crossflow and the counterflow arrangement. If the desired exchanger effectiveness is below 80 %, a crossflow configuration is the most suitable choice, due to greater flexibility in managing the heat transfer surface area, the flow area, the flow length and the pressure drop of each side. Similar devices are already commercially available from manufactures such as Modine for automotive and air-conditioning applications [71]. Thermodynamically, the effectiveness of the crossflow exchanger is between those of the counterflow and parallelflow arrangements. Therefore, in the case of high desired effectiveness, counterflow unit is advised, because the size penalty for the crossflow exchanger may become excessive; as a drawback, the design of the distribution elements may become challenging [23].

2.1 Input Data

The microchannel heat regenerator is optimized for a specific waste heat recovery system based on an ORC turbogenerator. This system, suitable for a heavy-duty truck engine, was targeted in a recent feasibility study [6] carried out within a cooperative project funded by the Austrian Research Promotion Agency involving the Graz University of Technology, the Delft University of Technology, and two large European automotive original equipment manufacturers. The authors consider the plate heat exchangers (PHE) employed as more voluminous than desirable, but the specifications are omitted in the paper due to a non-disclosure agreement with the private companies. A commercial optimization code is then employed to produce a benchmark PHE to which the MCHE can be compared.

2.1.1 Benchmark Plate Heat Exchanger

The PHE to be used for comparison with the optimized MCHE is designed employing proprietary software, Aspen EDR, to which the operating conditions of the heat exchanger used in [6] are fed. The specifications of interest are reported in Table 1. As anticipated in Section 1.3, the pressure drop on the cold-side is negligible with respect to the losses on the hot-side. The cold-side of the heat exchanger corresponds to the liquid-side and the hot-side to the gas-side.

Table 1: specifications of the benchmark plate heat exchanger

Specification	**Cold-side**	**Hot -side**	**Unit**
Inlet temperature	373.15	487.15	K
Outlet temperature	451.56	398.15	K
Inlet pressure	392000	8700	Pa
Pressure drop	6	3220	Pa
Fluid velocity	0.01	17.18	m/s
Heat transfer coefficient (mean)	81.9	88.1	$W/(m^2\ K)$
Heat transfer rate	35.59		kW
Mass flow rate	0.266		kg/s
UA	1143		W/K
Effective MTD	31.13		K
NTU	2.86		#
ε	0.7807		#
Number of plates	41		#
Plate thickness	0.6		mm
Plate pitch	5.28		mm
Plate length	1596		mm
Plate width	495		mm
Stack height	222		mm
Heat transfer surface area	26.96		m^2
Heat transfer surface area density	427		m^2/m^3
Volume of metal	0.01889		m^3
Fluid charge	58.6		kg
Overall dimensions	222×495×1596		m^3

Data from Table 1 can be used for comparison with both an aluminium-based and a copper-based MCHE, since the thermal conductivity of the material composing the plates has negligible effect on the reported numerical values. In fact, for the PHE, the longitudinal heat conduction parameter is in the order of 10^{-3} and conjugate effects can be ignored, as follows from (1.27). Moreover, the wall thermal resistance is three orders of magnitude lower that the convective resistance and has then no significant influence on the overall heat transfer coefficient.

Using the data of Table 3 and Table 1, some upper bounds may be defined:

$$\omega_{max} = \begin{cases} 0.01889 \cdot 2630 + 58.6 = 108.3 \text{ [kg]} & \text{for A360} \\ 0.01889 \cdot 8300 + 58.6 = 215.4 \text{ [kg]} & \text{for C878} \end{cases} \tag{2.1}$$

$$\Delta p_{max} = 3220 + 6 = 3226 \text{ [Pa]} \tag{2.2}$$

which represent, respectively, the maximum weight and pressure drop allowable to be used in the optimization process.

The heat capacity rates can be determined from the data of Table 1:

$$C_{max} = c_{P,c}\, \dot{m} = \frac{\dot{Q}}{T_{c,out} - T_{c,in}} = 453.8 \left[\frac{W}{K}\right] \tag{2.3}$$

$$C_{min} = c_{P,h}\, \dot{m} = \frac{\dot{Q}}{T_{h,in} - T_{h,out}} = 399.8 \left[\frac{W}{K}\right] \tag{2.4}$$

$$r = \frac{C_{min}}{C_{max}} = \frac{T_{c,out} - T_{c,in}}{T_{h,in} - T_{h,out}} = 0.8810 \tag{2.5}$$

where, the subscripts $_c$ and $_h$ denote quantities referred to the cold-side and to the hot-side respectively, while the subscripts $_{in}$ and $_{out}$ refer to the inlet or outlet cross-section of the channels.

It is then possible to obtain the required heat exchanger effectiveness, defined as:

$$\varepsilon = \frac{c_{P,h}\,\dot{m}}{C_{min}}\,\frac{(T_{h,in} - T_{h,out})}{(T_{h,in} - T_{c,in})} = \frac{T_{h,in} - T_{h,out}}{T_{h,in} - T_{c,in}} = 0.78070175 = \varepsilon_{min} \qquad \textbf{(2.6)}$$

It should be noted that the value of the thermal power exchanged in the regenerator calculated in [6] is 5 % higher than the values computed with the Aspen software bundle for the benchmark PHE. This incongruity is probably due to a different thermodynamic library exploited in the automated procedure used by the authors to size their PHE. Different values of the specific heat at constant pressure also slightly modify the outlet temperature of the cold-side. However, the exchanger effectiveness, as defined in (2.6), is not affected by this error and will be used as thermal requirement to satisfy.

2.1.2 Materials and Physical Properties

The working fluid is D4, a cyclic siloxane [6]; the physical properties of the organic fluid at inlet pressure are obtained from the NIST database through the software Aspen Properties. For each side of the MCHE, the properties are averaged with an arithmetic mean between the values at the inlet and outlet temperatures, as the pressure dependence is small enough to be neglected. The averages of interest for the case study are reported in Table 2, along the corresponding values calculated at the inlet and outlet temperatures.

Table 2: physical properties of the working fluid

Property	Cold-side			Hot-side			Unit
	Inlet	Outlet	Mean	Inlet	Outlet	Mean	
Specific heat at constant pressure	1589	1822	1706	1612	1392	1502	J/(kg K)
Density	866.85	767.38	817.12	0.64	0.79	0.72	kg/m^3
Viscosity	0.7194	0.3583	0.5389	0.0102	0.0083	0.0093	g/(m s)
Thermal conductivity	0.0940	0.0764	0.0852	0.0195	0.0136	0.0165	W/(m K)

It should be mentioned that the arithmetic averages of the specific heat at constant pressure of Table 2 satisfy almost perfectly equations (2.3) and (2.4), meaning that $c_{P,h}$

and $c_{P,c}$ are closely linear functions of the temperature. According to the thermodynamic library employed, in the considered temperature range all the properties of interest behave likewise. If also the fluid temperature is roughly linear with the axial coordinate of the flow, the arithmetic averages of Table 2 are a suitable approximation of the real conditions inside the heat exchanger.

As pointed out in Section 1.2.3, copper and aluminium alloys are suitable candidates for microchannel heat exchanger cores. Following the guidelines of the NADCA, the alloys commercially designated as A360 and C878 are selected considering the behavior at high temperature (tensile and yield strengths after prolonged heating at testing temperature up to 260 °C; coefficient of thermal expansion; mold-filling capacity; anti-soldering to the mold). The physical properties of interest, at 20 °C since more precise data could not be found, are retrieved from [72] and are reported in Table 3.

Table 3: physical properties of the solid walls

Property	**A360**	**C878**	**Unit**
Density	2630	8300	kg/m^3
Thermal conductivity	113	27.7	$W/(m\,K)$

2.2 Core Geometry

The core of the MCHE, qualitatively shown in Figure 1, comprises N_m identical modules for the cold-side alternated with $(N_m - 1)$ modules for the hot-side, so that the first and the last module are at the lowest temperature possible, a common practice to minimize the heat losses to ambient [23]. Each module consists in a flat rectangular plate of thickness δ, which constitutes the dividing wall that separates the two sides, and several plain rectangular fins of thickness φ, formed directly on the plate.

When the modules are stacked up and bonded together, N_c and N_h rectangular channels are formed between the fins of the cold- and the hot-side respectively; an additional flat plate with no fins is needed to close the module at the top of the pile. The stack length is

L_m while the channels height, width and length are c, d and L_c for the cold-side, and l, s and L_h for the hot-side. The modules can be piled in crossflow or counterflow configuration; however, since the required effectiveness in (2.6) is lower than 80 %, a crossflow configuration may be the best choice [23], as follows from the discussion of Section 1.3. In this case, the channel lengths on the hot- and cold-side are not necessarily equal and, together with the stack lengths, determine the dimensions of the core.

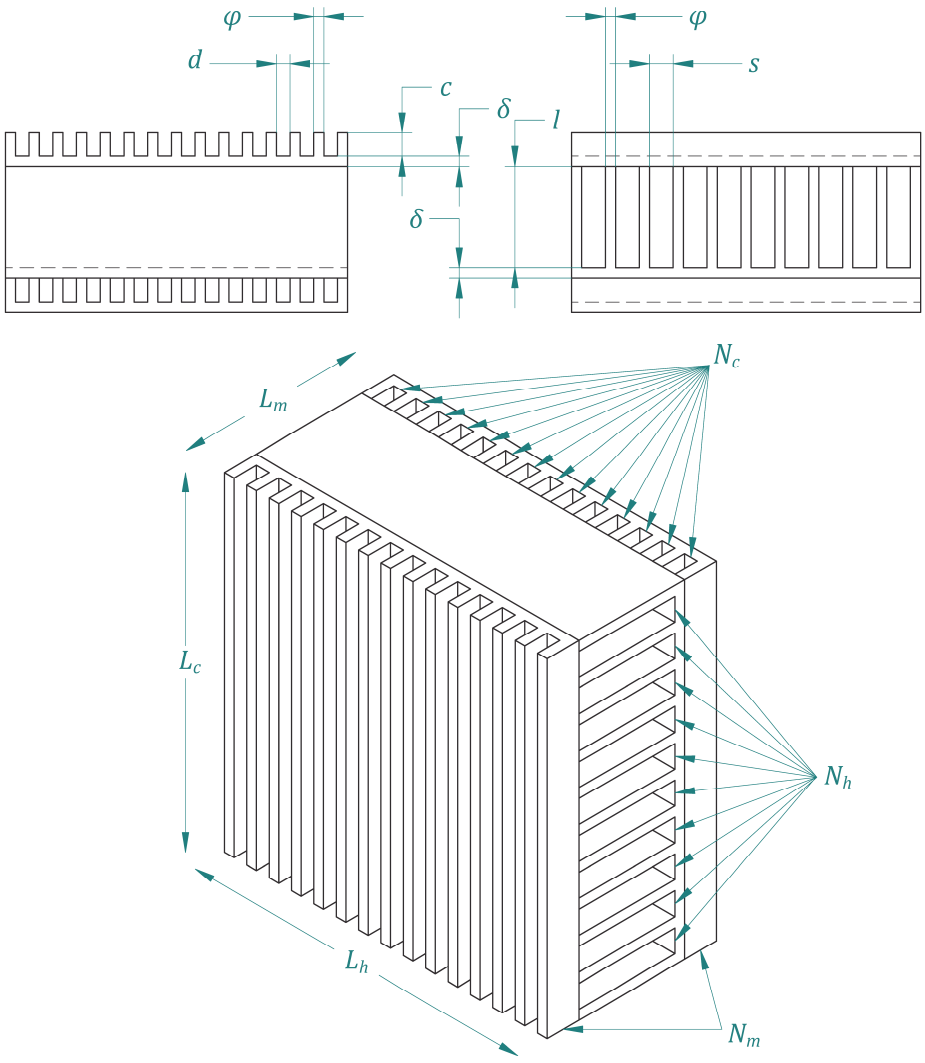

Figure 6: details of the microchannel regenerator and nomenclature of the design parameters

2.2.1 Parameterization of the Geometry

The geometric parameters of the single-pass crossflow MCHE of Figure 6 can be used to define the following quantities, needed for the thermohydraulic design:

$$L_m = (c + \delta)\, N_m + (l + \delta)\, (N_m - 1) \tag{2.7}$$

$$L_h = d\, N_c + \varphi\, (N_c + 1) \tag{2.8}$$

$$L_c = s\, N_h + \varphi\, (N_h + 1) \tag{2.9}$$

$$S_h = \; l\, s\, N_h\, (N_m - 1) \tag{2.10}$$

$$S_c = c\, d\, N_c\, N_m \tag{2.11}$$

$$V_w = \; L_c\, L_h\, \delta\, (2\, N_m - 1) + c\, \varphi\, L_c (N_c + 1)\, N_m + l\, \varphi\, L_h (N_h + 1)(N_m - 1) \tag{2.12}$$

$$V_h = \; s\, l\, L_h\, N_h\, (N_m - 1) \tag{2.13}$$

$$V_c = c\, d\, L_c\, N_c\, N_m \tag{2.14}$$

where S_h and S_c are the total flow areas of the hot- and the cold-side; V_w is the volume of the metal matrix of the MCHE core; V_h and V_c are the volumes occupied by the gas and the liquid.

The hydraulic diameters $D_{H,h,}$ and $D_{H,c,}$, the channels aspect ratios a and b, and the fin aspect ratio a_φ are calculated as follows:

$$D_{H,h} = \frac{2\, s\, l}{s + l} \tag{2.15}$$

$$D_{H,c} = \frac{2\, c\, d}{c + d} \tag{2.16}$$

$$a = \frac{l}{s} \tag{2.17}$$

$$b = \frac{c}{d} \tag{2.18}$$

$$a_{\varphi} = \frac{l}{\varphi} \tag{2.19}$$

The proposed MCHE can be classified as plate-fin heat exchanger: these devices are usually designed sizing only one plate, which consists in dividing wall and half-height fins on each side [73], as shown in Figure 7. If the stack length is sufficient to ignore edge effects due to heat losses to the ambient at the bottom and at the top of the pile, the said subdivision exploits symmetry planes, and therefore each plate is equivalent. It is therefore convenient to define geometric relations on the element of Figure 7. The whole exchanger is now seen as the sum of

$$N_p = 2(N_m - 1) \tag{2.20}$$

plates, or elements, plus half cold-side module on each extremity of the stack. These two small parts are supposed to contribute to the total flow area but not to the total heat transfer surface area, since they are expected to exchange principally with the environment.

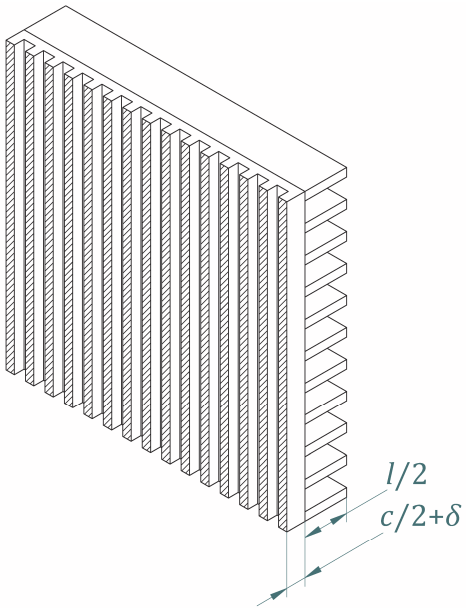

Figure 7: single element or plate of the microchannel heat exchanger, constituted by the dividing wall and half-height fins on both sides

The following quantities are then defined, basing on Figure 7:

$$A_{p,h} = s\, L_h\, N_h \tag{2.21}$$

$$A_{f,h} = l\, L_h\, N_h \quad (2.22)$$

$$A_h = A_{p,h} + A_{f,h} = (s + l)\, L_h\, N_h \quad (2.23)$$

$$A_{p,c} = d\, L_c\, N_c \quad (2.24)$$

$$A_{f,c} = c\, L_c\, N_c \quad (2.25)$$

$$A_c = A_{p,c} + A_{f,c} = (d + c)\, L_c\, N_c \quad (2.26)$$

$$S_w = L_c\, L_h \quad (2.27)$$

where A_p and A_f are the primary area and the fin area, and together form the heat transfer surface area A; S_w is the area of the dividing wall. Multiplying these areas by N_p, the total corresponding values for the whole MCHE are obtained, since, as said, the two terminal parts are neglected.

2.2.2 Channel Aspect Ratio and Compactness

From the geometric point of view, the MCHE can also be seen as the sum of single microchannels, dividing the core matrix as shown in Figure 8 for the hot-side.

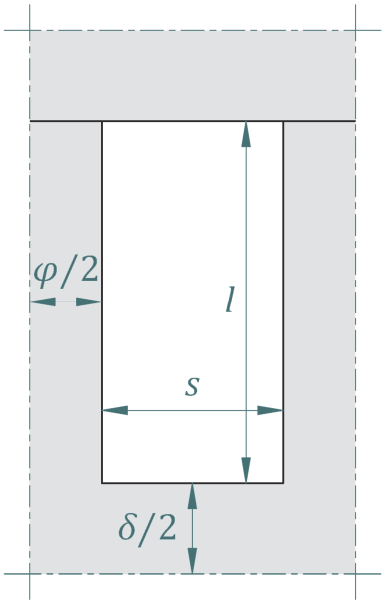

Figure 8: section of a single channel; the region occupied by the solid wall is shown in gray while the fluid is left white

Considering N_h $(N_m - 1)$ of such channels for the hot-side and N_c N_m channels for the cold-side (obtained with a similar subdivision), only a small portion of the metal matrix at the beginning and end of each module is neglected. Then, the heat transfer surface area density β, introduced in Section 1.2.1 to mathematically express the concept of compactness, can be written as:

$$\beta_h = \frac{A_h}{V_{w,h} + V_h} = \frac{2\,(s + l)\,L_h\,N_h}{(\varphi\,l + \delta\,s + \delta\,\varphi)\,L_h\,N_h + l\,s\,L_h\,N_h} = \frac{2\,(1 + a\,)\,s}{(s + \varphi)\,(a\,s + \delta)} \quad \textbf{(2.28)}$$

Clearly, as φ and δ decrease, the geometry becomes more compact. Supposing s the shortest side of the rectangular cross-section and l the longest, the channel aspect ratio defined by (2.17) reads:

$$a \geq 1 \quad \textbf{(2.29)}$$

It is interesting to investigate the behavior of β_h as the channel dimensions vary, considering wall thickness fixed to the minimal values allowed by the manufacturing method. Since it is reasonable to presume a larger thickness for the plates when compared to the fins, the following inequality is considered:

$$\varphi \leq \delta \quad \textbf{(2.30)}$$

The partial derivative of β_h with respect to s reads:

$$\frac{\partial \beta_h}{\partial s} = \frac{2\,(1 + a)(\delta\,\varphi - a\,s^2)}{(a\,s + \delta)^2\,(s + \varphi)^2} \quad \textbf{(2.31)}$$

which is equal to zero in:

$$s_\beta = \sqrt{\frac{\delta\,\varphi}{a}} \quad \textbf{(2.32)}$$

For each a, this coordinate corresponds to the maximum of β_h with respect to s, due to the mean value theorem, in fact:

$$\lim_{s \to 0} \beta_h = 0 \quad \textbf{(2.33)}$$

$$\lim_{s \to s_\beta} \beta_h = \frac{2\,(1+a)}{(\sqrt{\delta} + \sqrt{a\,\varphi})^2} > 0 \tag{2.34}$$

$$\lim_{s \to \infty} \beta_h = 0 \tag{2.35}$$

The expression reported in (2.34) represents the maximum compactness obtainable for given channel aspect ratio and wall thicknesses.

It should be mentioned that the definition (2.28) is different from the one generally considered [23], as it also takes the thickness of the dividing wall into account when calculating the volume: using the traditional definition, δ disappears from (2.28) and the maximum of β, which turn out to be monotonically decreasing, moves to $s = 0$. However, when s becomes comparable to δ, increasing β do not necessary correspond to reduced dimensions of the heat exchanger as a whole. The definition (2.28) restores the parallelism between surface area density and compactness of the device.

Taking now the partial derivative of β_h with respect to a:

$$\frac{\partial \beta_h}{\partial a} = \frac{2\,(\delta - s)\,s}{(a\,s + \delta)^2\,(s + \varphi)} \tag{2.36}$$

Therefore β_h grows or decreases monotonically with respect to a according to the sign of $\delta - s$, meaning that high aspect ratios ($a \to \infty$) are to be preferred if $s < \delta$ while low aspect ratios ($a \to 1$) are desirable if $s > \delta$. In the particular case $s = \delta$, the surface area density is independent of a. Then, for each s, the maximum of β_h with respect to a is:

$$\lim_{a \to \infty} \beta_h = \frac{2}{s + \varphi} \quad \text{if} \quad s < \delta \tag{2.37}$$

$$\lim_{a \to 1} \beta_h = \frac{4}{(s+\delta)(s+\varphi)} \quad \text{if} \quad s > \delta \tag{2.38}$$

For each value of a, as said, equation (2.32) gives the coordinate s_β corresponding to the maximum of β_h with respect to s. Therefore, considering $s = s_\beta$ in the above equation leads to:

$$\beta_{h,max} = \lim_{\substack{s \to s_\beta \\ a \to \infty}} \beta_h = \frac{2}{\varphi} \tag{2.39}$$

$$\bar{\beta}_{h,max} = \lim_{\substack{s \to s_\beta \\ a \to 1}} \beta_h = \frac{4}{(\sqrt{\delta} + \sqrt{\varphi})^2} \tag{2.40}$$

It can be easily shown that if (2.30) holds true, then $\beta_{h,max} > \bar{\beta}_{h,max}$; therefore $\beta_{h,max}$ is the absolute maximum of β_h and depends only on φ. Evidently, this level of compactness cannot be reached in practice, nevertheless it shows the importance of reducing the fin thickness φ in particular.

The following dimensionless quantities are defined:

$$s^* = \frac{s}{\varphi} \tag{2.41}$$

$$\beta_h^* = \frac{\beta_h}{\beta_{h,max}} = \frac{\varphi\, \beta_h}{2} = \frac{(1 + a)\, s^*}{(s^* + 1)\left(a\, s^* + \frac{\delta}{\varphi}\right)} \tag{2.42}$$

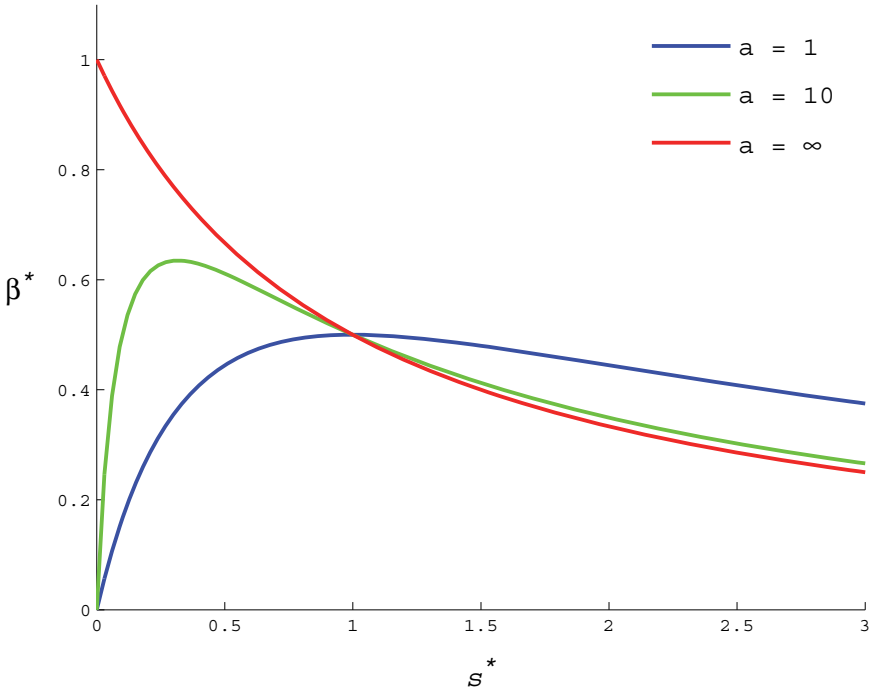

Figure 9: $\boldsymbol{\beta_h^*}$ as a function of $\boldsymbol{s^*}$ and a for the particular case $\delta = \varphi$

In the particular case $\delta = \varphi$, β_h^* becomes a function of s^* and a only, as shown in Figure 9. Notice that the surface area density is enhanced reducing the channel size until the condition expressed by (2.32) is met. Then, if the channel size is further diminished leaving the wall thickness untouched, β_h starts to decrease, as anticipated in Section 1.2.1.

While imposing (2.32) ensures high compactness, it is not the best choice for a light MCHE. In order to prove this statement and to mathematically express the concept of lightness in the same way as β represents compactness, the parameter α is defined as the ratio of the total transfer area to the total exchanger mass. For the hot-side of the geometry of Figure 8, the parameter α_h can be written as:

$$\alpha_h = \frac{A_h}{\rho_w V_{w,h} + \rho_h V_h} = \frac{2\,(s+l)\,L_h}{\rho_w\,(l\,\varphi + s\,\delta + \delta\,\varphi)L_h + \rho_h\,l\,s\,L_h} = \frac{2\,(1+a\,)s}{\rho_w\,(\varphi\,a\,s + \delta s + \delta\,\varphi) + \rho_h\,a\,s^2} \tag{2.43}$$

This function behaves qualitatively as (2.28). For each a and fixed wall thicknesses and densities, the coordinate corresponding to the maximum of $\alpha_h$with respect to s can be found with the same procedure followed to obtain (2.32), giving:

$$s_\alpha = \sqrt{\frac{\rho_w\,\delta\,\varphi}{\rho_h\,a}} > \sqrt{\frac{\delta\,\varphi}{a}} = s_\beta \tag{2.44}$$

In Figure 10, $\alpha^+ = \alpha/\alpha(s_\alpha)$ and $\beta^+ = \beta/\beta(s_\beta)$ are plotted as functions of s^* for the hot- and the cold-side, in the particular case of $a = 10$ and $\delta = \varphi$. The copper alloy is considered for the solid wall and the working fluid is D4. Due to the low density of the gas, the maximum for α_h occurs at high values of s^* and is left out of the figure to emphasize the other two maxima.

Anyhow, whichever side is considered, for $s > s_\alpha$ and $s < s_\beta$ both α and β decrease; therefore it is convenient to choose the smallest side of the rectangular microchannel such as:

$$s_\alpha \geq s \geq s_\beta \tag{2.45}$$

In this interval, higher aspect ratios guarantee higher α_h ; on the other hand, , according to (2.36), the value of $\delta - s$ has to be considered to determine the behavior of β_h . In fact, even if it is necessarily $\delta \geq s_\beta$ (from (2.32), considering (2.29) and (2.30)), s_α can be both greater or less than δ, depending on the ratio of the wall density to the fluid density (from (2.44)). Therefore, in general, the choice of high aspect ratios enhances the compactness of the device if $\delta \geq s \geq s_\beta$ and penalizes it if $s_\alpha \geq s \geq \delta$.

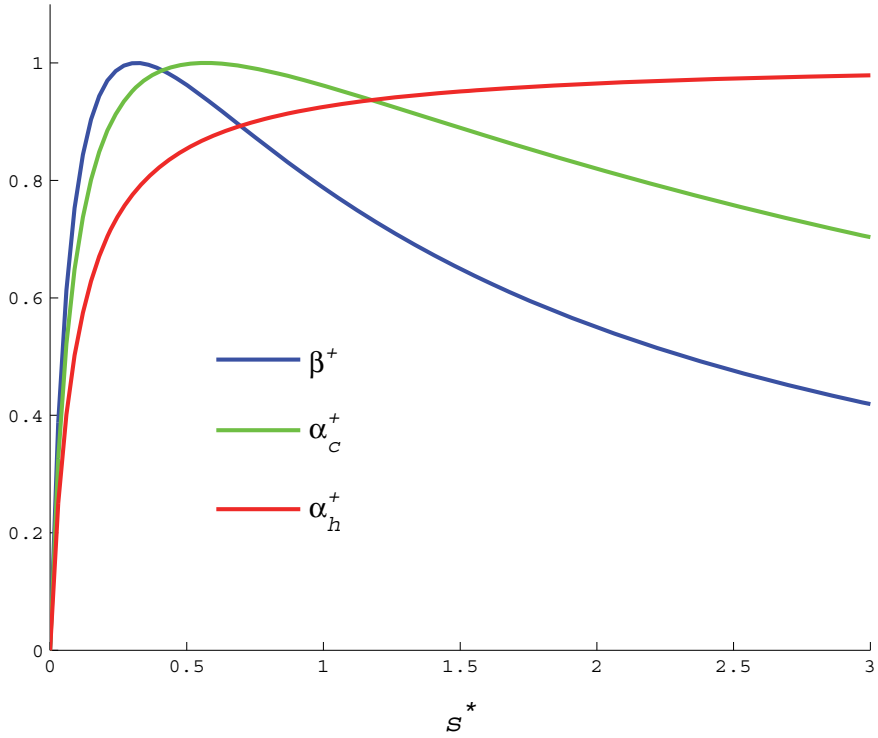

Figure 10: normalized $\boldsymbol{\alpha}$ and $\boldsymbol{\beta}$ for $\boldsymbol{a = 10}$ and $\boldsymbol{\delta = \varphi}$

Since the objective function to minimize is the total weight of the MCHE, high aspect ratios are expected in the optimal device. The equations of the present section are obtained starting from the assumption $s < l$. In the opposite case $s > l$, symmetrical results are obtained, with equal or lower β_h and α_h because of (2.30). For example, the absolute maxima now become respectively $2/\delta \leq 2/\varphi$ and $2/(\rho_w\,\delta) \leq 2/(\rho_w\,\varphi)$. High aspect ratio microchannels characterized by $s < l$ are then to be preferred. This choice also improves the structural strength of the MCHE because of a larger number of contact points between the modules. Moreover, fewer modules (and bonds) are needed when compared to the case $s > l$, but longer fins are required between the channels.

It should be noted that increasing the fin length l penalizes the fin efficiency $\eta_{f,h}$, in fact from its definition:

$$\lim_{l\to\infty} \eta_{f,h} = \lim_{l\to\infty} \frac{\tanh\left(\sqrt{\frac{2\,h_h}{k_w\,\varphi}}\,\frac{l}{2}\right)}{\sqrt{\frac{2\,h_h}{k_w\,\varphi}}\,\frac{l}{2}} = 0 \tag{2.46}$$

However, the high thermal conductivity of the material limits the negative impact of longer fins. Moreover, in the small scale the difference between primary and extended surfaces weakens, as the fin efficiency $\eta_{f,h}$ tend to 1:

$$\lim_{\varphi\to 0} \eta_{f,h} = \lim_{\varphi\to 0} \frac{\tanh\left(\sqrt{\frac{2\,h_h}{k_w\,\varphi}}\,\frac{l}{2}\right)}{\sqrt{\frac{2\,h_h}{k_w\,\varphi}}\,\frac{l}{2}} \geq \lim_{\varphi\to 0} \frac{\tanh\left(\sqrt{\frac{2\,h_h}{k_w}}\,\frac{a_{\varphi,max}}{2}\sqrt{\varphi}\right)}{\sqrt{\frac{2\,h_h}{k_w}}\,\frac{a_{\varphi,max}}{2}\sqrt{\varphi}} = 1 \tag{2.47}$$

The manufacturing method sets the maximum aspect ratio of the microchannels a_{max} and/or the of the fins $a_{\varphi,max}$; considering the procedures described in Section 1.2.3, a reasonable maximum channel aspect ratio is set to:

$$a_{max} = a_{\varphi,max} = 10 \tag{2.48}$$

A criterion to select a suitable minimum channel aspect ratio will be developed in Section 2.4.2; until then, from (2.29) it can be considered $a_{min} = 1$. Then, the constraint expressed by (2.45) can be relaxed to:

$$\sqrt{\frac{\rho_w\,\delta\,\varphi}{\rho_h\,a_{min}}} > s > \sqrt{\frac{\delta\,\varphi}{a_{max}}} \tag{2.49}$$

Using the definition of a (2.17), equation (2.45) can also be written as:

$$\frac{\rho_w\,\delta\,\varphi}{\rho_h\,s} > l > \frac{\delta\,\varphi}{s} \tag{2.50}$$

Finally, the following conditions are obtained:

$$s < \frac{\varphi\,a_{\varphi,max}}{a_{min}} \tag{2.51}$$

$$l < \varphi \, a_{\varphi,max} \tag{2.52}$$

$$s \, a_{min} < l < s \, a_{max} \tag{2.53}$$

It is worth to underline that the analysis carried on in this section is based on purely geometric relationships. The shape of the channel affects heat transfer, pressure drop and scaling effects, so that the most attractive configuration from a geometric point of view might actually be less desirable than others. This is why, instead of imposing (2.32) or (2.44), the optimal values for channel dimensions are sought after in the selected intervals, obtained above for the hot-side and reported below for the cold-side:

$$\sqrt{\frac{\rho_w \, \delta \, \varphi}{\rho_c \, a_{min}}} > d > \sqrt{\frac{\delta \, \varphi}{a_{max}}} \tag{2.54}$$

$$\frac{\rho_w \, \delta \, \varphi}{\rho_c \, d} > c > \frac{\delta \, \varphi}{d} \tag{2.55}$$

$$d < \frac{\varphi \, a_{\varphi,max}}{a_{min}} \tag{2.56}$$

$$c < \varphi \, a_{\varphi,max} \tag{2.57}$$

$$d \, a_{min} < c < d \, a_{max} \tag{2.58}$$

From the literature reviewed, the following minimal value of the wall thickness is within reach and is hence adopted to minimize both (2.28) and (2.43) :

$$\varphi = \delta = \varphi_{min} = \delta_{min} = 0.0003 \text{ [m]} \tag{2.59}$$

2.3 Additional Elements

In addition to the core, i.e. the metal matrix described in the above sections, every heat exchanger is constituted by other components, which distribute the working fluid or guarantee the integrity of the assembly. These components impose constraints on the optimal solution and contribute to the total weight, which is the objective function to

minimize. The headers, in particular, deserve special attention since their impact on both the pressure drop and the weight of the device is of the same order of magnitude as the contribution of the core.

2.3.1 Frame

To improve the structural strength of the exchanger, the employ of two plates of thickness $\tau/2 \gg \varphi$ at the top and at the bottom of the stack could prove useful. Moreover, as shown in Figure 11, on each module the thickness of the first and the last fins is increased of the same quantity $\tau/2$. A frame is then formed, on which the headers can be brazed. In addition, the frame offers a relatively large surface suitable for eutectic bonding, or alternatively it makes room for bolts in the four corners, as can be seen in Figure 11. To prevent leakage, gaskets as in Figure 12 could be formed directly on the modules in the molding process

The presence of the frame is neglected for what concern heat transfer but is taken into account regarding the core volume; equation (2.12) now becomes:

$$\begin{aligned} V_w = {} & L_c\, L_h\, \delta\, (2\, N_m - 1) + c\, \varphi\, L_c (N_c + 1)\, N_m + l\, \varphi\, L_h (N_h + 1)(N_m - 1) \\ & + (L_c + \tau)(L_h + \tau)\, \tau + (L_c + \tau)\, \tau\, (c + \delta)\, N_m \\ & + (L_h + \tau)\, \tau\, (l + \delta)\, (N_m - 1) + (N_c + 1) \tau\, \varphi\, c\, N_m \\ & + (N_h + 1)\, \tau\, \varphi\, l\, (N_m - 1) + \tau\, L_c\, \delta\, N_m + \tau\, L_h\, \delta\, (N_m - 1) \end{aligned} \tag{2.60}$$

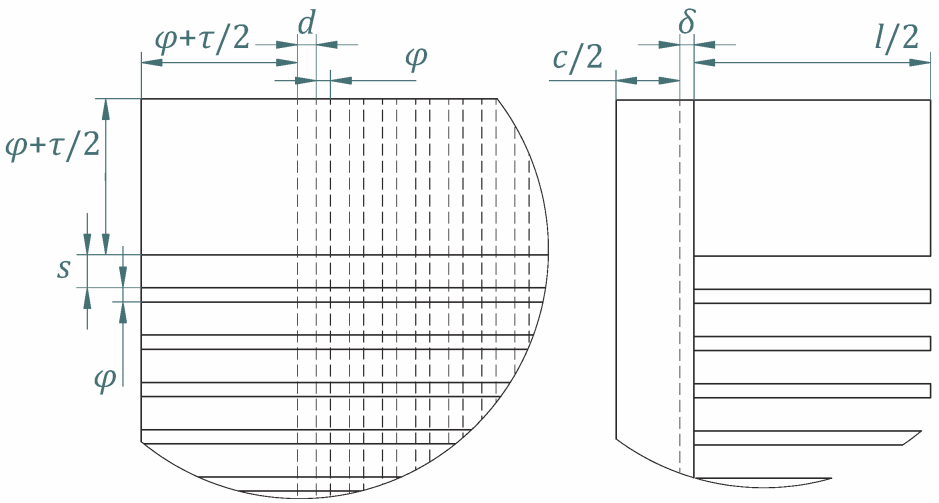

Figure 11: corner detail of the MCHE with focus on the frame

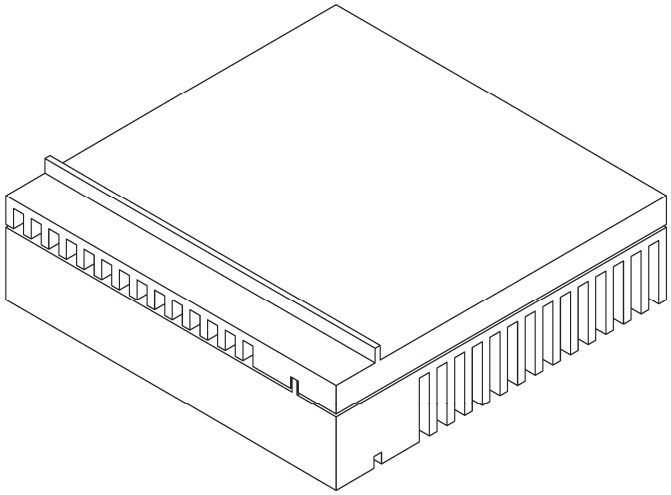

Figure 12: gaskets to be formed directly on the plates

Quantitatively, τ should be as small as possible, then it is arbitrarily chosen:

$$\tau = \tau_{min} = 0.01 \text{ [m]} \tag{2.61}$$

2.3.2 Piping

The supply and return pipes are to be connected to the distribution elements, which will be addressed in the next section. In general, the free flow area of the pipes is smaller than the flow area of the headers and properly sized diverging and converging connections may be excessively big if the area difference is large. The simplest (and smallest) connections, usually called abrupt entrance and exit (with reference to the smaller passage), are therefore chosen. These connections are widely employed in plate-fin exchangers [74]; however, the pressure difference across these elements may be large.

The pressure loss due to the abrupt entrance and exit is expressed as follows:

$$\Delta p_{abrupt} = \left[\frac{0.7 - 0.2\,\frac{S_{pipe}}{S_{head}} - 0.5\left(\frac{S_{pipe}}{S_{head}}\right)^2}{\rho_{out}} - \frac{\frac{S_{pipe}}{S_{head}} - \left(\frac{S_{pipe}}{S_{head}}\right)^2}{\rho_{in}} \right] \left(\frac{\dot{m}}{S_{pipe}}\right)^2 \tag{2.62}$$

where S_{pipe} and S_{head} are the flow area of the piping and at the inlet of the headers;

this expression is obtained considering the equations given in Section 2.4.2 if, on each side, S_{pipe} is unique for the supply and return pipe and if S_{head} is the same for the inlet and outlet headers. Equation (2.62) clearly shows that, for given operating conditions, it is necessary to increase S_{pipe} and/or to decrease S_{head} in order to reduce the hydraulic losses at the inlet and at the outlet of the headers.

Because of the high density, on the cold-side of the studied MCHE, steel pipes DN 40 [75] are sufficiently big to guarantee losses lower than 1 % of the allowable pressure drop of equation (2.2), regardless of the free flow area of the headers; therefore it is assumed the following diameter D_c for the cold-side piping:

$$D_c = 40.90 \text{ [mm]} \tag{2.63}$$

On the other hand, the hot side inlet header faces directly the turbine designed in [6]; the diameter of the hot-side piping D_h is therefore considered equal to the turbine outlet diameter:

$$D_h = 85 \text{ [mm]} \tag{2.64}$$

Since this diameter then cannot be increased and the pressure losses are comparable to the core pressure drop, the area change across the entrance and the exit of the headers should be kept small. The header flow area is then to be limited, because S_{pipe} is imposed by (2.64). However, as it will be discussed in the next section, if S_{head} is too small, the pressure drop along the header would be excessive. Therefore, an optimal value for S_{head} exists, which minimizes the total pressure drop in the header.

It is mentioned for completeness that, for the diameters of (2.63) and (2.64), standard thicknesses [75] are more than sufficient, according to ASME guidelines for pipes under internal [76] and external [77] pressure. Moreover, the rules of thumb for the maximum velocity of liquid and vapor lines of refrigerant suggested in Perry's Chemical Engineers' Handbook [78] are well satisfied. For simplicity, it is assumed a unique thickness $\tau/2$ as defined by (2.61), which is close to the standard values.

2.3.3 Headers

In compact gas-to-liquid exchanger, the gas-side header design is more difficult because of the large frontal area needed to reduce the pressure drop. In such cases, either no header is used, as in an automobile radiator (on the air side), or an oblique flow header is generally employed [23]. Since the heat recovery system for which the MCHE is designed is based on a closed cycle, distribution elements are needed also on the gas-side.

The headers should be designed to achieve uniform distribution of the fluid flow within the heat exchanger core, and minimal pressure drop within the header itself, since no heat transfer is generally associated with the pressure drop expenditure [23]. The first requirement is fulfilled determining the appropriate shape of the headers in order to produce a matching pressure profile in the inlet and outlet headers: the two-dimensional theory for oblique-flow headers presented in [79] is therefore considered. The second requirement is satisfied determining the optimal value for S_{head} such as the total pressure drop ascribable to the distribution elements is minimized; the discussion follows from the precedent section and will be continued once the header shape is determined.

In an oblique-flow header, the fluid inlet flow direction is not perpendicular to the core face (as in a normal-flow header). A particular subgroup of oblique-flow headers has the inlet flow direction parallel to the core face area. The main quality of this class of distribution elements is the minimization of header volume and flow separation [23]. The model considers headers with uniform inlet velocity and rectangular cross-section; however it will be here used for semielliptical cross-sections, which are a better match to the round piping and help to reduce weight and space occupied for given header height, width and depth.

Depending on whether the supply and the return pipes of the heat exchanger are on the same side of the device or not, the oblique-flow headers assume a counterflow or parallelflow configuration. In both arrangements, the optimal outlet header (to minimize the pressure drop in the distribution elements and the flow maldistribution in the core) is

a box header, i.e. with constant cross-section. The best inlet header for the counterflow arrangement is a box header too, which acts as a diffuser, increasing the pressure of the flow as the mass flow rate diminishes along the axial direction of the header (because part of the fluid goes into the core of the exchanger). This counterbalances the different length of the paths followed by the various streamlines inside the whole device. On the other hand, in the parallelflow arrangement, since there is no difference in the path of the streamlines, the optimal cross-section of the inlet header reduces along the axial direction.

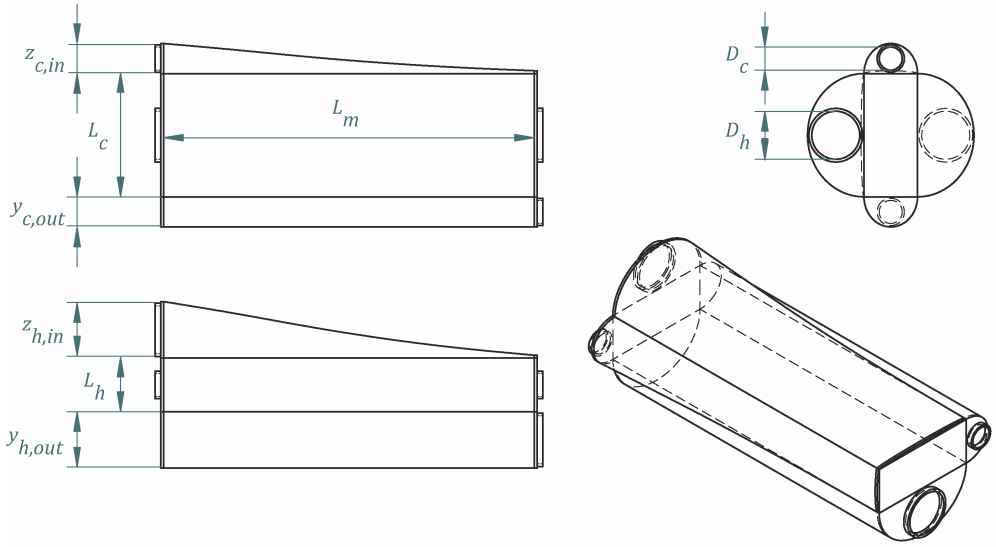

Figure 13: parallelflow headers for the microchannel heat exchanger

Parallelflow headers have higher pressure drop than counterflow headers. Moreover, the inlet header is more difficult to manufacture due to the reducing cross-section. On the other hand, parallelflow headers are smaller and lighter, since the outlet header can be reduced arbitrarily, varying at the same time the shape of the inlet header for the matching pressure profile needed to assure uniform flow distribution in the core. Contrarily, the dimensions of the inlet an outlet counterflow headers are not independent: for what concern the case study, the required size is too big to consider. Parallel flow headers are then chosen and dimensioned.

The information on the piping system is here used to size the headers; the equations reported below refer to the hot-side. However the correspondent equations for the cold

side are obtained simply inverting the subscripts $_h$ and $_c$. Considering the diameter of equation (2.64) and the parameters of Figure 13, it must be:

$$z_{h,in} > D_h + \tau \tag{2.65}$$

$$y_h = y_{h,out} > D_h + \tau \tag{2.66}$$

Moreover, because of the shape of the headers, it is reasonable to impose:

$$z_{h,in} < L_c \tag{2.67}$$

$$y_{h,out} < L_c \tag{2.68}$$

Defining now the following parameter:

$$H = \frac{\pi}{2} \frac{z_{h,in}}{y_{h,out}} \sqrt{\frac{\rho_{h,in}}{\rho_{h,out}}} \tag{2.69}$$

the optimal profile of the inlet headers assume the form:

$$z_h = \frac{\left(1 - \frac{x_h}{L_m}\right) z_{h,in}}{\sqrt{1 + \left(H \frac{x_h}{L_m}\right)^2}} \tag{2.70}$$

which is function of the axial coordinate of the header x_h, as shown in Figure 14.

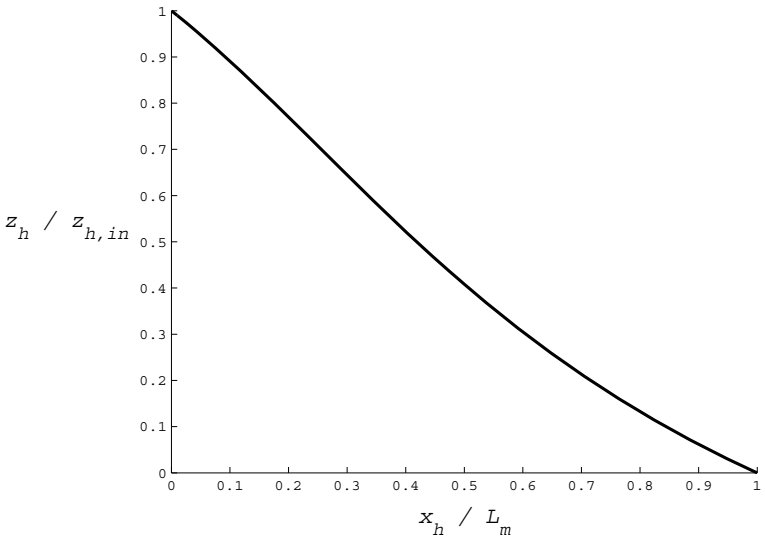

Figure 14: non-dimensional profile of the hot-side inlet header

The volume of the solid material constituting the inlet header needs some approximations in order to be calculated; the perimeter P_{head} , function of the axial coordinate of the header, is the semicircumference of an ellipsis, which is slightly overestimated by the following correlation:

$$P_{head} = \pi \sqrt{\frac{\left(\frac{L_c}{2}\right)^2 + z_h^2}{2}} \tag{2.71}$$

while the cross sectional area of the header walls, supposed of thickness $\tau/2$, is a semielliptical crown and is approximated as:

$$S_{head,w} = \frac{\tau}{2} P_{head} \tag{2.72}$$

The above equation requires the following conditions to be satisfied for all x_h:

$$\frac{\tau}{2} \cong \frac{\tau}{2} \frac{1}{\cos \arctan \frac{\mathrm{d}z_h}{\mathrm{d}x_h}} = \frac{\tau}{2} \sqrt{1 + \left(\frac{\mathrm{d}z_h}{\mathrm{d}x_h}\right)^2} \implies \frac{\mathrm{d}z_h}{\mathrm{d}x_h} \ll 1 \tag{2.73}$$

$$\pi \sqrt{\frac{\left(\frac{L_c}{2}\right)^2 + z_h^2}{2}} \cong \pi \sqrt{\frac{\left(\frac{L_c + \tau}{2}\right)^2 + \left(z_h + \frac{\tau}{2}\right)^2}{2}} \implies \begin{cases} \tau \ll z_h \\ \tau \ll L_c \end{cases} \tag{2.74}$$

Then, considering also the walls closing the header frontally, the volume $V_{head,h,in}$ of metal composing the hot-side inlet header is written as:

$$V_{head,h,in} = \frac{\pi}{8} \tau (L_c + \tau)\left(z_{h,in} + \tau\right) + \int_0^{L_m} S_{head,w} \, \mathrm{d}x_h \tag{2.75}$$

$$\begin{aligned} \int_0^{L_m} S_{head,w} \, \mathrm{d}x_h &= \frac{\pi \, \tau}{4\sqrt{2}} \int_0^{L_m} \sqrt{L_c^2 + 4 \, \frac{\left(1 - \frac{x_h}{L_m}\right)^2 z_{h,in}^2}{1 + \left(H \, \frac{x_h}{L_m}\right)^2}} \, \mathrm{d}x_h \\ &= L_m \, \frac{\pi \, \tau}{4\sqrt{2}} \int_0^1 \sqrt{L_c^2 + 4 \, \frac{(1 - X)^2 z_{h,in}^2}{1 + (H \, X)^2}} \, \mathrm{d}X \end{aligned} \tag{2.76}$$

The integral now can be solved numerically, independently of N_m:

$$\int_0^1 \sqrt{L_c^2 + 4\,\frac{(1-X)^2 z_{h,in}^2}{1+(H\,X)^2}}\;\mathrm{d}X \cong \frac{1}{2\,n}\left[\sqrt{L_c^2 + 4\,z_{h,in}^2} + L_c + 2\sum_{i=1}^{n-1}\sqrt{L_c^2 + 4\,\frac{\left(1-\frac{i}{n}\right)^2 z_{h,in}^2}{1+\left(H\,\frac{i}{n}\right)^2}}\right] \tag{2.77}$$

If the Natural number n is sufficiently high, the integrating function is well approximated by a polygonal.

The volume $V_{fluid,h,in}$ of fluid contained in the inlet header is obtained with a similar procedure, with a better approximation; the semielliptical cross-section of the header is analytically expressed as:

$$S_{head,h} = \frac{\pi}{4}\,L_c\,z_h \tag{2.78}$$

Then, the fluid volume is calculated as:

$$V_{fluid,h,in} = \int_0^{L_m} S_{head,h}\,\mathrm{d}x_h = L_m\,\frac{\pi\,L_c}{4}\int_0^1 \frac{(1-X)z_{h,in}}{\sqrt{1+(H\,X)^2}}\,dX \tag{2.79}$$

$$\int_0^1 \frac{(1-X)z_{h,in}}{\sqrt{1+(H\,X)^2}}\,dX \cong \frac{1}{2\,n}\left[z_{h,in} + 2\sum_{i=1}^{n-1}\frac{\left(1-\frac{i}{n}\right)z_{h,in}}{\sqrt{1+\left(H\,\frac{i}{n}\right)^2}}\right] \tag{2.80}$$

The volumes of metal and fluid in the outlet header are straightforward to calculate, since the geometries are based on cylinders with semielliptical cross-section:

$$V_{head,h,out} = \frac{\pi}{8}(L_m+\tau)(L_c+\tau)(2\,y_h+\tau) - \frac{\pi}{4}L_m\,L_c\,y_h \tag{2.81}$$

$$V_{fluid,h,out} = \frac{\pi}{4}L_m\,L_c\,y_h \tag{2.82}$$

Notice that the model here adopted for the headers is recommended only if [79]:

$$\frac{z_{h,in}}{L_m} > \frac{1}{3} \tag{2.83}$$

$$\frac{\Delta p_{core,h}}{\frac{1}{2}\rho_{h,in}\, v_{h,in}^2} > \frac{1}{2} \tag{2.84}$$

where $\Delta p_{core,h}$ is the total pressure losses ascribable to the hot-side of the heat exchanger core; $v_{h,in}$ is the mean axial fluid velocity at the entrance of the hot-side inlet header, which is calculated as:

$$v_{h,in} = \frac{\dot{m}}{\rho_{h,in}\, S_{head,h,in}} = \frac{\dot{m}}{\rho_{h,in}\, \frac{\pi\, L_c\, z_{h,in}}{4}} \tag{2.85}$$

The pressure drop in the distribution elements is then evaluated as follows:

$$\Delta p_{head,h} = \left[\left(1 - \frac{4}{\pi^2}\right) H^2 + 1\right] \frac{\rho_{h,in}\; v_{h,in}^2}{2} \tag{2.86}$$

This quantity contributes to the total pressure drop of the MCHE and accounts for both the inlet and the outlet header.

Since parallelflow headers are employed, the designer is free to choose arbitrary values for $z_{h,in}$ and $y_{h,out}$. It can then be imposed:

$$z_{h,in} = y_{h,out} \tag{2.87}$$

$$H = \frac{\pi}{2} \sqrt{\frac{\rho_{h,in}}{\rho_{h,out}}} \tag{2.88}$$

Therefore, equation (2.86) becomes a function of the sole $S_{head,h,in}$; the sum of equation (2.62) and (2.86) can then be minimized with respect to $S_{head} \equiv S_{head,h,in}$ in order to find the optimal value S_{opt} for the inlet flow area of the headers; the various contributions and the total pressure drop in the distribution elements of one side of the crossflow MCHE are plotted in Figure 15.

For the given operating conditions, the optimal value is:

$$S_{opt} = \frac{\pi \left(L_c \, z_{h,in}\right)_{opt}}{4} = 0.0164989 \ [\mathrm{m}^2] \tag{2.89}$$

which gives the minimal header pressure drop:

$$\Delta p_{head,h} + \Delta p_{abrupt,h} = 1261 \ [\mathrm{Pa}] \tag{2.90}$$

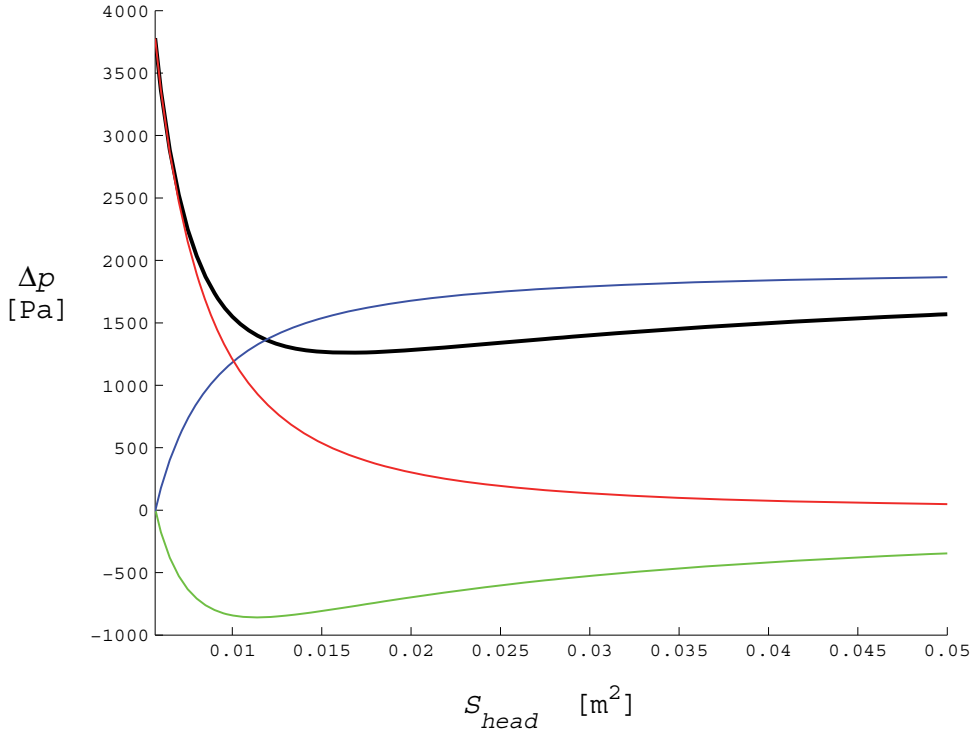

Figure 15: pressure drop in the hot-side headers as a function of the inlet cross-sectional area of the headers; the **red** line is the pressure drop in the inlet and outlet headers, according to (2.86); the **blue** and the **green** lines corresponds to the two terms summed in(2.62) and represents the pressure drop and rise (negative values) due to the abrupt area change across the connections between the headers and the piping; the **black** line is the sum of the various contributions it represents the total pressure drop in the hot-side headers to be minimized; the origin of the axis is set in (S_{pipe} , -1000)

From equation (2.2), the allowable pressure drop for the microchannel core then becomes:

$$\Delta p_{max} = 3226 - 1261 = \ 1965 \ [\mathrm{Pa}] \tag{2.91}$$

Moreover, from equation (2.65) (2.67) and (2.89):

$$\frac{4\,S_{opt}}{\pi\left(z_{h,in}\right)_{max}} = \frac{4\,S_{opt}}{\pi\,L_c} < L_c < \frac{4\,S_{opt}}{\pi\,(D_h+\tau)} = \frac{4\,S_{opt}}{\pi\left(z_{h,in}\right)_{min}} \tag{2.92}$$

Substituting (2.9) into the above equations it gives:

$$\frac{2\sqrt{\frac{S_{opt}}{\pi}} - \varphi}{s+\varphi} < N_h < \frac{\frac{4\,S_{opt}}{\pi\,(D_h+\tau)} - \varphi}{s+\varphi} \tag{2.93}$$

Once N_h is assigned, $z_{h,in}$ can be calculated with (2.9) and (2.89). However, the greater L_c the larger are the hot-side modules; this helps to contain the number of modules and the length of the stack. Since the header cross section is imposed by (2.89), a shorter MCHE has lighter headers, and is therefore a better candidate for the optimal design. Hence, the constraint (2.93) can be substituted with:

$$N_h = \frac{\frac{4\,S_{opt}}{\pi\,(D_h+2\,\tau)} - \varphi}{s+\varphi} \tag{2.94}$$

$$z_{h,in} = y_{h,out} = D_h + \tau \tag{2.95}$$

This is confirmed by the final result of the optimization process, which does not vary considering (2.93) instead of (2.97).

As said, such a limiting constraint is not necessary for the cold-side; then, bearing in mind equation (2.8), it can be imposed what follows:

$$z_{c,in} = y_{c,out} = D_c + \tau \tag{2.96}$$

$$D_c + \tau < L_h < L_{max} - \tau \tag{2.97}$$

$$\frac{D_c+\tau-\varphi}{d+\varphi} < N_c < \frac{L_{max}-\tau-\varphi}{d+\varphi} \tag{2.98}$$

To quantify the maximum channel length L_{max}, a typical dimension of the suitable workpiece for the fabrication processes of Section 1.2.3 is considered:

$$L_{max} = 0.3\ [\mathrm{m}] \tag{2.99}$$

2.4 Mathematical Model

The optimal design is sought considering a number of properly selected intervals equal to the degrees of freedom of the system. The intervals, which constitute the design space, are discretized into arrays of values to be tested in the optimization process. For each combination of the elements from these arrays, a MCHE design that satisfy thermal requirement of Table 1 is found. Each design is then evaluated in terms of weight and pressure drop and, if the result respects the constraints, the solution is refined including longitudinal heat conduction in the model. Among the refined designs, the optimal solution can be chosen basing on the total weight of the exchanger as objective functions to minimize.

The degrees of freedom of the system correspond to the independent design parameters of Figure 6. The parameters are limited by the constraints found in the previous sections, which define the abovementioned intervals. The number of independent parameters is reduced by only one equation, derived from the well-known ε-NTU method, extensively described in several book on heat exchanger design [23] and [80]. This equation links the design parameters of Figure 6 through the thermal requirements of Table 1, and it is used to obtain the first attempt solution to be refined.

2.4.1 Thermal Design

The studied MCHE is a single-pass crossflow heat exchanger composed by a large number of uninterrupted channels with small cross-section, therefore both fluid are considered unmixed. The model generally employed to characterize such a device is derived for example in [23]. It comprises the following system of partial differential equations of the first order, obtained through a power balance on a differential element of the exchanger:

$$\frac{\partial T_h}{\partial x} = \frac{C_{min}}{C_h}\frac{NTU}{L_h}(T_h - T_c) \tag{2.100}$$

$$\frac{\partial T_c}{\partial y} = \frac{C_{min}}{C_c}\frac{NTU}{L_c}(T_h - T_c) \tag{2.101}$$

The assumptions of uniform distribution of the heat transfer area and uniform temperature on the channel cross section is invoked, as well as the hypotheses listed at the beginning of Section 1.2.2.

If the inlet temperatures are imposed as boundary conditions, the equation system can be analytically solved. Once the temperature field has been determined, analytical expressions of the terminal temperatures are obtained and substituted into the definition of exchanger effectiveness, reported in (2.6). Many equivalent forms of the effectiveness based on the exact solution of (2.100) and (2.101) are available in the relevant literature [81], among which the following is one of the simplest:

$$\varepsilon = 1 - \exp(-NTU) - \exp[-(1+r)NTU] \sum_{n=1}^{\infty} \frac{r^n}{(n+1)!} \sum_{j=1}^{n} \frac{n+1-j}{j!} NTU^{n+j} \qquad \textbf{(2.102)}$$

Due to the complexity of the analytical solution, approximated formulas are usually employed [82]; the following is cited in many textbook such as [21] [23]:

$$\varepsilon = 1 - \exp\left\{ \frac{NTU^{0.22}}{r} \left[\exp(-r \cdot NTU^{0.78}) - 1\right] \right\} \qquad \textbf{(2.103)}$$

Recently, a more accurate correlation has been proposed [83]:

$$\varepsilon = [1 + 0.44\,(1-r)] \left\{ 1 - \left[\frac{1}{0.92 + (\pi\, r^{0.15}\, NTU)^{1.25}} \right]^{0.4} \right\} \qquad \textbf{(2.104)}$$

Equation (2.104) gives a relative error with respect to (2.102) below 2 % for $0 \leq r \leq 1$ and $0 \leq NTU \leq 6$, while it can reach 3.8 % if (2.103) is employed in the same range; moreover, equation (2.104) has the benefit of being invertible:

$$NTU = \frac{1}{\pi\, r^{0.15}} \left\{ \left[\frac{1 + 0.44(1-r)}{1 - \varepsilon + 0.44(1-r)} \right]^{2.5} - 0.92 \right\}^{0.8} \qquad \textbf{(2.105)}$$

Substituting into (2.105) the required values for *r* and *ε* reported in (2.5) and (2.6):

$$NTU = 4.5794 \qquad \textbf{(2.106)}$$

From the definition of number of transfer unit *NTU*, replacing $\dot{m}$ and $c_{p,h}$ with the corresponding values in Table 1 and Table 2:

$$UA = C_{min}\, NTU = c_{P,h}\, \dot{m}\, NTU = 1829.6 \text{ [W/K]} \tag{2.107}$$

Considering the geometry of Figure 6, the definition of *UA* gives:

$$UA = \frac{1}{R_h + R_w + R_c} = \frac{1}{\frac{1}{N_p\, \eta_{o,h}\, h_h\, A_h} + \frac{\delta}{N_p\, S_w\, k_w} + \frac{1}{N_p\, \eta_{o,c}\, h_c\, A_c}} \tag{2.108}$$

where R_h and R_c are the convective resistances, and R_w is the wall thermal resistance; $\eta_{o,h}$ and $\eta_{o,c}$ are the extended surface efficiencies:

$$\eta_{o,h} = 1 - \frac{N_p\, A_{f,h}}{N_p\, A_h}\left(1 - \eta_{f,h}\right) = 1 - \frac{A_{f,h}}{A_h}\left(1 - \eta_{f,h}\right) \tag{2.109}$$

$$\eta_{o,c} = 1 - \frac{A_{f,c}}{A_c}\left(1 - \eta_{f,c}\right) \tag{2.110}$$

Thanks to the symmetry planes used to cut the geometry of Figure 7, the fin efficiencies $\eta_{f,h}$ and $\eta_{f,c}$ can be expressed as follows, as in the majority of two-fluid plate-fin exchangers [23]:

$$\eta_{f,h} = \frac{\tanh\left(m_h\, \frac{l}{2}\right)}{m_h\, \frac{l}{2}} \tag{2.111}$$

$$\eta_{f,c} = \frac{\tanh\left(m_c\, \frac{c}{2}\right)}{m_c\, \frac{c}{2}} \tag{2.112}$$

which correspond to the efficiency of half-height fin with adiabatic tip; the fin parameters m_h and m_c are written as:

$$m_h = \sqrt{\frac{2\, h_h}{k_w\, \varphi}} \tag{2.113}$$

$$m_c = \sqrt{\frac{2\, h_c}{k_w\, \varphi}} \tag{2.114}$$

As already mentioned, the assumptions listed in Section 1.2.2 are supposed true for the

optimization process and the heat transfer coefficients h_h and h_c are then considered constant on each side of the exchanger. The scaling effects are evaluated as following task in order to assess the validity of the hypotheses. The constant value for the heat transfer coefficient of fully-developed laminar flows in rectangular channels can be analytically determined. It depends only on the aspect ratio and the thermal boundary conditions. In the macroscale, crossflow heat exchangers characterized by high thermal conductivity, such as in the case of copper or aluminium alloys, are usually treated considering uniform wall temperature, both axially and peripherally [84]. The so-called T boundary condition is then here considered also for the microchannel device. In this case, the following equations, obtained with a point-matching method, give the Nusselt number as a function of the aspect ratio with an error within ±0.1 % with respect to the analytical values [84]:

$$Nu_h = 7.541\,(1 - 2.610\,a^{-1} + 4.970\,a^{-2} - 5.119\,a^{-3} + 2.702\,a^{-4} - 0.548\,a^{-5}) \quad \textbf{(2.115)}$$

$$Nu_c = 7.541\,(1 - 2.610\,b^{-1} + 4.970\,b^{-2} - 5.119\,b^{-3} + 2.702\,b^{-4} - 0.548\,b^{-5}) \quad \textbf{(2.116)}$$

Substituting (2.115) and (2.116) into the definition of *Nu* (1.8), the heat transfer coefficients are obtained. It should be noted that the effect of the real boundary condition on heat transfer can only be assessed experimentally or through computational fluid-dynamics (CFD) analysis. To account for this issue, for flow maldistribution and for the other minor effects described in Section 1.2.2, a safety factor is introduced. Plate-fin heat exchangers having fully developed laminar flows are generally dimensioned considering the magnitude of the analytical *Nu* reduced by a minimum of 10% [23].

2.4.2 Hydraulic Design

The pressure drop admitted in the distribution elements is treated in Section 2.3.2 and 2.3.3, and it is already accounted trough equation (2.91). For a plate-fin heat exchanger, the total pressure drop on one side of the core can be expressed as [23]:

$$\Delta p = \Delta p_{fr} + \Delta p_{acc} + \Delta p_{in} + \Delta p_{out} \quad \textbf{(2.117)}$$

where Δp_{fr} is the pressure drop produced by fluid friction; Δp_{acc} is the contribution

caused by density variations; Δp_{in} is the core entrance pressure drop; Δp_{out} is the core exit pressure rise. Since the equations are identical for the hot- and the cold-side, the subscripts $_h$ and $_c$ are omitted for the sake of brevity.

The term representing the effects of fluid friction usually includes the change in the momentum rates of developing flows; if $L > L_{HD}$, it can be expressed as:

$$\Delta p_{fr} = \frac{1}{2}\,\rho\,u^2\,\frac{4\,f_{app}}{D_H}L = \frac{1}{2}\,\rho\,u^2\,\left(4\frac{L}{D_H}f + K_\infty\right) \qquad \textbf{(2.118)}$$

The apparent friction factor f_{app} depends on the channel shape and can be found in tables and charts [23]; if the channel length is greater than the hydrodynamic entrance length, f_{app} becomes:

$$f_{app} = f + \frac{D_H}{4\,L}K_\infty \qquad \textbf{(2.119)}$$

where the Hagenbach's factor K_∞ is given by the following curve-fit correlation [22]:

$$K_\infty = 0.680 + 1.220\,a + 3.309\,a^2 - 9.592\,a^3 + 8.909\,a^4 - 2.996\,a^5 \qquad \textbf{(2.120)}$$

The change of the momentum rate in the core caused by the flow acceleration (or deceleration) due to density variation across the heated (or cooled) channels produces the following pressure drop (or rise) [23]:

$$\Delta p_{acc} = \rho^2\,u^2\left(\frac{1}{\rho_{out}} - \frac{1}{\rho_{in}}\right) \qquad \textbf{(2.121)}$$

To estimate the core entrance and exit contributions, the contraction and expansion loss coefficients due to area changes K_c and K_e are available in charts as functions of σ, the ratio of the free flow areas on the considered side to the corresponding frontal area [22] [85]; the pressure variations are then calculated as:

$$\Delta p_{in} = \frac{\rho^2\,u^2}{2\,\rho_{in}}(1 - \sigma^2 + K_c) \qquad \textbf{(2.122)}$$

$$\Delta p_{out} = -\frac{\rho^2\,u^2}{2\,\rho_{out}}(1 - \sigma^2 - K_e) \qquad \textbf{(2.123)}$$

The same equations and charts can be used to determine the pressure drop across the connection between the piping and the headers [23]; in this case, the following expression are suggested:

$$K_c = 0.4\,(1-\sigma) \tag{2.124}$$

$$K_e = (1-\sigma)^2 \tag{2.125}$$

And the free flow area ratio becomes:

$$\sigma = \frac{S_{pipe}}{S_{head}} < 1 \tag{2.126}$$

Usually, in (2.117) the frictional term is dominant, accounting for more than 90 % of the total pressure drop [23]. If the hydrodynamic entrance effect is neglected coherently with the assumption of Section 1.2.2, equation (2.118) reduces to (1.13), conveniently rewritten here for both sides:

$$\Delta p_{fr,h} = \frac{2\,\mu_h\,\dot{m}\,Po_h\,(L_h+\tau)}{\rho_h\,S_h\,D_{H,h}^2} \tag{2.127}$$

$$\Delta p_{fr,c} = \frac{2\,\mu_c\,\dot{m}\,Po_c\,(L_c+\tau)}{\rho_c\,S_c\,D_{H,c}^2} \tag{2.128}$$

Equations (2.127) and (2.128) represent the only contribution considered in the optimization process, a common practice also in direct-sizing methods [73]. The other terms will then be evaluated only for the optimal design.

The Poiseuille number is approximated by the following correlations with a maximum overestimation of 0.05 % with respect to the analytically determined values for fully-developed flows, which depend only on the channel aspect ratio [84]:

$$Po_h = 24\,(1 - 1.3553\,a^{-1} + 1.9467\,a^{-2} - 1.7012\,a^{-3} + 0.9564\,a^{-4} - 0.2537\,a^{-5}) \tag{2.129}$$

$$Po_c = 24\,(1 - 1.3553\,b^{-1} + 1.9467\,b^{-2} - 1.7012\,b^{-3} + 0.9564\,b^{-4} - 0.2537\,b^{-5}) \tag{2.130}$$

For the same reasons that lead to consider lower *Nu* for plain fin geometries, it is advised to increase the value of the analytical *Po* by a minimum of 10% for design

purposes [23].

The ratio of the Nusselt number from (2.115) to the Poiseuille number of (2.129) may now be plotted as a function of a, as shown in Figure 16. It should be noted that, multiplying the mentioned ratio by $Pr^{-1/3}$, the surface flow area goodness factor is obtained: a surface having a higher ratio is good because it will require lower free-flow area and hence lower frontal area for the exchanger [23]. Observing Figure 16, it is clear that high aspect ratios are more convenient, as was also found in Section 2.2.2. The minimum channel aspect ratio introduced in the same section can be obtained compelling the area goodness factor to be a high percentage of the maximum reachable value. The following implicit equation can be solved iteratively to find a_{min} for given a_{max}, using the correlations (2.115) and (2.129):

$$\left(\frac{Nu}{Po}\right)_{a_{min}} = \left(1 - \frac{1}{a_{max}}\right)\left(\frac{Nu}{Po}\right)_{a_{max}} \qquad \textbf{(2.131)}$$

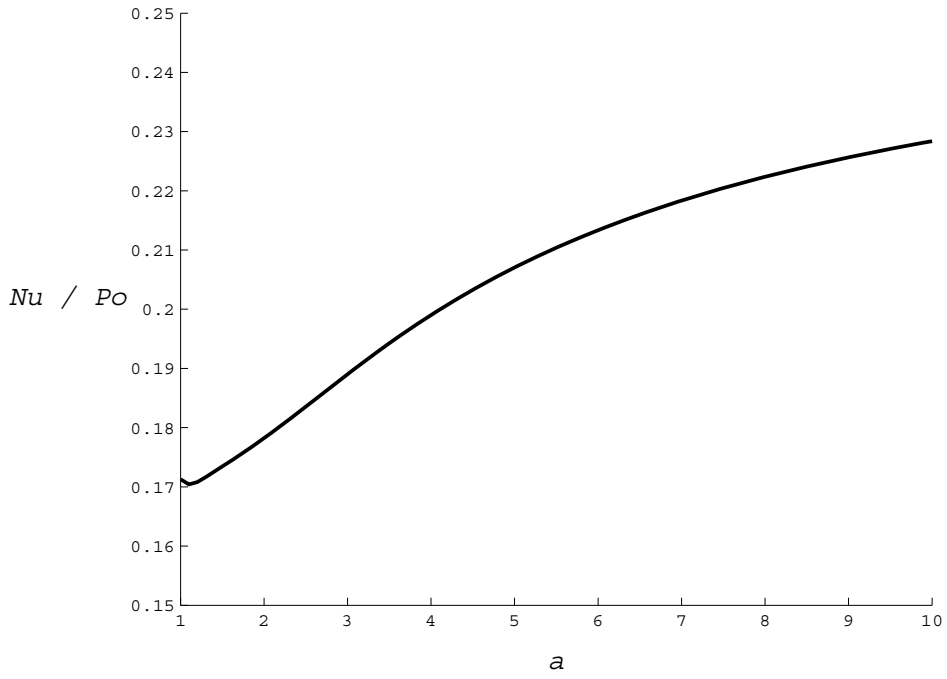

Figure 16: ratio of the Nusselt number to the Poiseuille number as a function of the aspect ratio

2.4.3 First Attempt Solutions

In the above sections, several constraints on the design parameters of Figure 6 are determined in order to select the appropriate design space. These constraints are conveniently summarized in Table 4; as it can be easily noticed, only the constraints on *s* and *d* are defined starting merely from input data, since the other constraints depend indeed on *s* and *d*: therefore, the design space for the other design parameters are generated after the selection of a value for *s* and *d* in their already defined design space.

For each parameter, the corresponding design space is discretized to generate a finite number of values to be tested. For every combination of these values, the smallest Natural number of modules N_m necessary to fulfill the thermal requirements is found considering equations (2.20) (2.107) and (2.108). If the wall thermal resistance is negligible, as it usually is in heat exchangers characterized by thin walls with high thermal conductivity, especially when at least one of the two fluids is gaseous [23], N_m can be written as:

$$N_m = \text{ceil}\left[1 + \frac{UA}{2}\left(\frac{1}{\eta_{o,h}\, h_h\, A_h} + \frac{1}{\eta_{o,h}\, h_h\, A_h}\right)\right] = N_\varepsilon \qquad \textbf{(2.132)}$$

It should be noted that neglecting the wall thermal resistance does not simplify the form of (2.132), but it is ignored to save computational time while calculating the first attempt solution. In addition, also the more accurate model, reported in the following section and used to refine the solution, does not account for the wall thermal resistance. What makes the (2.132) simple to handle, is the assumption of constant heat transfer coefficient as functions of the aspect ratio only. The non-linearity of the problem is then confined on *s*, *l*, *c*, and *d* through equations (2.17) (2.111) (2.115) and (2.129) for the hot-side, and the correspondent ones for the cold-side. Assigning values from the discretized design space to the mentioned parameters, which are then considered as input data and not as unknowns, the non-linearity disappears. However, in Section 2.2.1 a small contribution to the heat transfer area of the first and the last module of the stack was neglected; if accounted for, equation (2.132) would become quadratic in N_m.

Table 4: constraints on the design parameters

Parameter	Constraint	Equation
φ	$\varphi = \varphi_{min}$	(2.59)
δ	$\delta = \delta_{min}$	(2.59)
τ	$\tau = \tau_{min}$	(2.61)
s	$\sqrt{\frac{\delta\ \varphi}{a_{max}}} < s < \sqrt{\frac{\rho_w\ \delta\ \varphi}{\rho_h\ a_{min}}}$	(2.49)
	$s < \frac{\varphi\ a_{\varphi,max}}{a_{min}}$	(2.51)
d	$\sqrt{\frac{\delta\ \varphi}{a_{max}}} < d < \sqrt{\frac{\rho_w\ \delta\ \varphi}{\rho_c\ a_{min}}}$	(2.54)
	$d < \frac{\varphi\ a_{\varphi,max}}{a_{min}}$	(2.56)
l	$\frac{\delta\ \varphi}{s} < l < \frac{\rho_w\ \delta\ \varphi}{\rho_h\ s}$	(2.50)
	$l < \varphi\ a_{\varphi,max}$	(2.52)
	$s\ a_{min} < l < s\ a_{max}$	(2.53)
c	$\frac{\delta\ \varphi}{d} < c < \frac{\rho_w\ \delta\ \varphi}{\rho_c\ d}$	(2.55)
	$c < \varphi\ a_{\varphi,max}$	(2.57)
	$d\ a_{min} < c < d\ a_{max}$	(2.58)
N_h	$N_h = \frac{\frac{4\ S_{opt}}{\pi\ (D_h + \tau)} - \varphi}{s + \varphi}$	(2.93)
N_c	$\frac{D_c + \tau - \varphi}{d + \varphi} < N_c < \frac{L_{max} - \tau - \varphi}{d + \varphi}$	(2.98)

The pressure drop is then evaluated for both sides from (2.127) and (2.128), considering also (2.10) (2.11) and (2.27) (2.28):

$$\Delta p_{fr,h} = \frac{2\,\dot{m}\;\mu_h\,Po_h\,(L_h+\tau)}{l\;s\;N_h\;D_{H,h}^2\;\rho_h}\;\frac{1}{N_m+1} = \frac{P_h}{N_m+1} \tag{2.133}$$

$$\Delta p_{fr,c} = \frac{2\,\dot{m}\,\mu_c\,Po_c\,(L_c+\tau)}{c\;d\;N_c D_{H,c}^2\;\rho_c}\;\frac{1}{N_m} = \frac{P_c}{N_m} \tag{2.134}$$

where P_h and P_c are coefficients depending on all the design parameters of Figure 6 except N_m. Since in the ORC heat recovery system the working fluid passes firstly through one side of the microchannel regenerator and then through the other, the above equations are summed to give the total frictional pressure drop Δp_{tot} in the MCHE core:

$$\Delta p_{tot} = \Delta p_{fr,h} + \Delta p_{fr,c} = \frac{P_h}{N_m+1} + \frac{P_c}{N_m} \tag{2.135}$$

while the total weight of the MCHE is expressed as:

$$\begin{aligned}\omega_{tot} = \rho_w\left(V_w + V_{head,in,h} + V_{head,in,c} + V_{head,out,h} + V_{head,out,c}\right)\\ + \rho_c\left(V_c + V_{fluid,in,c} + V_{fluid,out,c}\right)\\ + \rho_h\left(V_h + V_{fluid,in,h} + V_{fluid,out,h}\right) = N_m\,W_1 + W_2\end{aligned} \tag{2.136}$$

where W_1 and W_2 are found considering equations (2.13) (2.14) (2.60) (2.75) (2.79) (2.81) and (2.82):

$$W_1 = W_1\left(s\,,l\,,c\,,d\,,\varphi\,,\delta\,,\tau\,,z_{h,in}\,,z_{h,out}\,,y_{h,in}\,,y_{h,out}\,,N_h\,,N_c\right) \tag{2.137}$$

$$W_2 = W_2\left(s\,,l\,,c\,,d\,,\varphi\,,\delta\,,\tau\,,z_{h,in}\,,z_{h,out}\,,y_{h,in}\,,y_{h,out}\,,N_h\,,N_c\right) \tag{2.138}$$

In equation (2.135) and (2.136), N_m is collected to reduce the computational time of the optimization process, as the refinement of the solution consists in increasing progressively N_m until the conjugate effect is counterbalanced, or until the weight or the pressure drop exceed the maximum values imposed. All the equations are manipulated and simplified using Wolfram Mathematica in order to reduce the number of operations in the optimization process and therefore the computational time.

2.4.4 Final Design

If conjugate effects are taken into account, there is no clean analytical solution to solve the unmixed crossflow problem, nor a numerical solution that can be coded without some effort [73]. The most recommended [21] [23] method, proposes a set of three partial differential equations, from which a non-homogeneous linear system is obtained employing a successive substitution technique on a finite difference formulation of the governing equations. This system is composed by linear equations equal in number to the cells of the two-dimensional domain properly discretized, and it can be solved with traditional algorithms pre-implemented in MATLAB. In other words, this approach consists in writing simultaneous finite-difference expressions to be loaded in a matrix for direct solution [73]. The output is an array containing the values of the wall temperature in each cell, from which the fluid temperature in each node is calculated, recalling the recursive formulas used for the successive substitutions. The temperature field is then completely determined along with the heat exchanger effectiveness.

This model is fully described in [40]; here, the main equations are rewritten in a form suitable for the implementation in MATLAB, maintaining where possible the original nomenclature. The results of the numerical method (values of the effectiveness as a function of several parameters) are also presented in [23], in an easily reproducible manner appropriate for the validation of the MATLAB script.

The governing equations are:

$$\frac{\partial T_h}{\partial x} = \frac{\eta_{o,h}\, h_h\, A_h}{L_h\, C_h}\, (T_w - T_h) \tag{2.139}$$

$$\frac{\partial T_c}{\partial y} = \frac{\eta_{o,c}\, h_c\, A_c}{L_c\, C_c}\, (T_w - T_c) \tag{2.140}$$

$$k_w\, A_{w,h}\, L_h\, \frac{\partial^2 T_w}{\partial x^2} + k_w\, A_{w,c}\, L_c\, \frac{\partial^2 T_w}{\partial y^2} = L_h\, C_h\, \frac{\partial T_h}{\partial x} + L_c\, C_c\, \frac{\partial T_c}{\partial y} \tag{2.141}$$

These equations are obtained from a power balance on the two fluids and the dividing wall, and are written for geometries such as the one of Figure 7. Several hypotheses are

made, coherently with those listed in Section 1.2.2. In addition, it is assumed uniform distribution of the heat transfer area, uniform temperature on the channel cross section, negligible thermal resistance through the exchanger wall in the direction normal to the fluid flows. It should be noticed that the fluid properties and the heat transfer coefficients are supposed constant along the channels. However, this approach would be adaptable, through an iterative process, to the case of varying conditions through the exchanger [73]. With some modifications, non-uniformity of the inlet temperature profiles and of the flow distribution may be introduced [86].

Defining the non-dimensional temperature of the wall Θ, of the hot fluid θ and of the cold fluid ϑ such as:

$$\Theta = \frac{T_w - T_{c,in}}{T_{h,in} - T_{c,in}} \tag{2.142}$$

$$\theta = \frac{T_h - T_{c,in}}{T_{h,in} - T_{c,in}} \tag{2.143}$$

$$\vartheta = \frac{T_c - T_{c,in}}{T_{h,in} - T_{c,in}} \tag{2.144}$$

and the non-dimensional coordinates as:

$$X = \frac{x}{L_h} \tag{2.145}$$

$$Y = \frac{y}{L_c} \tag{2.146}$$

the governing equations become:

$$\frac{\partial \theta}{\partial X} + NTU_h\,(\theta - \Theta) = 0 \tag{2.147}$$

$$\frac{\partial \vartheta}{\partial Y} + NTU_c\,(\vartheta - \Theta) = 0 \tag{2.148}$$

$$\Lambda_h\,\frac{\partial^2 \Theta}{\partial X^2} + \Lambda_c\,\varrho\,\frac{\partial^2 \Theta}{\partial Y^2} - \frac{\partial \theta}{\partial X} - \varrho\,\frac{\partial \vartheta}{\partial Y} = 0 \tag{2.149}$$

where NTU_h and NTU_c are the number of transfer units defined for the side indicated by the subscripts; Λ_h and Λ_h are the longitudinal heat conduction parameters; ϱ is the ratio of the cold fluid heat capacity rate to the hot fluid heat capacity rate. For the single plate of Figure 7, these non-dimensional parameters are expressed as:

$$NTU_h = \frac{\eta_{o,h}\, h_h\, A_h}{C_h} = 2\,(N_m - 1)\,\frac{\eta_{o,h}\, h_h\, A_h}{c_{P,h}\, \dot{m}} \tag{2.150}$$

$$NTU_c = \frac{\eta_{o,c}\, h_c\, A_c}{C_c} = 2\,N_m\,\frac{\eta_{o,c}\, h_c\, A_c}{c_{P,c}\, \dot{m}} \tag{2.151}$$

$$\Lambda_h = \frac{k_w\, A_{w,h}}{L_h\, C_h} = 2\,(N_m - 1)\,\frac{k_w\,\left[\delta\, L_c + \varphi\,(N_h + 1)\,\frac{l}{2}\right]}{L_h\, c_{P,h}\, \dot{m}} \tag{2.152}$$

$$\Lambda_c = \frac{k_w\, A_{w,c}}{L_c\, C_c} = 2\,N_m\,\frac{k_w\,\left[\delta\, L_h + \varphi\,(N_c + 1)\,\frac{c}{2}\right]}{L_c\, c_{P,c}\, \dot{m}} \tag{2.153}$$

$$\varrho = \frac{C_c}{C_h} = \frac{c_{P,c}}{c_{P,h}}\,\frac{N_m - 1}{N_m} \tag{2.154}$$

The two-dimensional domain is discretized considering constant distance between the nodes of the grid, expressed as:

$$\Delta X = \frac{1}{n_x} \tag{2.155}$$

$$\Delta Y = \frac{1}{n_y} \tag{2.156}$$

where it is considered $n_x = n_y = 10$ as suggested in the original paper. Therefore the two-dimensional domain is subdivided into 100 cells, which is sufficient to calculate the exchanger effectiveness with accuracy to the third digit [40].Then, the governing equations are written in finite difference form. By means of successive substitutions, the fluid temperatures in any node $(i\,, j)$ of the discretization grid can be related to the inlet temperature of the fluid and to the wall temperature of all the upstream subdivisions in the same flow channel, that is *i* for the hot-side and *j* for the cold-side. Bearing in mind

that the non-dimensional inlet conditions become $\theta_{in} = 1$ and $\vartheta_{in} = 0$ because of equations (2.43) and (2.44), the following recursive formulas are obtained:

$$\begin{cases} \theta_{i,j} = \left(\frac{B}{D}\right)^{j-1} + \frac{1}{D}\sum_{k=1}^{j-1} \Theta_{i,k} \left(\frac{B}{D}\right)^{j-1-k} \\ i = 1\,,2\,,\dots,n_y \\ j = 1\,,2\,,\dots,n_x + 1 \end{cases} \tag{2.157}$$

$$\begin{cases} \vartheta_{i,j} = \frac{1}{F}\sum_{k=1}^{i-1} \Theta_{k,j} \left(\frac{E}{F}\right)^{i-1-k} \\ i = 1\,,2\,,\dots,n_y + 1 \\ j = 1\,,2\,,\dots,n_x \end{cases} \tag{2.158}$$

Considering the above expressions, the third governing equation gives the wall temperature in the center of each cell $(i\,,j)$:

$$\begin{cases} G\,\Theta_{i,j+1} + H\,\Theta_{i+1,j} + W\,\Theta_{i,j} + P_1\,\Theta_{i,j-1} + P_2\Theta_{i-1,j} + P_3\sum_{k=1}^{j-2} \Theta_{i,k} \left(\frac{B}{D}\right)^{j-2-k} \\ \qquad + P_4\sum_{k=1}^{i-2} \Theta_{k,j} \left(\frac{E}{F}\right)^{i-2-k} = P_5 \left(\frac{B}{D}\right)^{j-1} \\ i = 2\,,3\,,\dots,n_y - 1 \\ j = 2\,,3\,,\dots,n_x - 1 \end{cases} \tag{2.159}$$

The above expression is also valid for the cells at the boundary of the discretized domain (i.e. when at least one of the following condition is true: $i = 1$; $j = 1$; $i = n_y$; $j = n_x$) provided that only the terms with subscripts strictly positive and not exceeding the number of cells are retained.The following coefficients are defined to obtain (2.157) (2.158) and (2.159):

$$B = \frac{1}{NTU_h\,\Delta X} - \frac{1}{2} \tag{2.160}$$

$$D = B + 1 \tag{2.161}$$

$$E = \frac{1}{NTU_c\,\Delta Y} - \frac{1}{2} \tag{2.162}$$

$$F = E + 1 \tag{2.163}$$

$$G = \frac{\Lambda_h}{(\Delta X)^2} \tag{2.164}$$

$$H = \frac{\Lambda_c\,\varrho}{(\Delta Y)^2} \tag{2.165}$$

$$R = \frac{1}{2}\,NTU_h \tag{2.166}$$

$$Z = \frac{1}{2}\,\varrho\,NTU_c \tag{2.167}$$

$$P_1 = G + \frac{R}{D}\left(1 + \frac{B}{D}\right) \tag{2.168}$$

$$P_2 = H + \frac{Z}{F}\left(1 + \frac{E}{F}\right) \tag{2.169}$$

$$P_3 = \frac{R\,B}{D^2}\left(1 + \frac{B}{D}\right) \tag{2.170}$$

$$P_4 = \frac{Z\,E}{F^2}\left(1 + \frac{E}{F}\right) \tag{2.171}$$

$$P_5 = -R\left(1 + \frac{B}{D}\right) \tag{2.172}$$

$$W = A + \frac{R}{D} + \frac{Z}{F} \tag{2.173}$$

$$A = \begin{cases} -2\,(G+H+R+Z) & \text{if } \; i = 2\,,3\,,\dots,n_y-1 \;\wedge\; j = 2\,,3\,,\dots,n_x-1 \\ -2\left(G+\dfrac{H}{2}+R+Z\right) & \text{if } \; i = 1\,,n_y \;\wedge\; j = 2\,,3\,,\dots,n_x-1 \\ -2\left(\dfrac{G}{2}+H+R+Z\right) & \text{if } \; j = 1\,,n_x \;\wedge\; i = 2\,,3\,,\dots,n_y-1 \\ -2\left(\dfrac{G}{2}+\dfrac{H}{2}+R+Z\right) & \text{if } \; (i,j) = (1,1)\,,(1,n_x)\,,(n_y,1)\,,(n_y,n_x) \end{cases} \tag{2.174}$$

The above expression is found considering that some terms of the power balance disappear for the boundary cells. In fact, adiabatic boundary condition is considered in the finite difference form of equation (2.149) by imposing zero first order derivative for the wall temperature.

The cells of the discretized domain can be numbered so as to express (2.159) with a single index, defined as:

$$\begin{cases} I = (i-1)n_x + j \\ i = 1\,,\dots,n_y \\ j = 1\,,2\,,\dots,n_x \end{cases} \tag{2.175}$$

The problem has now the form of a non-homogeneous system of $n_x\,n_y$ linear equations and can be easily solved to find Θ. The wall temperature can then be switched back to the two-index formulation employing the following relationships:

$$\begin{cases} i = \text{ceil}\left(\dfrac{I}{n_x}\right) \\ j = I - \left[\text{ceil}\left(\dfrac{I}{n_x}\right) - 1\right] n_x \\ I = 1\,,2\,,\ldots,n_x\,n_y \end{cases} \tag{2.176}$$

The hot-side outlet temperature θ_{out} is then evaluated with (2.157). From the definition (2.6) and considering also (2.143), the exchanger effectiveness is calculated as:

$$\varepsilon = \frac{T_{h,in} - T_{h,out}}{T_{h,in} - T_{c,in}} = 1 - \frac{T_{h,out} - T_{c,in}}{T_{h,in} - T_{c,in}} = 1 - \theta_{out} = \varepsilon_{\Lambda} \tag{2.177}$$

Since the chances to make mistakes while building the matrix of coefficients of the linear system are many, the validation of the MATLAB script is necessary. As already mentioned, the results published in [23] are a suitable reference.

2.5 Optimization Process

Despite of the intricate formulation, the method described in Section 2.4.4 is rapidly computed. Therefore an iterative procedure can be established to refine the first attempt design of Section 2.4.3 by taking conjugate effects into account. The method consists in a progressive increase of the number of modules N_m , keeping the geometry of the modules fixed. In fact, as described in Section 1.2.2, conjugate effects reduce the heat exchanger performance, deteriorating its effectiveness and making necessary additional heat transfer surface: if the modules geometry is fixed, the only way to provide larger area is increasing N_m. At each iteration, equation (2.177) is evaluated with the new value of N_m, until the thermal requirement represented by (2.6) is fulfilled. The final design for the considered module geometry is then obtained.

Each combination of the design parameters of Table 4 gives a fixed module geometry; however, aiming to reduce the computational time, some of them may be discarded

before being fed to the iterative procedure introduced above. This can be done defining minimum and maximum values for N_m, to be compared with the N_ε resulting from the first attempt solution. From (2.135), approximating N_m with $N_m - 1$:

$$N_m > 1 + \frac{P_c + P_h}{\Delta p_{max}} = N_{\Delta p} \tag{2.178}$$

The approximation is valid for $N_m \gg 1$, otherwise (2.178) can be substituted with the only acceptable solution of a quadratic equation. Moreover, from (2.136):

$$N_m < \frac{\omega_{max} - W_2}{W_1} = N_\omega \tag{2.179}$$

The quantities Δp_{max} and ω_{max} , corresponding to the maximum allowable pressure drop and weight, are defined in (2.1) and (2.2); however, during the optimization process, ω_{max} is progressively substituted whenever a final design with lower weight is found.

Then, the condition to be respected in order to start the iterative procedure is:

$$\max\left(N_\varepsilon \ , \ N_{\Delta p}\right) < N_\omega \tag{2.180}$$

If this condition is false conjugate effects are not calculated, the considered geometry is discarded and the algorithm proceeds to the first attempt design of the next fixed geometry (or combination of parameters).

In the opposite case, a suitable increment of N_m must be determined at each iteration, but some considerations on the shape of the curve $\varepsilon(N_m)$ are needed first. From the conventional heat exchanger theory (see Section 2.4.1) where conjugate effects are neglected, it is well-know that t $\varepsilon(NTU)$ is a concave function, as it maintains a negative second order derivative for all NTU. Also $\varepsilon(N_m)$ is a concave function: in fact, considering equations (2.107) and (2.132), and that N_m is increased keeping the modules geometry fixed, NTU becomes proportional to N_m:

$$NTU = \frac{UA}{c_{p,h}\,\dot{m}} = \frac{2(N_m - 1)}{\dfrac{1}{\eta_{o,h}\,A_h\,h_h} + \dfrac{1}{\eta_{o,c}\,A_c\,h_c}} \tag{2.181}$$

It can be assumed that these considerations remain true if axial heat conduction is taken

into account, since conjugate effects are not likely to alter qualitatively this general behavior. The only expected difference is a lower curve, as a consequence of the degradation of the exchanger effectiveness [40]. Then, at the iteration *i*, the increment ΔN_i of the number of modules $N_m = N_i$ for the following iteration can be defined as:

$$\begin{cases} \Delta N_i = \dfrac{\varepsilon - \varepsilon_i}{\varepsilon_i - \varepsilon_{i-1}} \Delta N_{i-1} \\ i = 2\,,3\,,\ldots \end{cases} \tag{2.182}$$

which is the increment that would be necessary to obtain the required effectiveness ε if the function $\varepsilon(N_m)$ was linear and coincident with the line passing by $(N_{i-1}\,,\ \varepsilon_{i-1})$ and $(N_i\,,\ \varepsilon_i)$. Because of the concave shape of (N_m) , the linear function is greater for all $N_m > N_i$; therefore, the increment will always be lower than the necessary, consenting to approach the required effectiveness avoiding the risk of crossing it. In the firsts iterations (except the very first) the increment will be larger depending on how far is the solution, accelerating the convergence.

To initiate the recursive formula (2.182), at the first iteration ε_1 is calculated starting with $N_1 = \max(N_m\ ,\ N_{m,min})$ from equation (2.180); then it is imposed $\Delta N_1 = 1$ to obtain the number of modules for the next iteration, evaluated with the following expression:

$$\begin{cases} N_{i+1} = N_i + \Delta N_i \\ i = 1\,,2\,,\ldots \end{cases} \tag{2.183}$$

The iterative process is truncated if one of the following conditions is verified:

- the required effectiveness ε is reached
- the maximum allowable weight ω_{max} is reached, i.e. when $N_m > N_\omega$
- the increment ΔN_m becomes negative

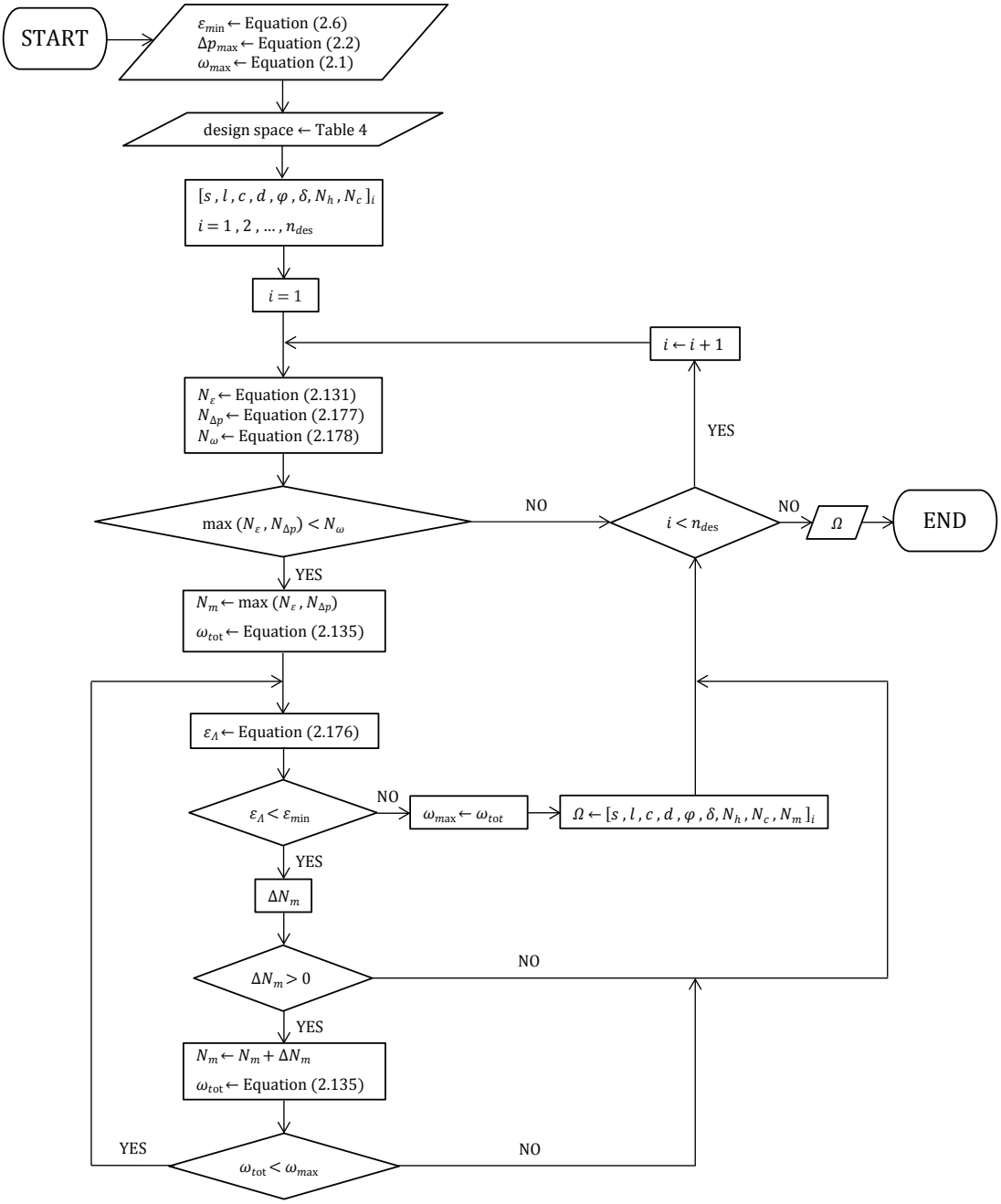

Figure 17: flow chart of the optimization process

If the reason of the truncation is the first of the above, the final design is saved and ω_{max} is updated. The saved design respects the hydraulic requirements because of (2.180) and, because the reason of the truncation, fulfills the thermal requirements, accounting for the performance degradation caused by conjugate heat transfer. This

design also is lighter than all the previously saved design, otherwise the reason of truncation would have been the second. The last motivation would indicate that increasing N_m the effectiveness is reduced, because the conjugate effects overcome the benefits of additional heat transfer area: in fact also the longitudinal heat conduction parameters Λ_h and Λ_h of equations (2.152) and (2.153) are proportional to N_m . A simplified flow diagram of the optimization process is reported in Figure 17.

2.6 Counterflow Configuration

The method proposed in the above sections for a crossflow MCHE is easily traduced for counterflow arrangement. The only difference in the parameterization of the geometry is that s, d, N_h , and N_c are no longer independent, since the channel lengths defined by (2.8) and (2.9) are equal. The width L_w of the modules represents the link between the above mentioned variables:

$$L_w = d\,N_c + \varphi\,(N_c + 1) + \tau = s\,N_h + \varphi\,(N_h + 1) + \tau \qquad \textbf{(2.184)}$$

An additional parameter, the channel length L, is then considered; equation (2.99) is suitable to define the upper limit of L, while as lower limit it is arbitrarily considered τ. This value could probably be augmented since too short channels are characterized by elevated conjugate effect. However it is not possible to define a constraint involving the longitudinal heat conduction parameter since, as from equation (2.152), it is a function of N_m, the dependent variable of the optimization process. For the same reason, an upper limit involving pressure is not considered. Therefore, the constraints on L are simply:

$$\tau < L < L_{max} \qquad \textbf{(2.185)}$$

A suitable value for L_w is obtained considering the distribution elements. As already mentioned, the headers for the counterflow configuration are more complicated than those for the crossflow arrangement described in Section 2.3.3. Various types of distributors can be used for plate-fin heat exchangers [74]. However, microchannel devices often employ manifolds and ports which are similar to the typical distribution elements of plate heat exchangers [56] [67] [87]. The risk of flow maldistribution in

MCHE employing such distributors is high. In-depth numerical analysis is needed for a proper design [67], which is beyond the purposes of the present work. Nevertheless a few geometrical considerations can be made.

The values of D_h and D_c given in Section 2.3.2 are chosen as diameters of the circular ports. The sketch in Figure 18, roughly representing the distributor of one single module, is completely determined by L_w . The total area A_{head} of the drawing is calculated by the CAD software employed, Solid Edge. In Figure 19, A_{head} and A_{head}/L_w are plotted as a function of L_w . From the latter function, it can be inferred that the larger L_w the lighter is the device. In fact, for given channel dimensions, less modules (but with more channels) are needed, reducing the contribution of the distributors (and of the frame) to the total weight. However, larger L_w is likely to increase flow maldistribution, since the path followed by the various streamlines become more and more different. The choice of L_w such that A_{head} is minimized seems a good compromise:

$$L_w = 0.18346 \text{ [m]} \tag{2.186}$$

Equation (2.184) then gives:

$$N_h = \frac{L_w - \tau - \varphi}{s + \varphi} \tag{2.187}$$

$$N_c = \frac{L_w - \tau - \varphi}{d + \varphi} = \frac{s + \varphi}{d + \varphi} N_h \tag{2.188}$$

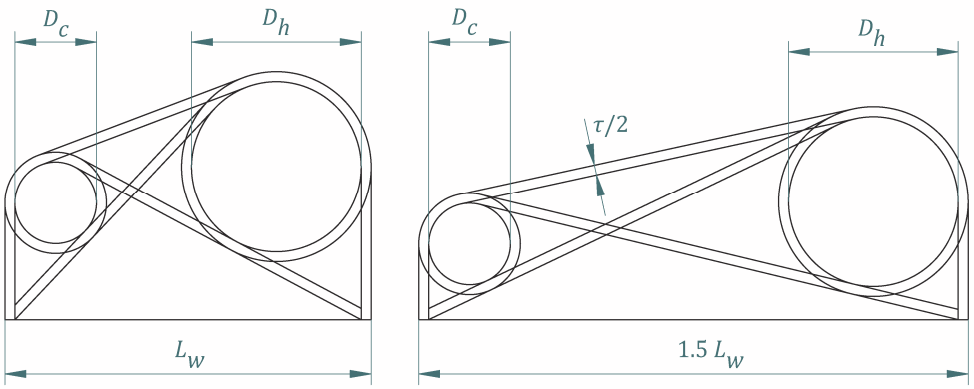

Figure 18: sketch of the distributors

In Figure 20, the modules for the crossflow configuration are shown. These modules are obtained connecting the distributors sketched in Figure 18 to the finned core elements of Figure 6. Depending on the wall thickness and on the pressure difference between the two sides of the exchanger, additional finned surface or pillars may be needed in the distributors to avoid deformation. Generally, these elements alter significantly the velocity and pressure profiles, and numerical simulations are required for an accurate designed [67].

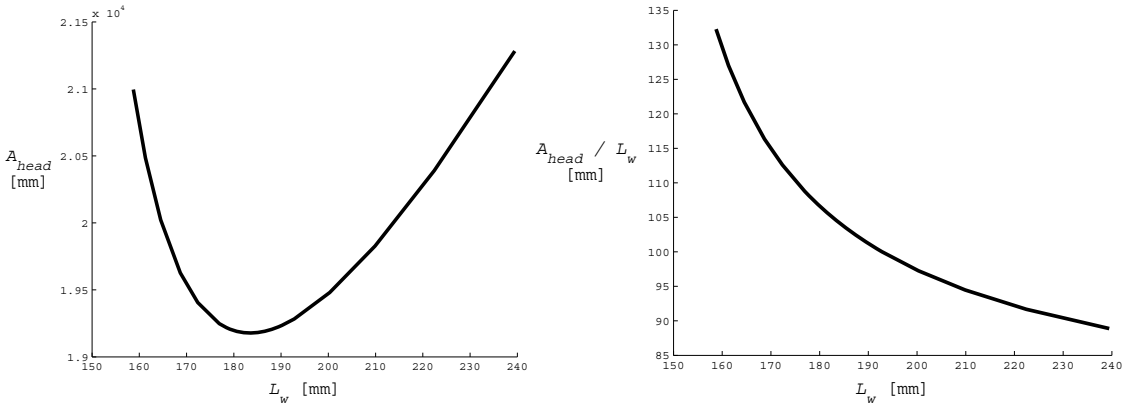

Figure 19: surface area and effective height of the distributors as a function of the exchanger width

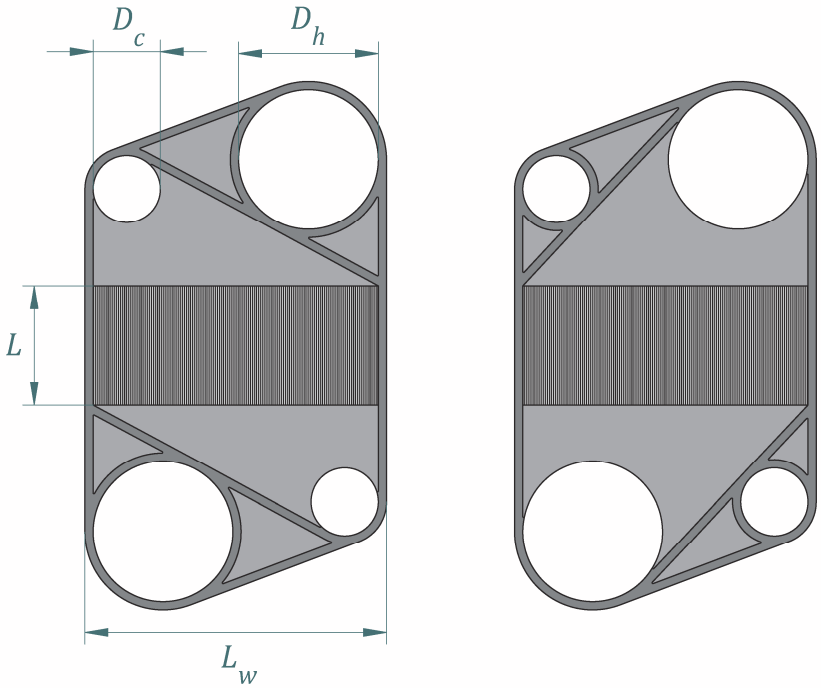

Figure 20: cold- and hot-side modules for the counterflow arrangement

The pressure drop in distributors similar to those in Figure 20 is often of the same order of magnitude as the core pressure drop. The following expression, obtained experimentally, is recommended [23]:

$$\Delta p_{head,h} = \frac{1.5 \left[\frac{\dot{m}}{\frac{\pi}{4} D_h^2}\right]^2}{2\,\rho_{h,in}} = 2575 \text{ [Pa]} \tag{2.189}$$

$$\Delta p_{head,c} = \frac{1.5 \left[\frac{\dot{m}}{\frac{\pi}{4} D_c^2}\right]^2}{2\,\rho_{c,in}} = 36 \text{ [Pa]} \tag{2.190}$$

From equation (2.2), the allowable pressure drop for the microchannel core then becomes:

$$\Delta p_{max} = 3226 - \Delta p_{head,h} - \Delta p_{head,c} = 615 \text{ [Pa]} \tag{2.191}$$

The volumes to be considered in the optimization process are:

$$V_h = s\,l\,L\,N_h\,(N_m - 1) + \frac{\pi}{4} D_h^2\,L_m + 7.839 \cdot 10^{-3}\,(N_m - 1)\,l \tag{2.192}$$

$$V_c = c\,d\,L\,N_c\,N_m + \frac{\pi}{4} D_c^2\,L_m + 6.463 \cdot 10^{-3}\,N_m\,c \tag{2.193}$$

$$\begin{aligned} V_w = L\,L_w\,\delta\,(2\,N_m - 1) + c\,\varphi\,L(N_c + 1)N_m + l\,\varphi\,L(N_h + 1)(N_m - 1) \\ + L\,\tau\,(c + \delta)\,N_m + L\,\tau\,(l + \delta)\,(N_m - 1) + 37.773 \cdot 10^{-3}\tau \end{aligned} \tag{2.194}$$

$$V_{head,h} = (N_m - 1)(24.380\,\delta + 5.856\,l) \cdot 10^{-3} \tag{2.195}$$

$$V_{head,c} = N_m(24.380\,\delta + 6.702\,c) \cdot 10^{-3} \tag{2.196}$$

where the numerical values are retrieved through the CAD software and are expressed in square meters.

Another difference with respect to the crossflow arrangement is the thermal boundary condition considered to evaluate the heat transfer coefficient: in fact, the H1 boundary

condition is recommended for counterflow heat exchangers made of highly conductive materials [84]. The following correlation is then to be implemented:

$$Nu = 8.235\,(1 - 2.042\,a^{-1} + 3.085\,a^{-2} - 2.477\,a^{-3} + 1.058\,a^{-4} - 0.186\,a^{-5}) \quad \textbf{(2.197)}$$

The well-known ε-NTU relationship for counterflow exchanger gives [23]:

$$NTU = \frac{1}{1-r}\ln\frac{1-r\,\varepsilon}{1-\varepsilon} \quad \textbf{(2.198)}$$

Substituting in (2.198) the required values for r and ε reported in (2.5) and (2.6):

$$NTU = 2.9076 \quad \textbf{(2.199)}$$

From the definition of number of transfer unit NTU, replacing $\dot{m}$ and $c_{p,h}$ with the corresponding values in Table 1 and Table 2:

$$UA = 1161.7 \quad \textbf{(2.200)}$$

Then, the first attempt solution is still expressed by (2.132). The constraints of Table 4 remain valid for all the design parameters with the exception of L, N_h and N_c, for which (2.185) (2.187)and (2.188) are considered.

The model proposed in [40] and introduced in Section 2.4.4 to evaluate the conjugate effect can be adapted to the counterflow arrangement; the domain is now one-dimensional and the governing equations become:

$$\frac{\mathrm{d}T_h}{\mathrm{d}x} = \frac{\eta_{o,h}\,h_h\,A_h}{L\,C_h}\,(T_h - T_w) \quad \textbf{(2.201)}$$

$$\frac{\mathrm{d}T_c}{\mathrm{d}x} = \frac{\eta_{o,c}\,h_c\,A_c}{L\,C_c}\,(T_w - T_c) \quad \textbf{(2.202)}$$

$$k_w\,A_w\,\frac{\mathrm{d}^2T_w}{\mathrm{d}x^2} + C_h\,\frac{\mathrm{d}T_h}{\mathrm{d}x} - C_c\,\frac{\mathrm{d}T_c}{\mathrm{d}x} = 0 \quad \textbf{(2.203)}$$

from which the following recursive formulas are obtained:

$$\begin{cases} \theta_i = A^{n+1-i} + B \sum_{k=1}^{n+1-i} \Theta_{n+1-k} \; A^{n+1-i-k} \\ i = 1\,, 2\,, \dots, n+\,1 \end{cases} \tag{2.204}$$

$$\begin{cases} \vartheta_i = F \sum_{k=1}^{i-1} \Theta_k \; E^{i-1-k} \\ i = 1\,, 2\,, \dots, n+1 \end{cases} \tag{2.205}$$

$$\begin{cases} P_1\,\Theta_{i+1} + P_2\,\Theta_i + P_3\Theta_{i-1} + P_4 \sum_{k=1}^{n-1-i} \Theta_{n+1-k} \; A^{n-i-k} \\ \qquad\qquad + P_5 \sum_{k=1}^{i-2} \Theta_k \; E^{i-1-k} = P_6 A^{n-i} \\ i = 2\,, 3\,, \dots, n-1 \end{cases} \tag{2.206}$$

$$\begin{cases} P_1\,\Theta_2 + P_2\,\Theta_1 + P_4 \sum_{k=1}^{n-2} \Theta_{n+1-k} \; A^{n-1-k} = P_6 A^{n-1} \\ i = 1 \end{cases} \tag{2.207}$$

$$\begin{cases} P_2\,\Theta_n + P_3\Theta_{n-1} + P_5 \sum_{k=1}^{n-2} \Theta_k \; E^{n-1-k} = P_6 \\ i = n \end{cases} \tag{2.208}$$

To write the above equations, several quantities are defined, some of which are expressed exactly as in in Section 2.4.4 and are therefore not reported below:

$$\Lambda = \frac{k_w\, A_w}{L\, C_h} = 2\,(N_m - 1)\,\frac{k_w\,\left[\delta(\,L_w - \tau) + \varphi\,(N_h + 1)\,\frac{l}{2} + \varphi\,(N_c + 1)\,\frac{c}{2}\right]}{L\, c_{P,h}\, \dot{m}} \quad \textbf{(2.209)}$$

$$\Delta X = \frac{1}{n} \quad \textbf{(2.210)}$$

$$A = \frac{2 - \Delta X\, NTU_h}{2 + \Delta X\, NTU_h} \quad \textbf{(2.211)}$$

$$B = \frac{2\,\Delta X\, NTU_h}{2 + \Delta X\, NTU_h} \quad \textbf{(2.212)}$$

$$E = \frac{2 - \Delta X\, NTU_c}{2 + \Delta X\, NTU_c} \quad \textbf{(2.213)}$$

$$F = \frac{2\,\Delta X\, NTU_c}{2 + \Delta X\, NTU_c} \quad \textbf{(2.214)}$$

$$P_1 = \frac{\Lambda}{\Delta X} - B\,(A - 1) \quad \textbf{(2.215)}$$

$$P_2 = \begin{cases} -\left(2\dfrac{\Lambda}{\Delta X} + B + \varrho\, F\right) & \text{if } \; i = 2\,, 3\,, \dots, n-1 \\ -\left(\dfrac{\Lambda}{\Delta X} + B + \varrho\, F\right) & \text{if } \; i = 1\,, n \end{cases} \quad \textbf{(2.216)}$$

$$P_3 = \frac{\Lambda}{\Delta X} - \varrho\, F\,(E - 1) \quad \textbf{(2.217)}$$

$$P_4 = -B\,(A - 1) \quad \textbf{(2.218)}$$

$$P_5 = -\varrho\, F\,(E - 1) \quad \textbf{(2.219)}$$

$$P_6 = A - 1 \quad \textbf{(2.220)}$$

In the case of $\Lambda = 0$, the output of the MATLAB script implementing the presented model is in perfect agreement with equation (2.198); considering $n = 20$ in (2.210) is

sufficient to calculate the exchanger effectiveness with accuracy to the third digit. If $\Lambda > 0$, the results are in good agreement with the less accurate method suggested in [23] to evaluate the conjugate effects in counterflow exchangers. It should be mentioned that, because of the heat transfer and the pressure drop in the distributors, the assumption of unique mass flow rate and inlet temperature for each channel may be inadequate. In this case, the model could be adapted as described in [86].

3 Results

The MATLAB script implementing the method described in the previous chapter calculates, in only a few minutes, the design parameters of Figure 6 for the optimal crossflow and counterflow MCHE. The optimal values are searched in the design space defined by the constraints of Table 4. The optimal MCHE geometries are determined considering two different alloys for the walls. In Figure 21 the space occupied by the considered heat exchangers is visualized for a quick comparison. The optimal values of the design parameters are reported in Table 5 and Table 6, along with the discretization step used for the corresponding design space.

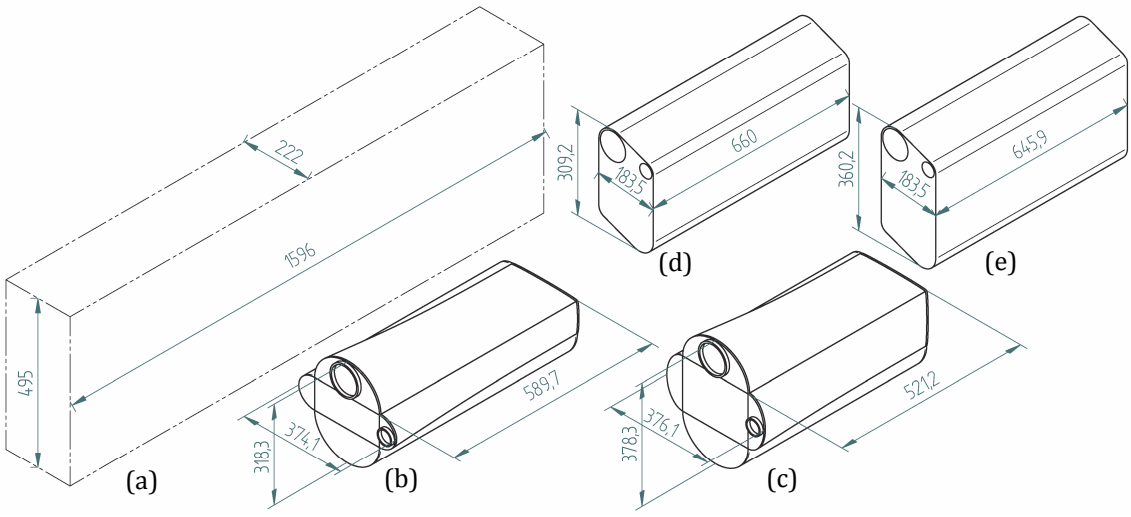

Figure 21: overall dimensions [mm] of the benchmark PHE (a), the copper (b) and aluminium (c) crossflow MCHE, the copper (d) and aluminium (e) counterflow MCHE

Table 5: optimized design parameters for the crossflow MCHE

Design parameter	Symbol	Crossflow			Unit
		C878	A360	Step	
Number of modules	N_m	106	105	—	#
Number of hot-side channels	N_h	370	320	—	#
Number of cold-side channels	N_c	120	230	10	#
Cold-side channel height	c	1.9	1.3	0.1	mm
Cold-side channel width	d	0.35	0.30	0.05	mm
Hot-side channel height	l	3.0	3.0	0.1	mm
Hot-side channel width	s	0.30	0.4	0.05	mm
Fin thickness	φ	0.30	0.30	—	mm
Dividing wall thickness	δ	0.30	0.30	—	mm
Hot-side channel length	L_h	88.3	148.3	—	mm
Cold-side channel length	L_c	232.3	234.3	—	mm
Length of the stack of modules	L_m	589.7	521.2	—	mm

Table 6: optimized design parameters for the counterflow MCHE

Design parameter	Symbol	Counterflow			Unit
		C878	A360	Step	
Number of modules	N_m	139	136	—	#
Number of hot-side channels	N_h	247	204	—	#
Number of cold-side channels	N_c	288	267	—	#
Cold-side channel height	c	1.1	1.1	0.1	mm
Cold-side channel width	d	0.30	0.35	0.05	mm
Hot-side channel height	l	3.0	3.0	0.1	mm
Hot-side channel width	s	0.40	0.55	0.05	mm
Fin thickness	φ	0.30	0.30	—	mm
Dividing wall thickness	δ	0.30	0.30	—	mm
Hot-side channel length	L	61	112	1	mm
Module width	L_w	183,2	183,9	—	mm
Length of the stack of modules	L_m	660.0	645.9	—	mm

In the following sections, the proposed devices are rated and the validity of the approximations made in the optimization process is assessed by evaluating the magnitude of the scaling effects neglected. An accurate test of the crossflow exchanger using commercial computational fluid-dynamics software such as ANSYS Fluent would require the simulation of a whole plate, due to the two-dimensional nature of the heat transfer process. An excessive number of discretization cells would be needed to resolve the temperature field inside the various microchannels, because the characteristic length of the microstructures is several orders of magnitude lower than the dimensions of the plate. On the other hand, considering a single channel for each side is sufficient to model the counterflow MCHE: numerical simulations can then be executed in acceptable computational time, for a further validation of the considered model.

As shown in Table 3, the thermal conductivity of the aluminium-based alloy A360 is four times the conductivity of the copper-based alloy C878. Conjugate effects are therefore more significant in the aluminium-based devices. Consequently, the copper-based devices are appreciably smaller. With this exception, for each flow arrangement no relevant difference is found rating the copper-based or the aluminium-based exchangers of Table 5 and Table 6: to avoid repetition, in the following sections the focus is on the copper-based crossflow and counterflow devices.

3.1 Outlet Temperatures and Effectiveness

The model described in Section 2.4.4 evaluates the exchanger effectiveness for the optimization process. To do so, it first calculates the temperature field in one single plate of the crossflow MCHE. The temperature field for the copper-based crossflow device of Table 5 is shown in Figure 22. The upper surface corresponds to the hot-side, the lower to the cold-side and the surface in the middle represents the temperature of the dividing wall.

While for the counterflow configuration the temperature at the outlet of each channel is the same, for the crossflow configuration it depends on the position of the microchannel in the core. In this case, the outlet temperature of the exchanger is the adiabatic mixing

temperature and, since uniform flow distribution is assumed, it corresponds to the arithmetic average of the outlet temperatures of the various channels. In Figure 23, the temperature distributions at the outlet of the two sides and the respective averaged value are shown.

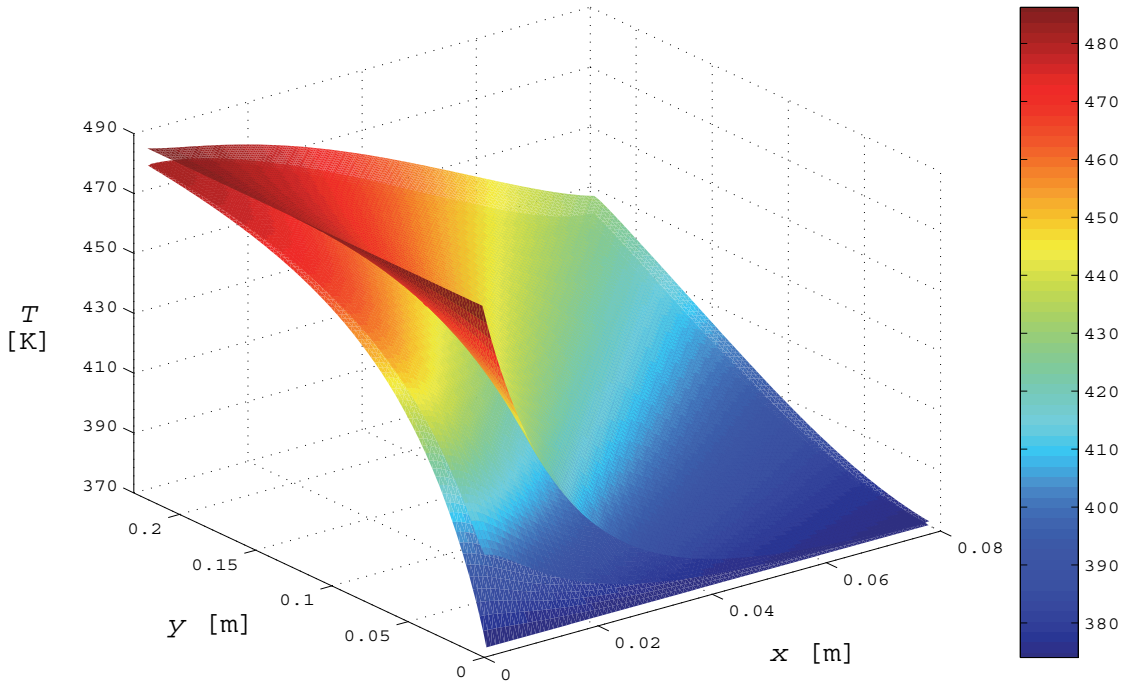

Figure 22: temperature field in one plate of the copper-based crossflow MCHE

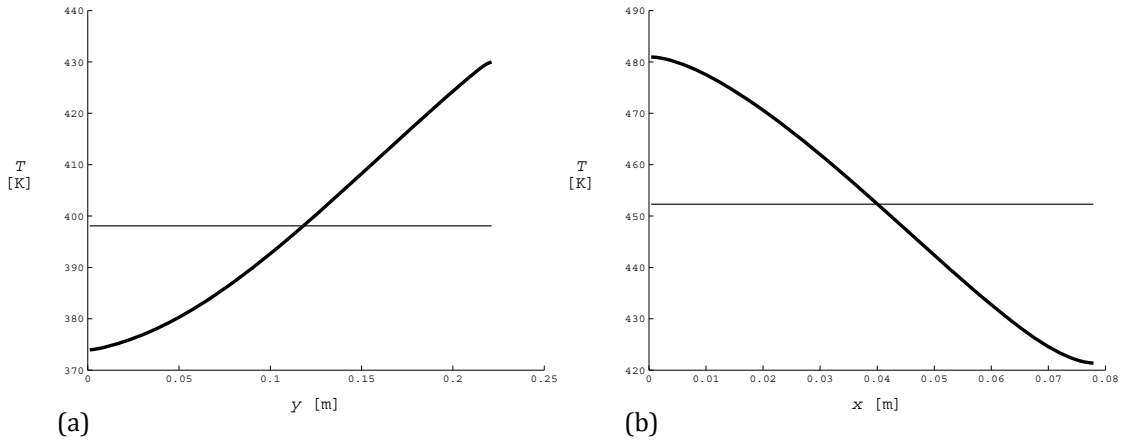

Figure 23: temperature distributions at the outlet of the hot-side (a) and of the cold-side (b)

As anticipated in Section 2.4.4, if the geometry of the modules is kept fixed, the exchanger effectiveness can be expressed as a function of the number of modules N_m only. Figure 24 shows values of the effectiveness as function of the number of modules. Observing the chart, the importance of considering conjugate effect becomes clear. The intersection between the horizontal line and the green curve represents the first attempt solution of Section 2.4.3, while the final design corresponds to the intersection between the horizontal line, the vertical line and the blue curve. A difference of 16 modules on each side exists between the two designs, corresponding to a relative error of 15.1 %. The error grows to 31.4 % if the aluminium-based MCHE is considered, due to higher thermal conductivity.

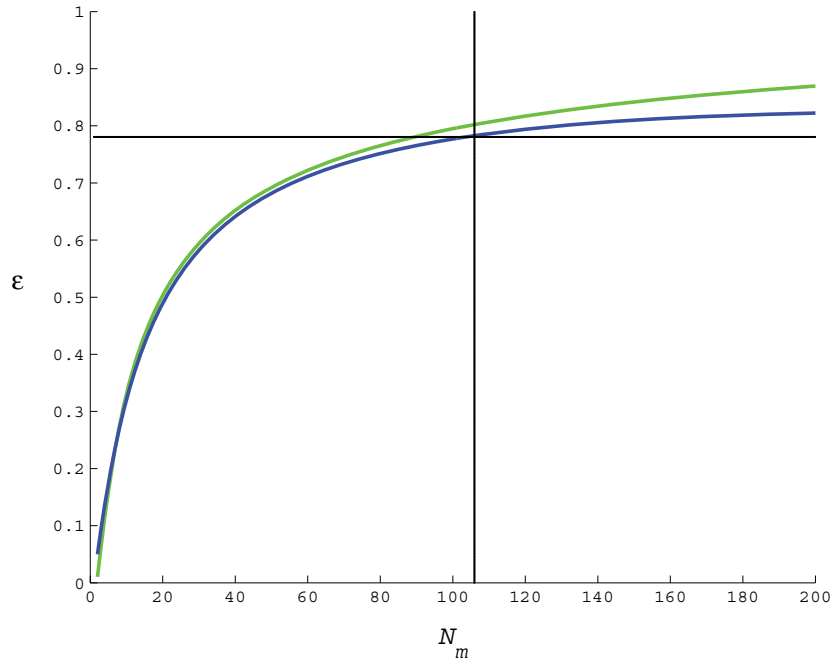

Figure 24: effectiveness of the copper-based crossflow MCHE as a function of the number of modules; the geometry of the modules is kept constant and given in Table 5; the **green** line is the effectiveness neglecting conjugate effect, calculated using (2.105); the **blue** line is the effectiveness taking conjugate effects into account, evaluated with the model of Section 2.4.4; the **black** horizontal and vertical lines mark, respectively, the required effectiveness and the number of modules needed to obtain it, and their intersection represents the optimal design

The response of the crossflow MCHE in situations involving off-design mass flow rate is visualized in Figure 25. It is evident that conjugate effects become stronger and stronger as the flow rate diminishes.

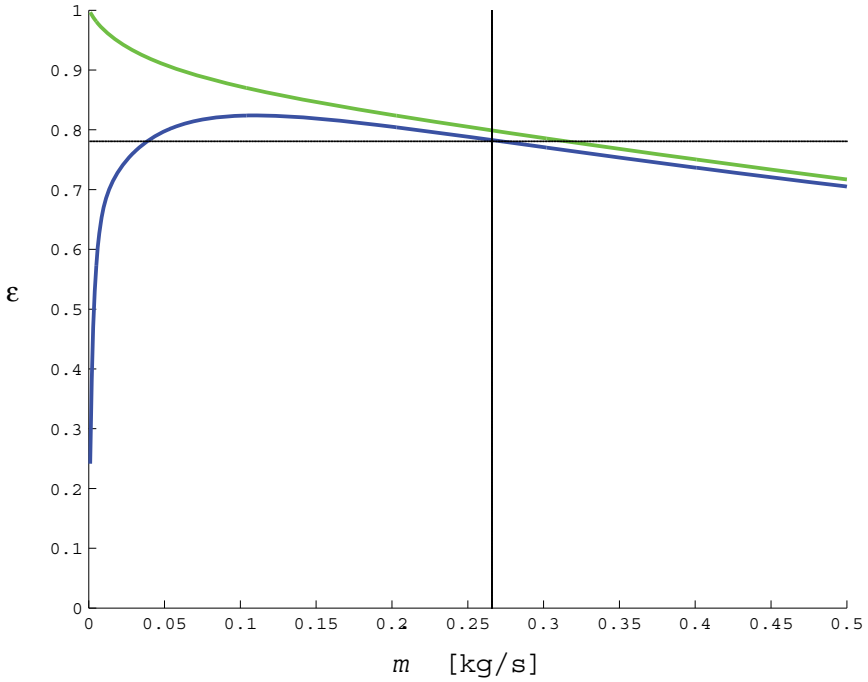

Figure 25: effectiveness of the copper-based crossflow MCHE as a function of the mass flow rate; the geometry of the exchanger is kept constant and given in Table 5; the **green** line is the effectiveness neglecting conjugate effect, calculated using (2.105); the **blue** line is the effectiveness taking conjugate effects into account, evaluated with the model of Section 2.4.4; the **black** horizontal and vertical lines mark, respectively, the required effectiveness and mass flow rate, and their intersection represents the design point

Similar conclusions are made when the counterflow geometries of Table 6 are considered.Tthe one-dimensional temperature profiles of the copper-based counterflow exchangers are shown in Figure 26, while the effectiveness is plotted as a function of the number of modules and of the mass flow rate in Figure 27. The relative error on the number of modules between the first attempt solution and the final design is 15.1 % for the copper-based MCHE and 27.2 % for the aluminium-based MCHE.

It should be noted that the results of this section are obtained neglecting the wall thermal resistance in the direction normal to the fluid flows, which, however, represents less than 1.7 % of the total thermal resistance of (2.108) for both the copper-based exchangers and less than 0.2 % for the aluminium-based devices. However, the contact resistance due to the bonds between two modules may be non-negligible [23] and should be evaluated empirically.

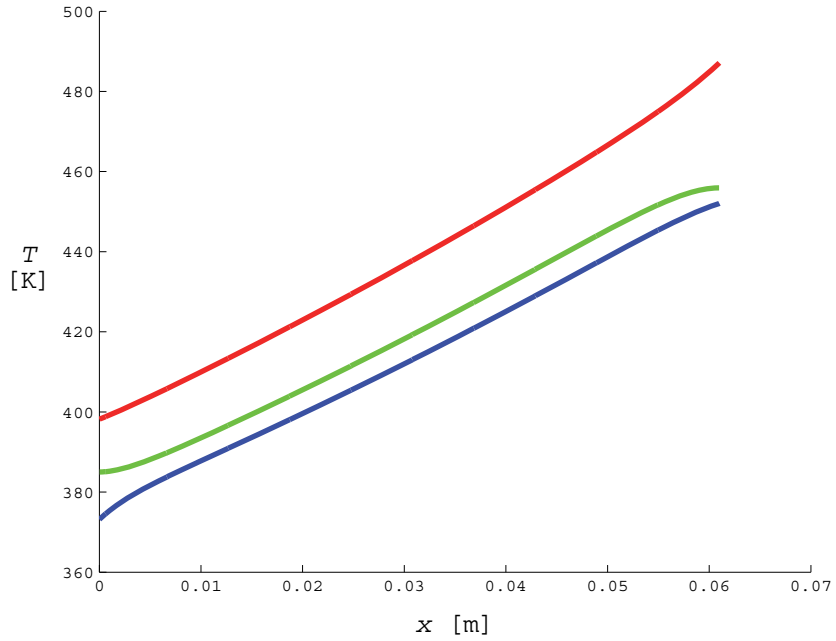

Figure 26: temperature field inside one channel of the copper-based counterflow MCHE of Table 6; the **green** line is the temperature of the dividing wall; the **blue** line is the fluid temperature on the cold-side and the **red** line is the fluid temperature on the hot-side

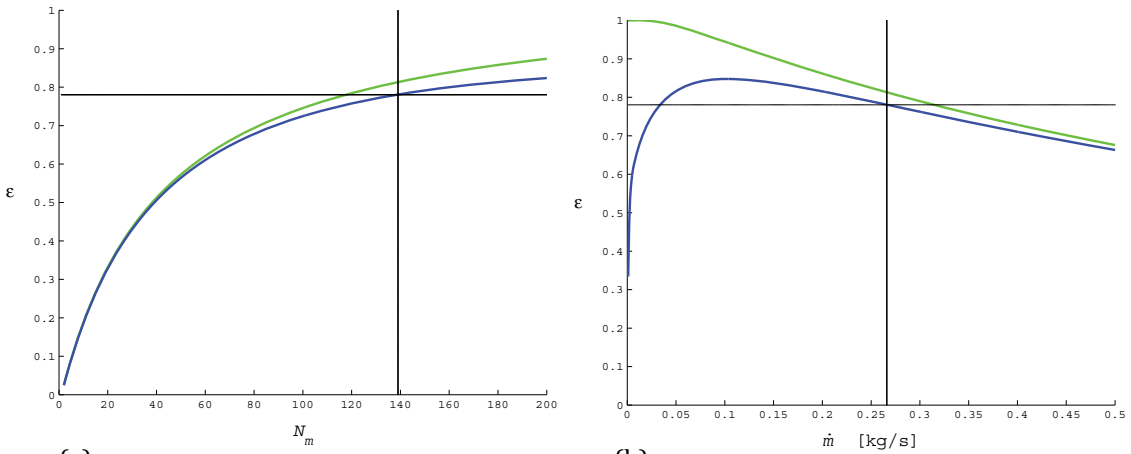

Figure 27: effectiveness of the copper-based counterflow MCHE of Table 6 as a function of the number of modules (a) and of the mass flow rate (b) (see the caption of Figure 24 and Figure 25)

3.2 Magnitude of the Scaling Effects

In the optimization process, with the exception of conjugate effects, the scaling effects are assumed as negligible. The thresholds conditions to decide if the respective scaling

effect can be neglected are discussed in Section 1.2.2 and evaluated below. Similar results are obtained for each of proposed devices, therefore, to avoid repetitions, these relationships are here evaluated only for the copper based crossflow MCHE, unless significant differences arise.

Rarefaction Effects

The threshold condition to be respected in order to safely ignore rarefaction effect is:

$$Kn = \frac{1.277}{\sqrt{\frac{R}{M}\,T}}\,\frac{\mu}{\rho\,D_C} < 10^{-3} \tag{3.1}$$

Substituting the appropriate values for the hot-side of the considered MCHE:

$$Kn = \frac{1.277}{\sqrt{\frac{8.314\,\frac{\mathrm{J}}{\mathrm{mol\,K}}}{296.61\,\frac{\mathrm{g}}{\mathrm{mol}}}\,\frac{398.15+487.15}{2}\,\mathrm{K}}}\,\frac{0.0093\,\frac{\mathrm{g}}{\mathrm{m\,s}}}{0.72\,\frac{\mathrm{kg}}{\mathrm{m^3}}\cdot 0.3\,\mathrm{mm}} = 4.9\cdot 10^{-4} < 10^{-3} \tag{3.2}$$

Rarefaction effects may therefore be neglected.

Entrance Effects

The threshold condition to be respected in order to safely ignore hydrodynamic entrance effects is:

$$\frac{L}{D_H} > 60 \tag{3.3}$$

while thermal entrance effects can be neglected if:

$$Re\,Pr\,\frac{D_H}{L} < 10 \tag{3.4}$$

Substituting the appropriate values for the hot-side of the co MCHE:

$$\frac{L_h}{D_{H,h}} = \frac{0.0883}{0.00055} = 160.5 > 60 \tag{3.5}$$

$$Re_h\, Pr_h \frac{D_{H,h}}{L_h} = 446.2 \cdot 0.8466 \frac{0.00055}{0.0883} = 2.35 < 10 \quad \textbf{(3.6)}$$

Entrance effects may therefore be neglected.

Conjugate Heat Transfer

The threshold condition to be respected in order to safely ignore conjugate effects is:

$$\Lambda = \frac{k_w\, A_w}{\dot{m}\, c_P\, L} < 0.01 \quad \textbf{(3.7)}$$

Substituting the appropriate values for the hot-side of the crossflow MCHE:

$$\Lambda_h = 0.0434 > 0.01 \quad \textbf{(3.8)}$$

Therefore conjugate effect cannot be neglected. However, since longer channels are involved, the cold-side is not appreciably influenced:

$$\Lambda_c = 0.0034 > 0.01 \quad \textbf{(3.9)}$$

On the other hand, the effect is more marked in the counterflow exchangers; for the copper-based device:

$$\Lambda = 0.0662 > 0.01 \quad \textbf{(3.10)}$$

while for the aluminium based-device, characterized by higher thermal conductivity:

$$\Lambda = 0.1285 > 0.01 \quad \textbf{(3.11)}$$

Conjugate effects are properly taken into consideration thanks to the model described in Section 2.4.4 and 2.6; if conjugate effects were not accounted for, the optimal design would be substantially different.

Surface Roughness

The threshold condition to be respected in order to safely ignore conjugate effects is:

$$\frac{\epsilon}{D_C} < 0.01 \tag{3.12}$$

For the hot-side of the crossflow MCHE, considering an appropriate value for the surface roughness retrieved from [56]:

$$\frac{\epsilon}{d} = \frac{0.01\ \text{mm}}{0.3\ \text{mm}} = 0.03 > 0.01 \tag{3.13}$$

Therefore, heat transfer and pressure drop may be slightly influenced by the roughness of the surface. However, in similar situations the relative error on the Nusselt and Poiseuille numbers is still likely to be below 1 % [43]. It should be noted that, among the devices of Table 5 and Table 6, the hot-side of the crossflow MCHE is characterized by the smallest microchannels, and is therefore the most influenced by surface roughness effect.

Variable Properties

The threshold condition to be respected in order to safely consider temperature independent properties is:

$$\left|\left(\frac{T}{\psi}\frac{\partial\psi}{\partial T}\right)_{T_r}\right| \ll 1 \tag{3.14}$$

while physical properties are independent of the pressure if:

$$\left|\left(\frac{p}{\psi}\frac{\partial\psi}{\partial p}\right)_{p_r}\right| \ll 1 \tag{3.15}$$

Considering the working pressures of Table 1 and the allowable pressure drop, the thermodynamic library employed gives physical properties substantially pressure-independent and closely linear with the temperature. Therefore, the only threshold condition to evaluate is:

$$\left|\left(\frac{T}{\psi}\frac{\partial\psi}{\partial T}\right)_{T_r}\right| = \left|\left(\frac{T}{\psi}\frac{\mathrm{d}\psi}{\mathrm{d}T}\right)_{T_r}\right| \cong \left|\left(\frac{T}{\psi}\frac{\Delta\psi}{\Delta T}\right)_{T_r}\right| \cong \left|\frac{\psi_{in}-\psi_{out}}{\psi_{in}+\psi_{out}}\frac{T_{in}+T_{out}}{T_{in}-T_{out}}\right| \ll 1 \tag{3.16}$$

where the arithmetic average between the inlet and outlet temperatures is chosen as

reference temperature.

Considering the values of Table 1 for the temperatures and of Table 2 for the various physical properties involved, the values of Table 7 are obtained:

Table 7: temperature sensitivity coefficients for the physical property of interest

Physical property	$c_{P,h}$	$c_{P,c}$	ρ_h	ρ_c	μ_h	μ_c	k_h	k_c
Sensitivity coefficient	6.52	5.26	9.33	5.25	9.14	25.80	15.86	7.95

Therefore, all the physical properties are strongly temperature dependent, both for the hot- and the cold-side. With the exception of the viscosity, the dependence from the temperature is weaker in the liquid.

In the optimization process, averaged values are calculated through an arithmetic mean between the inlet an outlet values. This choice does not introduce an excessive error in the counterflow exchangers since, as mentioned, the properties are closely directly proportional to the fluid temperature, and since, as can be seen in Figure 26, in each channel the bulk temperature is almost linearly distributed between the inlet and outlet values, contrarily to the crossflow case of Figure 22. As already mentioned, the method employed to evaluate the exchanger effectiveness could be easily adapted, through an additional iterative process, to the case of varying conditions throughout the exchanger.

Viscous Dissipation

The threshold condition to be respected in order to safely ignore viscous heating is:

$$Br = \mu\, u^2 \frac{L}{\dot{Q}} = \mu\, u^2 \frac{L}{\dot{m}\, c_P |T_{in} - T_{out}|} < 0.05 \frac{D_H^2}{2\, S\, Po} \tag{3.17}$$

Substituting the appropriate values for the hot-side of the crossflow MCHE:

$$Br_h = 2.03 \cdot 10^{-4} < 3.55 \cdot 10^{-4} = 0.05 \frac{D_{H,h}^2}{2\, l\, s\, Po_h} \tag{3.18}$$

It should be mentioned that, among the proposed devices, the hot-side of the copper-

based crossflow MCHE is the most influenced by viscous heating effect, which can be neglected according to this established thresholds.

Fluid Axial Conduction

The threshold condition to be respected in order to safely ignore heat conduction in the fluid is:

$$Pe = \frac{\rho \, c_P \, u \, D_H}{k} > 100 \tag{3.19}$$

Substituting the appropriate values for the hot-side of the crossflow MCHE:

$$Pe_h = 377.7 > 100 \tag{3.20}$$

Fluid axial conduction effects may therefore be neglected.

Electroviscous Effect

The walls of the exchangers are made of electrically conductive materials and therefore can't be charged relatively to the liquid; moreover, the working fluid can be considered as pure and does not contain a significant amount of ions. Therefore, electroviscous effects do not take place.

3.3 Total Pressure Drop

In Table 8, the various contributions to the total pressure drop of the copper-based heat exchangers are reported. The information from Section 2.3.3, 2.4.2 and 2.6 are employed to calculate the mentioned quantities.

The values of Table 8 may be used to calculate the relative error introduced with the approximations imposed for the optimization process. Both in the counterflow and crossflow configurations, considering only the pressure drop on the hot-side distribution system and the core frictional pressure drop with no entrance effect, the total pressure drop are underestimated approximately by 3 %.

Table 8: total pressure drop; all values are expressed in Pa, negative values indicate pressure rise

Contribution to pressure drop	Crossflow C878		Counterflow C878	
	Cold-side	Hot-side	Cold-side	Hot-side
Piping abrupt entrance pressure drop	31	1591	—	—
Piping abrupt exit pressure rise	-10	-775	—	—
Header pressure drop	7	444	36	2575
Core abrupt entrance pressure drop	1	78	0	54
Core abrupt exit pressure rise	0	-18	0	-16
Core frictional pressure drop	587	1368	144	465
Dynamic inlet effect	1	33	0	26
Pressure change due to density variation	0	-17	0	-13
Total pressure drop on one side	617	2704	180	3091
Total pressure drop	3321		3271	

3.4 Numerical Validation

As mentioned earlier, an accurate three-dimensional CFD analysis of the crossflow exchanger using proprietary software is impracticable, due to the excessive number of discretization cells required. On the other hand, the symmetry planes of the counterflow MCHE can be exploited to reduce the computational domain, so that the numerical analysis is executed in acceptable computational time.

Three different simulations are implemented in ANSYS Fluent considering the optimal copper-based counterflow MCHE. The first one considers constant properties and zero thermal conductivity in the axial direction, to neglect conjugate effects; the second one still involves constant properties but considers isotropic thermal conductivity, accounting therefore for longitudinal heat conduction; in the third simulation, the temperature dependence of the physical properties is defined.

The considered geometry, shown in Figure 28 as well as the boundary conditions

imposed, consists in a quarter of the hot-side and cold-side channels. The values chosen for the design parameters, reported in Table 9, are selected by the optimization process imposing $d = s$ as further constraint. In this way, each side has the same number of channels, as follows from (2.184), and each channel on one side matches exactly a channel the other side of the exchanger. Symmetry planes are formed and used to single out the element of Figure 28. The inlet temperatures and pressures of Table 1 are used as boundary conditions, together with the inlet velocities calculated as $u_{in} = \dot{m}/(\rho_{in}\, S)$.

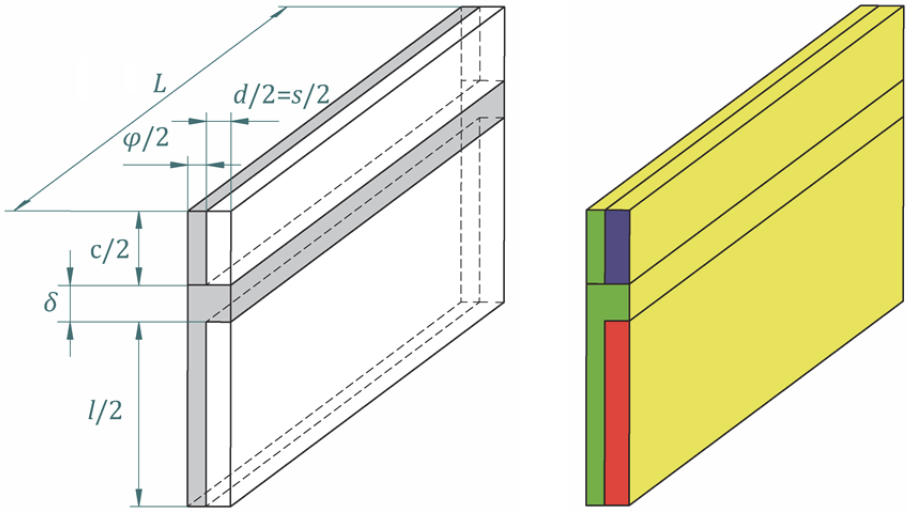

(a) (b)

Figure 28: geometry (a) and boundary conditions (b) considered for the numerical simulation of the counterflow arrangement; the region occupied by the solid wall is shown in gray while the fluid is left white; symmetry boundary condition, marked in yellow, is imposed on all the four sides of the geometry; the velocity inlet of the cold-side is filled with blue, while the pressure outlet of the hot side in red; adiabatic walls are indicated in green

Table 9: copper-based counterflow MCHE considered for the numerical simulation

Design parameter	N_m	N_h	N_c	s	d	l	c	φ	δ	L
Optimized value	120	247	247	0.4	0.4	3.0	1.2	0.3	0.3	68
Unit	[#]	[#]	[#]	[mm]	[mm]	[mm]	[mm]	[mm]	[mm]	[mm]

Since more precise data could not be found, the physical properties of the copper alloy are considered constant as reported in Table 3. On the other hand, the physical

properties of the fluid are approximated as quadratic functions of the temperature, interpolating the values of Table 2. As a matter of fact, all the fluid property are closely linear with the temperature, except the viscosity of the liquid, which, as shown in Figure 29, is well approximated by the following expression:

$$\mu_c = 8.172 \cdot 10^{-3} - 3.264 \cdot 10^{-5}\, T + 3.395 \cdot 10^{-8}\, T^2 \qquad \textbf{(3.21)}$$

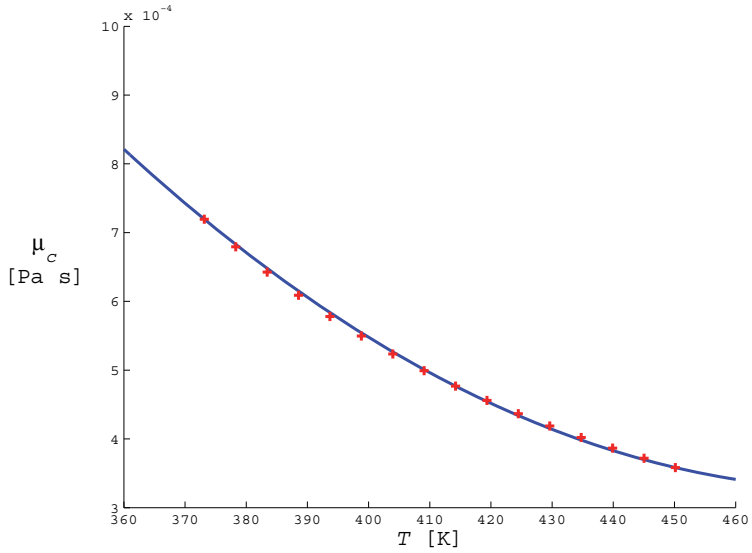

Figure 29: temperature dependence of the viscosity of the liquid; the quadratic equation (3.21), plotted in **blue**, closely approximates the data, in **red**, obtained from the considered thermodynamic library (see Section 2.1.2)

For each quantity of interest, the numerical simulation provides an array containing the values of the considered quantity in all the discretization cells. An arbitrary number of positions along the channel is chosen; at each position, the average value for each quantity is calculated manipulating the arrays in the MATLAB environment. In this way, the bulk temperature $\tilde{T}$, the wall temperature $\tilde{T}_w$, the wall heat flux $\tilde{q}_w$, the wall shear stress $\tilde{t}_w$ and the axial velocity $\tilde{u}$ are determined. For each side, these quantities are employed to evaluate the local values of the Nusselt and Poiseuille numbers as follows:

$$Nu = \frac{h\, D_H}{k} = \frac{\tilde{q}_w\, D_H}{k\left(\tilde{T}_w - \tilde{T}\right)} \qquad \textbf{(3.22)}$$

$$Po = f\, Re = \frac{2\, \tilde{t}_w\, D_H}{\mu\, \tilde{u}} \qquad \textbf{(3.23)}$$

The geometry of Figure 28 is discretized using GAMBIT. Around three millions of cells are considered: further refinement does not cause significant variations in the results, guaranteeing the independence of the solution from the mesh. The convergence of the solution is monitored by examining the residuals, shown in Figure 30, by checking relevant integrated quantities, as shown in Figure 31 and Figure 32, and, finally, by calculating mass and energy imbalances.

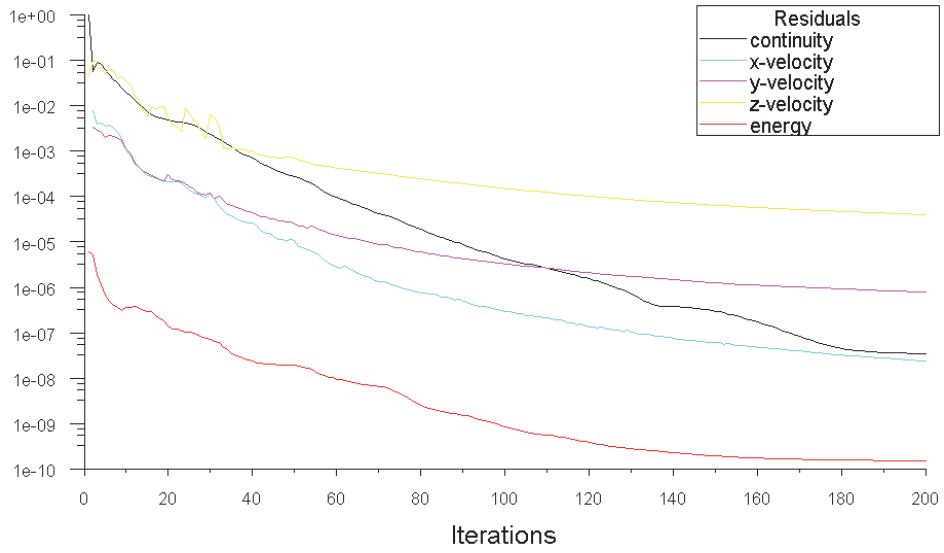

Figure 30: convergence history of the residuals for each of the conserved variables

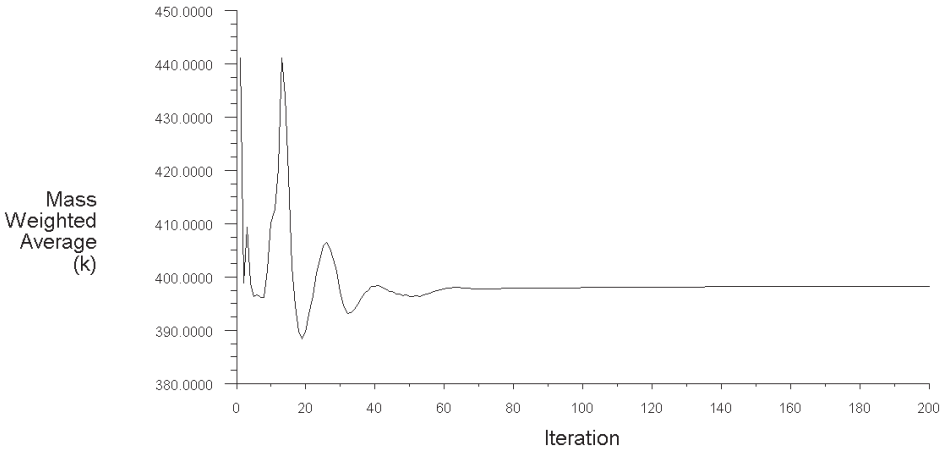

Figure 31: convergence history of the hot-side outlet bulk temperature

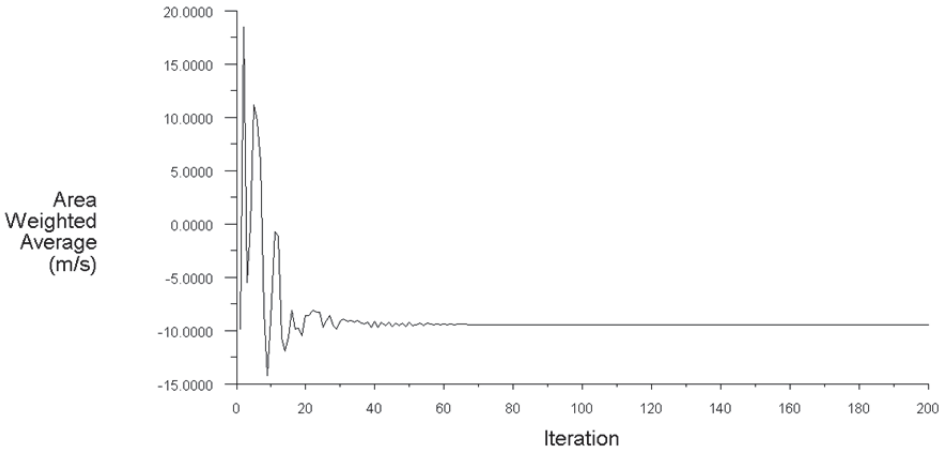

Figure 32: convergence history of the hot-side outlet axial velocity

When constant physical properties are considered, the Poiseuille number in the fully developed region matches almost perfectly the analytical values given by (2.129) and (2.130), as displayed in Figure 33. In the same figure it is shown that *Po* is significantly lowered when the momentum and the energy equations are coupled through temperature dependent properties. This alters the velocity profile and therefore the wall shear stress.

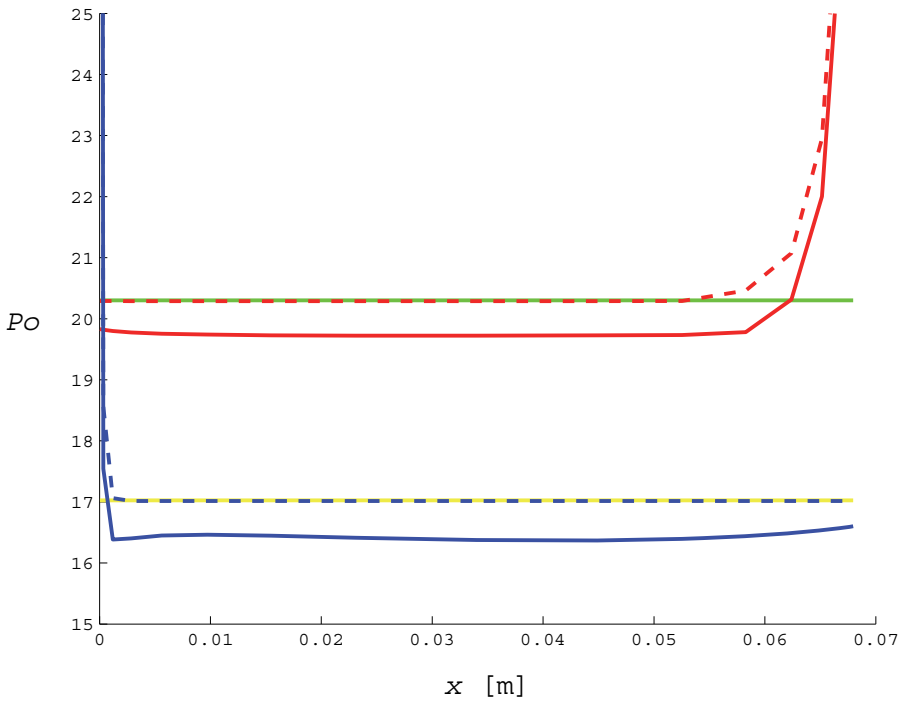

Figure 33: Poiseuille number as a function of the axial coordinate of the microchannels; the values for the hot-side are plotted in **red**, those for the cold-side in **blue**; the respective analytical values are marked in **green** and **yellow**; solid lines refer to the temperature dependent properties case while dashed lines refer to constant properties

In Figure 33 it can also be noted that the hydrodynamic entrance length is approximately 1/10 of the channel length for the hot-side, while it is much shorter for the cold-side. This is well predicted by equation (1.22): in fact the hot-side is characterized by higher Reynolds number, higher hydraulic diameter and a higher multiplying constant (for geometric reasons). The thermal entrance lengths, which can be identified in Figure 34, are similar on the two sides, due to the low viscosity of the gas, giving a lower Prandtl number for equation (1.23)

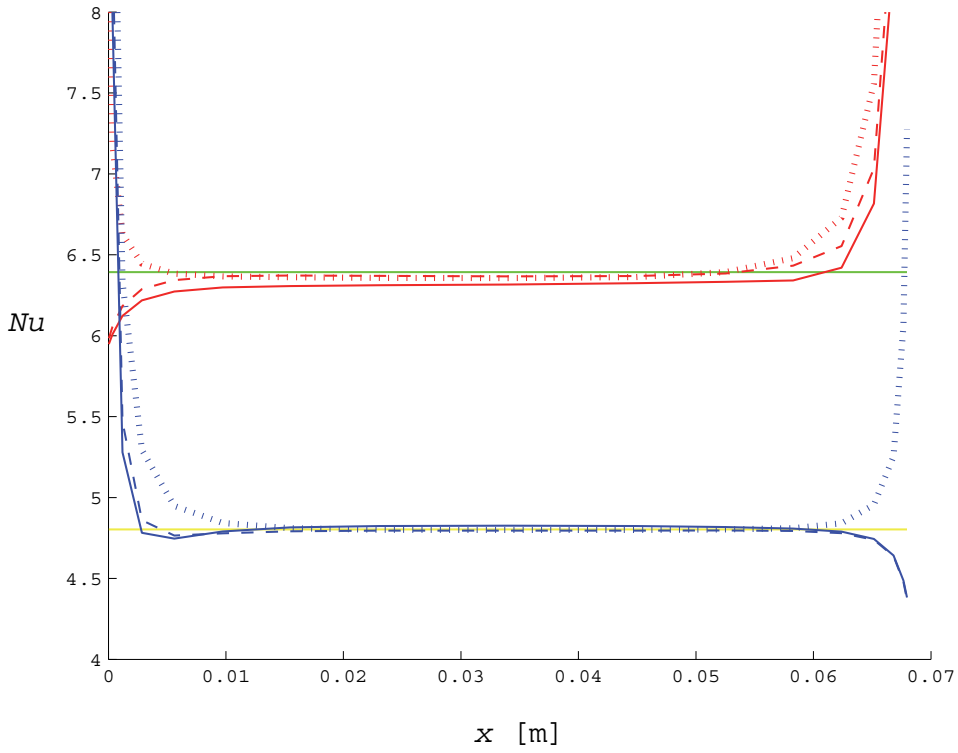

Figure 34: Nusselt number as a function of the axial coordinate of the microchannels; the values for the hot-side are plotted in **red**, those for the cold-side in **blue**; the respective analytical values are marked in **green** and **yellow**; solid lines refer to the temperature dependent properties case, dashed lines refer to constant properties, dotted lines to zero longitudinal heat conduction

The Nusselt number, plotted in Figure 34, stabilizes close to the analytical value for the H1 boundary condition given by equation (2.197), even if the wall heat flux, shown in Figure 35, is not perfectly constant. Especially for the gas-side, a slight variation of *Nu* is ascribable to temperature dependent properties, which, however leads to an overestimation of the effectiveness of only 0,6 %.

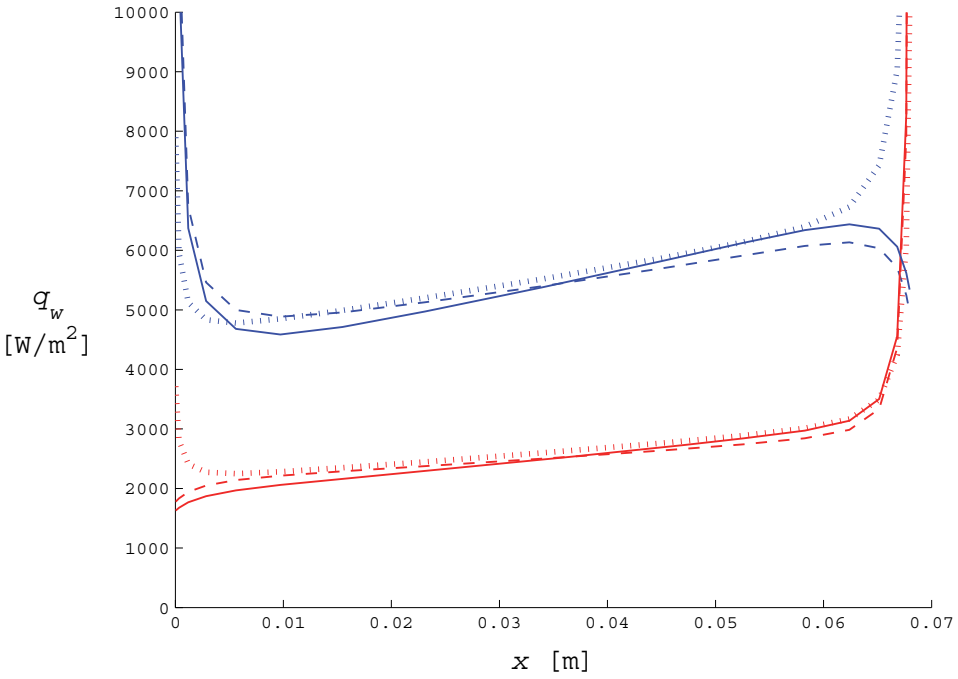

Figure 35: wall heat flux as a function of the axial coordinate of the microchannels; the values for the hot-side are plotted in **red**, those for the cold-side in **blue**; solid lines refer to the temperature dependent properties case, dashed lines refer to constant properties, dotted lines to zero longitudinal heat conduction

On the other hand, conjugate effects do not influence *Nu* appreciably, except in the entrance and exit region. Nonetheless the difference in ε is almost 3.4 % and the heat flux is sensibly decreased. As a consequence, according to (3.22), also the average temperature difference between the wall and the fluid temperature diminishes, as shown in Figure 36. Therefore, conjugate effects seem not to reduce the heat transfer coefficient with respect to the analytical value but, as assumed in [40], the performance deterioration is produced by the altered temperature profile in the walls. However, when the longitudinal heat conduction is particularly strong, also the boundary conditions are changed [39]. A progressive approach to the lower value characteristic of T boundary condition may be expected as limit when the thermal conductivity tends to infinity or *Re* to 0. In this case, the longitudinal heat conduction parameter of (1.28) is exceptionally high and the wall temperature distribution is flattened [21].

The results of the numerical analysis, confirm the choice of as correlation for Nu and Po. The temperature and pressure distribution along the channel are now considered to complete the validation. As visualized in Figure 37, heat transfer is well modelled,

giving a relative error of only 0.4 % on the effectiveness, when the values obtained from the optimization process are compared to the output of the numerical simulation. The pressure profile, plotted in Figure 38 relatively to the inlet pressure of each side, is altered by temperature dependent properties, as is the Poiseuille number. However, the variation is significant only for the hot-side and, as a whole, the relative error is not more than 0.6 %. On the other hand, in the crossflow configuration, temperature dependent properties may have stronger impact, since the temperature distribution along the channel is markedly non-linear. As already mentioned, it is possible to consider local values in the model of Section 2.4.4.

Notice that the geometries of Table 5 and Table 6 are designed considering *Nu* reduced by 10 % and *Po* increased by 10 % with respect to the analytical values. As described in Section 2.4.1 and 2.4.2, this common practice is suggested to account for flow maldistribution [23], which is not modeled in the optimization process nor in the numerical simulation. In addition, for the crossflow configuration

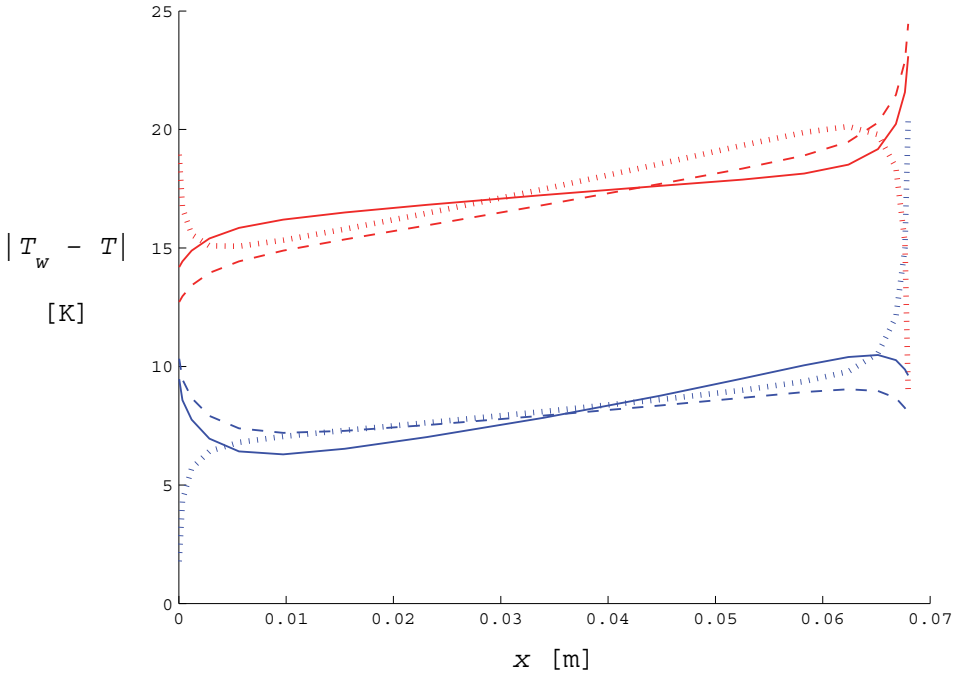

Figure 36: wall-fluid temperature difference (absolute value) as a function of the axial coordinate of the microchannels; the values for the hot-side are plotted in **red**, those for the cold-side in **blue**; solid lines refer to the temperature dependent properties case, dashed lines refer to constant properties, dotted lines to zero longitudinal heat conduction

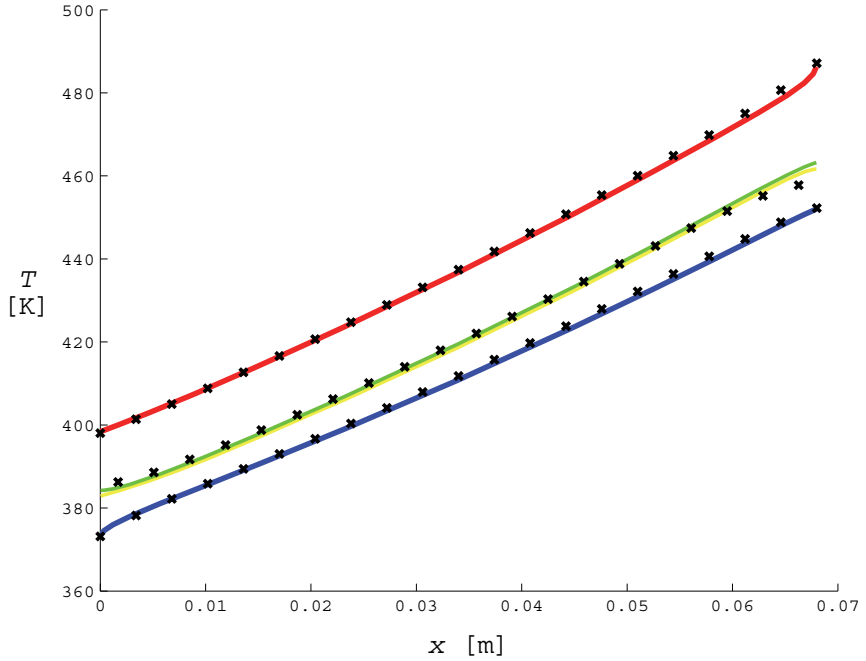

Figure 37: temperature field inside the microchannels; the **green** and **yellow** lines are the temperature on each side of the dividing wall; the **blue** line is the fluid temperature on the cold-side and the **red** line is the fluid temperature on the hot-side; the values calculated in the optimization process are indicated with × makers (no temperature jump is considered in the wall)

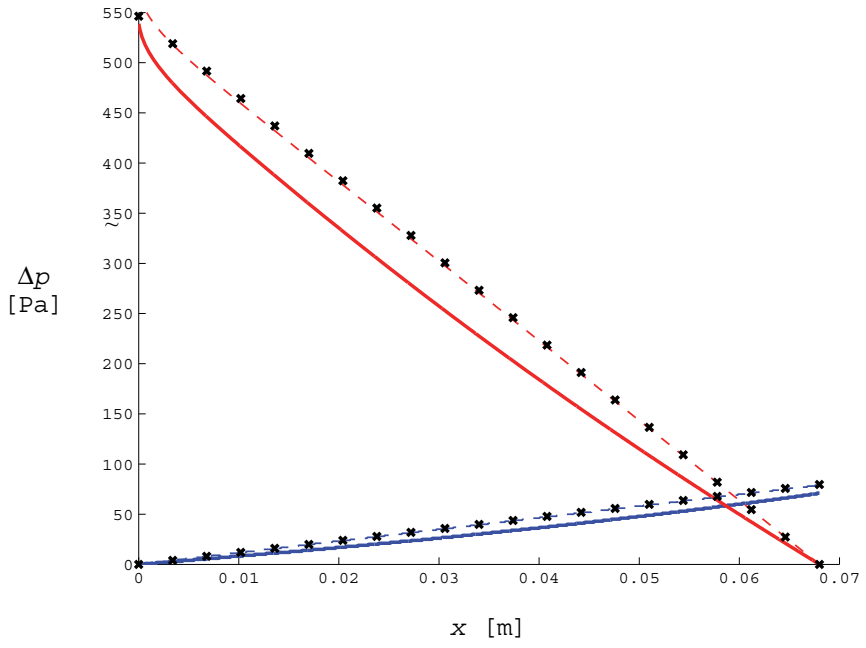

Figure 38: pressure drop relative to the inlet pressure as a function of the axial coordinate of the microchannels; the **blue** lines denote the cold-side and the **red** lines the hot-side; solid lines refer to the temperature dependent properties case while dashed lines refer to constant properties; the values calculated in the optimization process are indicated with × makers

3.5 Discussion

The optimization process, presented in the previous chapter and validated in the above sections, provides the best crossflow and counterflow configurations considering two different alloys, for a total of four devices. The overall dimensions and total weights are collected in Table 10.

Table 10: overall dimensions and weight of the optimized heat exchangers

Specification	Crossflow C878	Counterflow C878	Crossflow A360	Counterflow A360	Unit
Overall dimensions	318×374×590	184×309×660	376×378×521	184×360×645	mm^3
Total weight	87.7	84.1	41.9	35.0	kg

It is well known that, for given heat transfer surface area, the effectiveness of counterflow exchanger is considerably higher than for crossflow exchangers. However, the counterflow configurations of Table 10 are not significantly smaller or lighter than the crossflow arrangements, as can also be appreciated in Figure 21. The reason is that the headers constitute around two thirds of the device and, in the counterflow exchangers, are almost twice as heavy as the distribution elements of the crossflow exchangers. The choice between one configuration and the other should be made after a more precise design of the distribution elements and an evaluation of the manufacturing costs. In general, as already mentioned, crossflow heat exchangers are not suitable for application requiring effectiveness above 80 %. However, even for smaller effectiveness, the outlet temperature the firsts channels of each module almost reaches the inlet temperature of the other side, as shown in Figure 22. The crossflow configuration should then be avoided for a microchannel regenerator if the inlet temperatures are such that the risk of phase change is elevated.

Comparing the weight of each configuration considering the two different material, it turns out that the difference in weight do not reflects the difference in the density of the alloys, since the material with lower density has higher thermal conductivity. In fact, heavier conjugate effects make necessary to increase the heat transfer surface area, and

then the volume. The choice of the material should be therefore heavily influenced by thermal conductivity, which should be kept sufficiently high to neglect the thermal resistance of the dividing wall, but also appropriately low to avoid severe conjugate effects. It should be noted that the thermal conductivity of metals may be strongly temperature dependent. Unfortunately, no information was found for the considered alloys, with the exception of the values at 300 K, which are expected to be significantly lower than at the working temperature.

Table 11: specifications of the copper-based optimal MCHE and of the benchmark PHE

Specification	Crossflow – C878		Counterflow – C878		PHE		Unit
	Cold-side	Hot-side	Cold-side	Hot-side	Cold-side	Hot-side	
Outlet temperature	452.46	397.91	452.12	398.14	451.56	398.15	K
Total pressure drop	617	2704	180	3091	6	3220	Pa
Fluid velocity	0.0385	10.64	0.0246	9.10	0.01	17.18	m/s
Heat transfer coefficient (mean)	644.5	160.9	841.0	134.6	81.9	88.1	$W/(m^2 K)$
Heat transfer surface area	12.60	20.08	6.79	14.14	26.96	26.96	
Heat transfer surface area density	3596	3627	3967	3030	427	427	m^2/m^3
UA	2245		1400		1143		W/K
Effective *MTD*	15.81		25.36		31.13		K
NTU	5.62		3.50		2.86		#
ε	0.7828		0.7811		0.7807		#
Weight (empty)	82.1		81.9		156.8		kg
Fluid charge	5.6		2.2		58.6		kg
Overall dimension	318×374×590		184×309×660		222×495×1596		m^3

When selecting the material for the metal matrix, attention should be paid also to the maximum temperatures. In the case study, the hot-side inlet temperature (487 K) is close to the recommended limit (523 K) for the aluminium based alloy, above which the mechanical properties are progressively lost. Frequent thermal transients may compromise the durability of the component.

For a quick comparison, the specifications of the copper-based optimal geometries are reported in Table 11, aside of the specifications of the benchmark PHE from Table 1. It is apparent that the thermohydraulic requirement are satisfied with considerably smaller devices, which only need half of the material to be manufactured and require a fluid charge reduced by one order of magnitude.

The velocity of the cold-side is increased while the hot fluid is slowed down by modifying the flow areas. This allows compactness to be enhanced while containing the pressure drop on the gas side. Even if the pressure drop on the cold-side is higher in the MCHE compared to the PHE, the losses on the hot-side remain the most critic.

For obvious reasons, UA and NTU are larger in the crossflow exchanger. However, comparing the values of the other two devices of Table 11, it can be noted that higher values are required in the MCHE than in the benchmark PHE (in counterflow arrangement too). This is due to conjugate effects, which act as a heat bypass and reduce the effective NTU, although without actual heat loss [21].

Even if the turbulent flow of the PHE is characterized by significantly higher Nusselt number with respect to the laminar flow of the MCHE, the dramatic reduction of the hydraulic diameter leads to enhanced heat transfer coefficient in the MCHE, as expected from the discussion of Section 1.2.1. Since, in laminar conditions, Nu is independent of Re and therefore from the flow velocity, the heat transfer coefficient of the gas-side becomes considerably lower than on the cold-side, due to the lower thermal conductivity of the gas. However, the convective resistances are in part rebalanced by improving the heat transfer surface area in particular on the hot side. In any case, the required heat transfer surface is noticeably reduced compared to the PHE, because of the augmented heat transfer coefficient. Additionally, the surface is arranged in a more

efficient way, as the surface area densities is one order of magnitude higher when microchannels are used. It should be mentioned that the area densities of Table 11 are evaluated in the traditional way, where the volume of the dividing wall is not considered, differently from Section 2.2.2.

The minimum achievable weight, i.e. the weight of the optimal MCHE, is extremely sensitive to the maximum pressure drop allowed by the ORC heat recovery system. Strong influence is exerted also by the constraints of the available microfabrication techniques, in particular for what concerns the thickness of the microchannel walls and by the maximum aspect ratio allowed. The sensitivity analysis is accomplished executing iteratively the optimization process and varying (in separate tests) these quantities. The copper-based alloy and the counterflow configuration are taken into consideration.

Figure 39(a) shows that it is possible to reduce further the weight of the optimal device by increasing the allowed pressure drop, but it also suggests that the weight could hardly be halved with respect to the case study. On the other hand, it seems difficult to cut the pressure losses below 3000 Pa without dramatically increasing the weight of the MCHE; however, this restriction is not due to the use of microchannels per se, but rather to the distribution elements, which cause the highest pressure drop (see equation (2.189) and Table 8) could probably be improved.

A closely linear relationship between the minimal wall thickness imposed and the minimum achievable weight is illustrated by Figure 39(b). The manufacturing method and its limitations are therefore fundamental aspects to investigate, and are expected to play a fundamental role in a cost analysis.

The manufacturing process sets also the maximum aspect ratio of the microchannels and of the fins. Supposing these two quantities equal and varying their value, the results of Figure 39(c) are obtained. As anticipated in Section 2.2.2, higher aspect ratios guarantee lower weight.

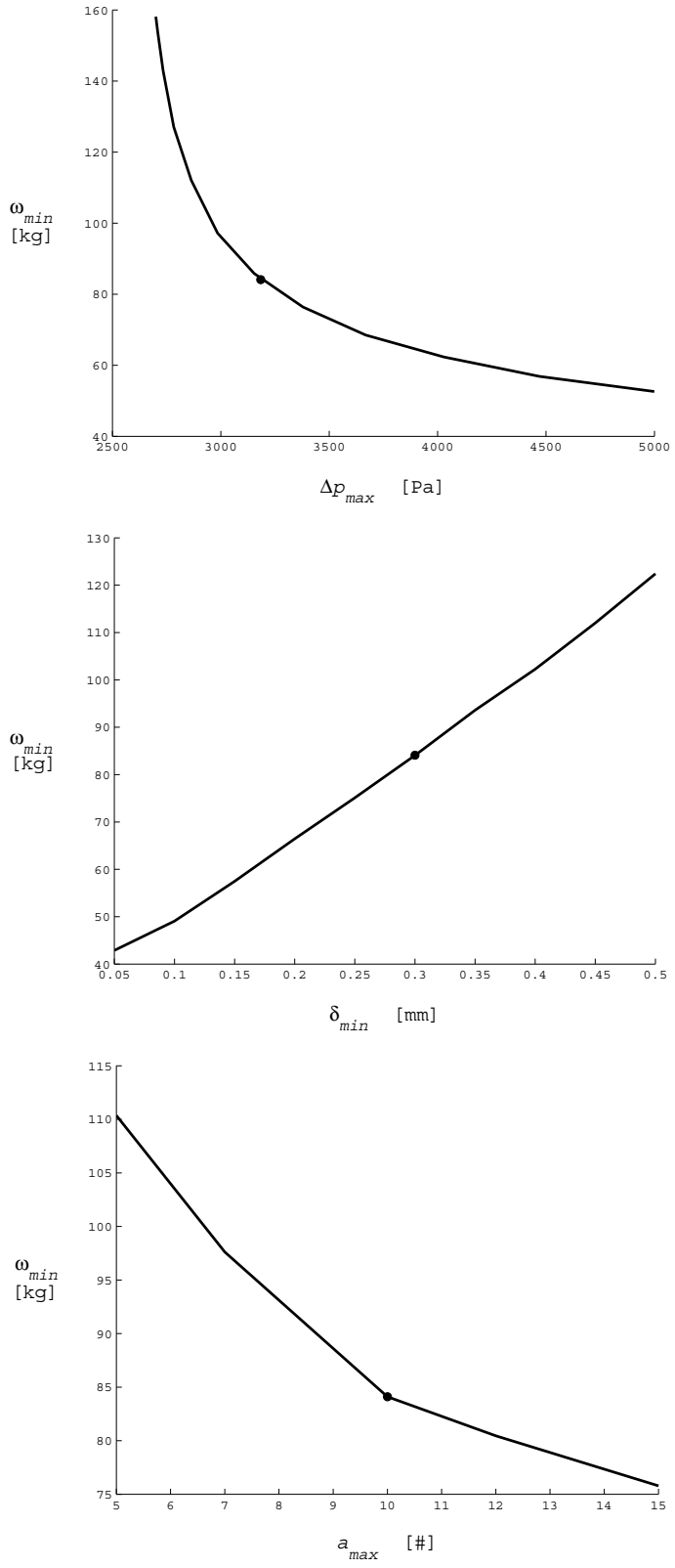

Figure 39: sensitivity analysis of the optimal solution with respect to the maximum pressure drop allowed (a), to the minimum wall thickness (b) and to the maximum aspect ratio (c); the • markers indicates the design point of the case study, characterized by equations (2.2) (2.59) and (2.48)

3.6 Conclusions and Recommendations

In this work, the performance of microchannel heat exchangers was assessed in gas-to-liquid applications of several tens of kW_{th} . The technology is suitable for exhaust heat recovery systems based on organic Rankine cycle. In order to design a light and compact microchannel heat exchanger, an optimization process was developed and validated numerically. No application of microchannels at comparable power level is available in the open literature, and little attention is given to optimization of microchannel devices, such that unprecedented number of design parameters is considered in the present work, including but not limited to dimensions, length and number of the microchannels on each side of the exchanger.

The model employed in the procedure was validated through computational fluid-dynamics analysis with commercial software. It was shown that conjugate effects have a significant impact on the heat transfer performance of the device. The Nusselt number is close to the analytical value of laminar flows with H-boundary condition; however, the heat transfer pattern is altered by variations in the wall temperature distribution. The effect is well modeled in the optimization process, such that the relative error on the exchanger effectiveness is less than 0.4% when the optimized geometry is simulated numerically. The variation of the fluid properties with temperature reduces the Poiseuille number. However, the relative error between the core pressure drop accounted in the proposed methodology and the one calculated trough numerical analysis is in order of 0,6 %.

The selection process needs only a few minutes of computational time, since great effort was made to minimize the number of operations for each iteration, and to define suitable constraints, which limit the design space where the optimal value of the design parameters are searched. These constraints were imposed through considerations on the manufacturing method, on the distribution elements and on the interaction of the proposed device with the other component of the mobile ORC heat recovery system.

The input for the optimization is constituted by the required effectiveness, the maximum allowable pressure drop and some information on the distribution elements, since their

design could not be automated. The output of the procedure is constituted by four different designs, since both the counterflow and the crossflow arrangements are considered for two different alloys for the metal matrix.

The aluminium-based alloy, even if significantly lighter with respect to the copper-based alloy, determines larger devices, due to higher thermal conductivity and conjugate effects. Moreover, the working temperature is dangerously close to the thermal stability limit of the material. For these reasons, a copper-based microchannel exchanger seems to be preferable.

No significant difference was found comparing the counterflow and crossflow arrangements obtained through the optimization process, as the distribution elements constitutes the largest part of the microchannel exchangers. Both devices are strikingly smaller and lighter than the benchmark heat exchanger, which is almost five times big and two times heavier. Microchannel heat exchangers are therefore a competitive technology not only for low power applications but also when heat fluxes in the order of several tens of kW_{th} are involved.

The distribution elements, especially those on the hot-side, are critical for the design of MCHE: several constraints were imposed to limit their dimension, weight and pressure losses. In this paper, however, only a rough header design was considered, due to the lack of a comprehensive theory. Numerical simulations and field experience are needed to acquire accurate flow distribution and pressure drop predictions: the flow characteristic of the headers, along with their technical feasibility and cost, are expected to impact on the choice between the crossflow and the counterflow arrangement.

Information and experience on the manufacturing method and materials are also needed. In fact, some of the imposed constraints depend on the microfabrication methods available, which are then expected to play a fundamental role in a future cost-benefit analysis; in addition, the performance of the MCHE is strongly related to surface roughness and thermal conductivity of the walls. Special attention is due to the bonding technique employed, in order to guarantee structural integrity and acceptable contact resistance at a reasonable cost.

References

[1] European Environment Agency, "Trends and projections in Europe 2013: Tracking progress towards Europe's climate and energy targets until 2020", EEA Report no. 10/2013.

[2] European Environment Agency, "Annual European Union greenhouse gas inventory 1990–2012 and inventory report 2014", Technical report no. 09/2014.

[3] AEA Technology, "Reduction and Testing of Greenhouse Gas Emissions from Heavy Duty Vehicles – Lot 1: Strategy", Final Report to the European Commission – DG Climate Action, 2011.

[4] S. N. Hossain and S. Bari, "Waste heat recovery from the exhaust of a diesel generator using Rankine Cycle", *Energy Conversion and Management*, vol. 75, 2013.

[5] C. Sprouse and C. Depcik, "Review of organic Rankine cycles for internal combustion engine exhaust waste heat recovery", *Applied Thermal Engineering*, vol. 51, 2013.

[6] W. Lang, P. Colonna, and R. Almbauer, "Assessment of Waste Heat Recovery from a Heavy-Duty Truck Engine by Means of an ORC Turbogenerator", *Journal of Engineering for Gas Turbines and Power*, vol. 135, 2013.

[7] G. Angelino, M. Gaia, and M. Macchi, "A review of Italian activity in the field of Organic Rankine Cycles", in *VDI Berichte 539 – Verein Deutscher Ingenieure, ORC-HP-technology Working Fluid Problems, Proceedings of the international VFI-seminar*, Zurich, Switzerland, 1984.

[8] T. Wang et al., "A review of researches on thermal exhaust heat recovery with Rankine cycle", *Renewable and Sustainable Energy Reviews 15 (2011) 2862–2871*, vol. 15, 2011.

[9] D. T. Hountalas et al., "Improvement of bottoming cycle efficiency and heat rejection for HD truck applications by utilization of EGR and CAC heat", *Energy Conversion and Management*, vol. 53, 2012.

[10] L. Guillaume et al., "Sizing Models and Performance Analysis of Waste Heat Recovery Organic Rankine Cycles for Heavy Duty Trucks", in *Second International Seminar on ORC Power Systems*, Rotterdam, The Netherlands, 2013.

[11] M. Ohadi et al., *Next Generation Microchannel Heat Exchangers*, Springer, 2013.

[12] M. G. Khan and A. Fartaj, "A review on Microchannel Heat Exchangers and Potential Applications", *International Journal of Energy Research*, vol. 35, 2011.

[13] C. M. Invernizzi, *Closed Power Cycle: Thermodynamic Fundamentals and Applications*, Springer-Verlag, 2013.

[14] M. Gaia, "Thirty years of organic Rankine cycle development", in *First International Seminar on ORC Power Systems*, Delft, the Netherlands, 2012.

[15] G. Angelino and P. Colonna, "Multicomponent Working Fluids for Organic Rankine cycles", *Energy*, vol. 23, 1998.

[16] O. Badr, S. D. Probert, and P. W. O'Callaghan, "Selecting a Working Fluid for a Rankine-Cycle Engine", *Applied Energy*, vol. 21, 1985.

[17] B. Saleh et al., "Working fluids for low-temperature organic Rankine cycles", *Energy*, vol. 32, 2007.

[18] P. Song et al., "A review of scroll expanders for organic Rankine cycle systems", *Applied Thermal Engineering*, vol. xxx, 2014.

[19] P. Bombarda, C. M. Invernizzi, and C. Pietra, "Heat recovery from Diesel engines: A thermodynamic comparison between Kalina and ORC cycles", *Applied Thermal Engineering*, vol. 30, 2007.

[20] C. M. Invernizzi, P. Iora, and P. Silva, "Bottoming micro-Rankine cycles for micro-gas turbines", *Applied Thermal Engineering*, vol. 27, 2007.

[21] J. E. Hesselgreaves, *Compact Heat Exchangers: Selection, Design and Operation.*, Pergamon, 2001.

[22] S Kandlikar et al., *Heat Transfer and Fluid Flow in Minichannels and Microchannels*, Elsevier, 2006.

[23] R.K. Shah and D.P. Sekulic, *Fundamentals of Heat Exchanger Design*, John Wiley & Sons, 2003.

[24] S. G. Kandlikar and W. J. Grande, "Evolution of Microchannel Flow Passages: Thermohydraulic Performance and Fabrication Technology ", *Heat Transfer Engineering*, vol. 24, 2003.

[25] H. Herwig and S. P. Mahulikar, "Variable property effects in single-phase incompressible flows through microchannels", *International Journal of*

Thermal Sciences, vol. 45, 2006.

[26] H. Herwig and O. Hausner, "Critical View on “New Results in Micro-Fluid Mechanics”: An Example", *International Journal Heat Mass Transfer*, vol. 46, 2003.

[27] G. L. Morini, "Scaling Effects for Liquid Flows in Microchannels", *Heat Transfer Engineering*, vol. 27, 2006.

[28] Z. Y. Guo and Z. X. Li, "Size effect on single-phase channel flow and heat transfer at microscale", *International Journal of Heat and Fluid Flow 24 (2003) 284–298*, vol. 24, 2003.

[29] P. Rosa, T. G. Karayiannis, and M. W. Collins, "Single-Phase Heat Transfer in Microchannels: The Importance of Scaling Effects", *Applied Thermal Engineering*, vol. 29.

[30] G. L. Morini and Y. Yang, "Guidelines for the Determination of Single-Phase Forced Convection Coefficients in Microchannels", *Journal of Heat Transfer*, vol. 135, 2013.

[31] G. L. Morini et. al., "A critical review of the measurement techniques for the analysis of gas microflows through microchannels", *Experimental Thermal and Fluid Science*, no. 35, 2011.

[32] G. Hetsroni et al., "Fluid flow in micro-channels", *International Journal of Heat and Mass Transfer*, vol. 48, 2005.

[33] G. L. Morini and M. Spiga, "Slip Flow in Rectangular microtubes", *Microscale Thermophysical Engineering*, vol. 2, 1998.

[34] S. Colin, "Gas Microflows in the Slip Flow Regime: A Critical Review on Convective Heat Transfer", *Journal of Heat Transfer*, vol. 134, 2012.

[35] C. Li, L. Jia, and T. Zhang, "The Entrance Effect on Gases Flow Characteristics in Micro-tube", *Journal of Thermal Science*, vol. 18, 2009.

[36] T. M. Harms, M. J. Kazmierczak, and F. M. Gerner, "Developing convective heat transfer in deep rectangular microchannels", *International Journal of Heat and Fluid Flow*, vol. 20, 1999.

[37] M. K. Moharana, G. Agarwal, and S. Khandekar, "Axial conduction in single-phase simultaneously developing flow in a rectangular mini-channel array", *International Journal of Thermal Sciences*, vol. 50, 2011.

[38] Y. S. Muzychka and M. M. Yovanovich, "Laminar Forced Convection Heat Transfer in the Combined Entry Region of Non-Circular Ducts", *Journal of Heat*

Transfer, vol. 126, 2004.

[39] G. Maranzana, I. Perry, and D. Maillet, "Mini- and micro-channels: influence of axial conduction in the walls", *International Journal of Heat and Mass Transfer*, vol. 47, 2004.

[40] J. P. Chiou, "The Effect of Longitudinal Heat Conduction on Crossflow Heat Exchanger", *Journal of Heat Transfer*, vol. 100, 1978.

[41] S. G. Kandlikar, S. Joshi, and S. Tian, "Effect of Surface Roughness on Heat Transfer and Fluid Flow Characteristics at Low Reynolds Numbers in Small Diameter Tubes", *Heat Transfer Engineering*, vol. 24, 2003.

[42] G. Gamrat, M. Favre-Marinet, and S. Le Person, "Modelling of roughness effects on heat transfer in thermally fully-developed laminar flows through microchannels", *International Journal of Thermal Sciences*, vol. 48, 2009.

[43] G. Croce, P. D'agaro, and C. Nonino, "Three-dimensional roughness effect on microchannel heat transfer and pressure drop", *nternational Journal of Heat and Mass Transfer*, vol. 50, 2007.

[44] M Gad-el-Hak, "The Fluid Mechanics of Microdevices—The Freeman Scholar Lecture", *Journal of Fluids Engineering*, vol. 121, 1999.

[45] N. P. Gulhane and S. P. Mahulikar, "Numerical study of compressible convective heat transfer with variations in all fluid properties", *International Journal of Thermal Sciences*, vol. 49, 2010.

[46] Z. Li et al., "Effects of thermal property variations on the liquid flow and heat transfer in microchannel heat sinks", *Applied Thermal Engineering*, vol. 27, 2007.

[47] G. L. Morini et al., "Experimental Analysis of Pressure Drop and Laminar to Turbulent Transition for Gas Flows in Smooth Microtubes", *Heat Transfer Engineering*, vol. 28, 2007.

[48] G. L. Morini and M. Spiga, "The Role of the Viscous Dissipation in Heated Microchannels", *Journal of Heat Transfer*, vol. 129, 2007.

[49] K. D. Cole and B. Çetin, "The effect of axial conduction on heat transfer in a liquid microchannel flow", *International Journal of Heat and Mass Transfer*, vol. 54, 2011.

[50] C. Yang, D. Li, and J. B. Masliyah, "Modelling forced liquid convection in rectangular microchannels with electrokinetic effects", *International Journal of Heat and Mass Transfer*, vol. 41, 1998.

[51] G. M. Mala and D. Li, "Flow characteristics of water through a microchannel between two parallel plates with electrokinetic effects", *International Journal of Heat and Fluid Flow*, vol. 18, 1997.

[52] C. L. Ren and D. Li, "Improved understanding of the effect of electrical double layer on pressure-driven flow in microchannels", *Analytica Chimica Acta*, vol. 531, 2005.

[53] C. Yang and D. Li, "Analysis of electrokinetic effects on the liquid flow in rectangular microchannels", *Colloids and Surfaces A: Physicochemical and Engineering Aspects*, vol. 143, 1998.

[54] S. S. Mehendale, A. M. Jacobi, and R. K. Shah, "Fluid flow and heat transfer at micro- and meso-scales with application to heat exchanger design", *Applied Mechanics Reviews*, vol. 53, no. 2000.

[55] S. Ashman and S. G. Kandlikar, "A Review of Manufacturing Processes for Microchannel Heat Exchanger Fabrication", in *Fourth International Conference on Nanochannels, Microchannels and Minichannels*, Limerick, Ireland, 2006.

[56] F. Mei et al., "Fabrication, Assembly, and Testing of Cu- and Al-Based Microchannel Heat Exchangers", *Journal of Microelectromechanical Systems*, vol. 17, 2008.

[57] F. Mei and W. J. Meng, "Structure of vapor-phase deposited Al-Ge thin films and Al-Ge intermediate layer bonding of Al-based microchannel structures", *Journal of Materials Research*, vol. 24, 2009.

[58] D. M. Cao and W. J. Meng, "Microscale compression molding of Al with surface engineered LiGA inserts", *Microsystem Technologies*, vol. 10, 2004.

[59] H. Wang and R. B. Peterson, "Performance enhancement of a thermally activated cooling system using microchannel heat exchangers", *Applied Thermal Engineering*, vol. 31, 2011.

[60] V. Gnielinski, "Ein Neues Berechnungsverfahren fur die Warmeubertragung im Ubergangsbereich zwischen Laminaren und Turbulenter Rohstromung", *Forschung im Ingenieurwesen - Engineering Research*, vol. 61, 1995.

[61] H. Cao, G. Chen, and Q. Yuan, "Testing and Design of a Microchannel Heat Exchanger with Multiple Plates", *Industrial and Engineering Chemistry Reasearch*, vol. 48, 2009.

[62] C. Harris, M. Despa, and K. Kelly, "Design and Fabrication of a Cross Flow Micro Heat Exchanger", *Journal of Microelectromechanical systems*, vol. 9, 2000.

[63] Y. S. Muzychka, "Constructal design of forced convection cooled microchannel heat sinks and heat exchangers", *International Journal of Heat and Mass Transfer*, vol. 48, 2005.

[64] M. I. Hasan et al., "Influence of channel geometry on the performance of a counter flow microchannel heat exchanger", *International Journal of Thermal Sciences*, vol. 48, 2009.

[65] B, Northcutt and I. Mudawar, "Enhanced Design of Cross-Flow Microchannel Heat Exchanger Module for High-Performance Aircraft Gas Turbine Engines", *Journal of Heat Transfer*, vol. 134, 2012.

[66] J. V. C. Vargas, A. Bejan, and D. L. Siems, "Integrative Thermodynamic Optimization of the Crossflow Heat Exchanger for an Aircraft Environmental Control System", *Journal of Heat Transfer*, vol. 123, 2001.

[67] Y. Yang, J. J. Brandner, and G. L. Morini, "Hydraulic and thermal design of a gas microchannel heat exchanger", *Journal of Physics: Conference Series*, vol. 362, 2012.

[68] D. T. Crane and G. S. Jackson, "Optimization of cross flow heat exchangers for thermoelectric waste heat recovery", *Energy Conversion and Management*, vol. 45, 2004.

[69] H. H. Bau, "Optimization of conduits' shape in micro heat exchangers", *International Journal of Heat and Mass Transfer*, vol. 41, 1998.

[70] L. Gosselin, M. T. Gingras, and F. M. Potvin, "Review of utilization of genetic algorithms in heat transfer problems", *International Journal of Heat and Mass Transfer*, vol. 52, 2009.

[71] TIAX, "Energy Consumption Characteristics of Commercial Building HVAC Systems Volume III: Energy Savings Potential", Reference No. 68370-00, 2002.

[72] North American Die Casting Association, "Product Specification Standards for Die Castings", NADCA Publication #402 2009.

[73] E. M. Smith, *Advances in Thermal Design of Heat Exchangers, A Numerical Approach:Direct-sizing, step-wise rating, and transients*, John Wiley & Sons, 2005.

[74] AEA Technology, "The Standards of the Brazed Aluminum Plate-Fin heat Exchanger Manufacturer Association", ALPEMA, 2000.

[75] American Society of Mechanical Engineers, "Welded and Seamless Wrought Steel Pipe", ASME B36.10M-2004.

[76] American Society of Mechanical Engineers, "Power Piping", ASME B31.1-2007.

[77] American Society of Mechanical Engineers, "Construction of Pressure Vessels", ASME BPVC-VIII-1-2010.

[78] C. Branan, *Rules of Thumb for Chemical Engineers*, Elsevier, 2005.

[79] A. L. London, G. Klopfer, and S. Wolf, "Oblique Flow Headers for Heat Exchangers", *Journal of Engineering for Power*, July 1968.

[80] S. Kakaç and Liu H., *Heat Exchangers - Selection, Rating and Thermal Design*, CRC Press, 2002.

[81] B.S. Baclic and P.J. Heggs, "On the search for new solutions of the single-pass crossflow heat exchanger problem", *International Journal of Heat and Mass Transfer* , vol. 28, 1985.

[82] R. Laskowski, "The concept of a new approximate relation for exchanger heat transfer effectiveness for a cross-flow heat exchanger with unmixed fluids", *Journal of Power Technologies*, vol. 91, 2011.

[83] A. Triboix, "Exact and approximate formulas for cross flow heat exchangers with unmixed fluids", *International Communications in Heat and Mass Transfer*, vol. 36, 2009.

[84] R. K. Shah and A. L. London, *Laminar Flow Forced Convection in Ducts: a Source Book for Compact Heat Exchanger Analytical Data*, Academic Press, 1978.

[85] W. M. Kays and A. L. London, *Compact Heat Exchangers*, McGraw-Hill, 1984.

[86] J. P. Chiou, "Thermal Performance Deterioration in Crossflow Heat Exchanger due to the Flow Nonuniformity", *Journal of Heat Transfer*, vol. 100, 1978.

[87] J. J. Brandner et al., "Microstructure Heat Exchanger Applications in Laboratory and Industry", *Heat Transfer Engineering*, vol. 28, 2007.

Software References

- Aspen Exchanger Design&Rating (EDR) V7.3.1 by Aspen Technology Inc.
- Aspen Properties V7.3.1 by Aspen Technology Inc.
- Fluent 6.3.26 by ANSYS Inc.
- GAMBIT 2.4.6 by ANSYS Inc.
- Mathematica 9.0.1.0 by Wolfram Research Inc.
- MATLAB 7.10.0 (R2010a) by MathWorks Inc.
- Solid Edge ST6 by Siemens PLM Software Inc.